Czech Technical University in Prague

Faculty of Electrical Engineering

Doctoral Thesis

August, 2017 **Ing. Petr Mašek**

Czech Technical University in Prague

Faculty of Electrical Engineering

Department of Microelectronics

Multi-coincidence System of Ionization Radiation Detectors Based on Advanced Position Sensitive Detectors

Doctoral Thesis

Ing. Petr Mašek

Prague, August 2017

Ph.D. Programme: *P2612* Electrical Engineering and Information Technology
Branch of study: *2612V015* Electronics

Supervisor: Prof. Ing. Miroslav Husák, CSc.
Supervisor-Specialist: Ing. Jan Jakůbek, Ph.D.

Acknowledgements

I would like to express my gratitude to my supervisor prof. Ing. Miroslav Husák, CSc. for his valuable comments and his leadership of this work and to my supervisor specialist Ing. Jan Jakůbek, Ph.D. for his practical advices and endless enthusiasm.

My thanks also belong to all my colleagues from Institute of Experimental and Applied Physics, particularly the colleagues from the lab, who contributed to this work by their support, opinions and who involuntarily shared my worries and problems regarding this work. My special thanks go to the former director, Ing. Stanislav Pospíšil, DrSc., and the current director, doc. Ing. Ivan Štekl, CSc., of the Institute of Experimental and Applied Physics for a chance to work in the institute where I got a lot of scientific experience and met many challenging projects.

The last but not least thanks belong to my family – parents Ivana and Miroslav, sister Iva with her family for their support and also to my wife Eva who married me during my doctoral study and thus significantly cheered my life.

Declaration

I hereby declare that the doctoral thesis has been done independently under the leadership of the supervisor prof. Ing. Miroslav Husák, CSc. and the supervisor-specialist Ing. Jan Jakůbek, Ph.D. and that I used only literature and sources which are cited and listed in this document.

In Prague …… …….

Ing. Petr Mašek

Abstract

Detection of ionizing radiation is an issue which affects many areas of a human life. Significant progress in detection capabilities was caused by the development of electronics in recent decades. This dissertation thesis, which deals with the design of the Multi-coincidence system of ionizing radiation detectors, follows this trend.

The Multi-coincidence system of ionizing radiation detectors combines extraordinary technologies and due to using advanced electronics allows them to operate in a synchronous mode that brings new possibilities in radiation environment investigation, such as incoming direction or separation of particle types in a mixed radiation field. This dissertation thesis summarizes the development from the basic design, through hardware, firmware and software for user control as well as basic data processing. The functionality of the design is verified on a prototype and demonstrated by measurements whose results are also presented.

The design is based on "sandwich" structure composed of two detection parts in closed geometry – a silicon pixel detector Timepix and a plastic scintillator covered by silicon photomultipliers. The pixel detector Timepix is a device with excellent parameters and unrivaled ability of detection and recognition of different types of radiation. The disadvantage is the detection material itself which does not allow to effectively detect certain types of radiation, such as neutrons. This is the domain of scintillation detectors. Recent optical sensors called silicon photomultipliers offers possibility for detecting of the scintillating light by small-size device.

The Multi-coincidence system is a compact portable detection unit which can be used in applications where small dimensions are a significant requirement. Furthermore, it is insensitive to a magnetic field. Utilization of the system can be found in different areas from searching of radiation threats, through dosimetry to space weather monitoring.

Keywords:

ionizing radiation; neutrons; pixel detector; scintillator; silicon photomultiplier; SiPM; FITPix; VATA64HDR16; dongle;

Anotace

Detekce ionizačního záření je aktuální problém a zasahuje do mnoha oblastí lidského života. Významný posun v možnostech detekce přinesl rozvoj elektroniky v posledních dekádách. V tomto směru pokračuje i tato dizertační práce, která se zabývá návrhem Multi-koincidenčního systému detektorů ionizačního záření.

Multi-koincidenční systém detektorů ionizačního záření sdružuje výjimečné technologie a pomocí pokročilé elektroniky umožňuje jejich činnost v režimu, který přináší nové možnosti ve zkoumání prostředí s ionizačním zářením jako např. přicházející směr nebo rozlišení různých typů záření ve směsných polích. V této dizertační práci je shrnut vývoj zařízení od samotného návrhu, přes hardware, firmware i software, pro interakci s uživatelem a také základní zpracování dat. Návrh zařízení je ověřen na prototypu a demonstrován měřeními, jejichž výsledky jsou taktéž uvedeny.

Návrh systému je založen na „sendvičové“ struktuře se dvěma detektory umístěnými ve vzájemné blízkosti - s křemíkovým pixelovým detektorem Timepix a plastickým scintilátorem pokrytým křemíkovými fotonásobiči. Pixelový detektor Timepix je zařízením se špičkovými parametry a bezkonkurenční schopností detekce a rozlišení různých typů záření. Nevýhodou je samotný detekční materiál, který z fyzikální podstaty neumožňuje účinnou detekci některých typů záření, jako například neutronů. V tomto ohledu vynikají plastové scintilační detektory. Nové optické senzory zvané křemíkové fotonásobiče nabízí možnost detekce scintilačního světla s velice malými nároky na velikost v porovnání s konvenčními fotonásobiči.

Multi-koincidenční systém je kompaktní přenosné detekční zařízení, které může být použito v aplikacích, kde jsou malé rozměry jedním z významných požadavků. Navíc je necitlivý k magnetickému poli. Využití systému lze nalézt v různých oblastech od vyhledávání radiačních hrozeb, přes dozimetrii až po monitorování kosmického počasí.

Klíčová slova:

ionizační záření; pixelový detektor; scintilátor; křemíkový fotonásobič; SiPM; FITPix; VATA64HDR16; dongle;

Contents

Acknowledgements III
Declaration IV
Abstract V
Anotace VI
Contents VII
List of abbreviations X
List of symbols XII
List of figures XIII
List of tables XIX
1. Introduction and Thesis Overview 20
1.1. Research goals 20
1.2. Thesis structure 21
2. Ionizing radiation 22
2.1. Heavy charged particles 22
2.2. Light charged particles 23
2.3. Electromagnetic radiation 23
2.4. Neutrons 24
3. Ionizing radiation detectors 27
3.1. Detection structure optimization 28
3.2. Processing of the signal from the detector 30
4. The state-of-art ionizing radiation detectors 32
4.1. Pixel detector Timepix 32
Equalization and calibration 34
Charge sharing and particle recognition 34
Advanced structures with Timepix 36
Neutron detection with Timepix 37
4.2. Silicon photomultipliers 38
5. Design of the Multi-coincidence system 41
5.1. Requirements of the system 41
5.2. Structure of the sensitive layer 42
5.3. System design 43
6. Scintillator & SiPM array 45
6.1. Plastic scintillator 45
Scintillator thickness optimization 45

6.2. Array of silicon photomultipliers 47
Readout circuits 47
IV characteristics 48
Temperature stability 49
Photomultiplier tube replacement 53
7. Analog front-end for SiPM 55
7.1. SiPM readout ASICs 55
7.2. ASIC VATA64HDR16 56
Internal structure 57
Front-end functionality 58
ASIC configuration 59
Readout sequence 59
Power supply & signal levels 60
8. Spectroscopic ASIC readout system 61
8.1. Interface board 61
Analog path 61
Digital path 62
Power supply 62
Communication interface 62
FPGA 62
8.2. Chip dongle 63
VATA64HDR16 dongle 63
9. Firmware 64
9.1. Core state machines 64
Command FSM 65
Readout FSM 65
9.2. Peripherals 67
FT232 interface 67
ADC driver 67
DAC driver 68
Pin driver 68
Start & coincidence 68
9.3. Firmware occupancy & portability 69
10. Prototype of the Multi-coincidence system 71
11. Acquisition software & basic processing 74
11.1. Readout tool 74
GUI 74

Processing thread 79
11.2. Processing software 80
12. Measurements and results 83
12.1. ASIC readout system initiation 83
12.2. Pedestal correction 84
12.3. SiPM array equalization 85
12.4. Summing SiPM elements 87
12.5. Data synchronization check 88
12.6. Experiment with fast neutrons 89
13. Results comparison 101
14. Conclusions 103
References 106
List of candidate's publications 110
Appendix A 113
Appendix B 117
Appendix C 118

List of abbreviations

AD-BANG	Advanced Detectors for Better Awareness of Neutrons and Gamma rays in environment
APD	avalanche photodiode
AmBe	americium beryllium
ASIC	application specific integrated circuit
CdTe	cadmium telluride
CERN	Conseil Européen pour la Recherche Nucléaire
CMOS	complementary metal–oxide–semiconductor
CTU	Czech technical university
DAC	digital-to-analog converter
DAQ	data acquisition
DLL	dynamic-link library
D-T	deuterium-tritium
FET	field effect transistor
FITPix	Fast Interface for Timepix Pixel detector
FPGA	field programmable gate array
FSM	finite state machine
FWHM	full with at half maximum
FTDI	Future Technology Devices International Ltd.
GaAs	gallium arsenide
GAPD	geiger-mode avalanche photodiode
GUI	graphical user interface
HSTL	high-speed transceiver logic
IDEAS	Integrated Detector Electronics AS
IEAP	Institute of Experimental and Applied Physics
I/O	input/output
ISE	integrated software environment
JTAG	Joint Test Action Group
LaBr	lanthanum bromide
LED	light emitting diode
LuAG	lutetium aluminium garnet
LVDS	low voltage differential signaling
MIP	minimum ionizing particle

MPPC	multi-pixel photon counter
NaI:Tl	natrium iodide doped by thallium
PAR	place and route
PCB	printed circuit board
PMT	photomultiplier tube
POPOP	1,4-bis(5-phenyloxazol-2-yl) benzene
pTP	p-terphenyl
SiPM	silicon photomultiplier
SPI	serial peripheral interface
SSPM	solid state photomultiplier
TAC	time-to-analog converter
TOF	time-of-flight
TOT	time-over-threshold
UART	universal asynchronous receiver/transmitter
VATA	Viking amplifier-trigger amplifier, designation of chips produced by IDEAS company
VHDL	VHSIC hardware description language
VHCIS	very high speed integrated circuit
YAP	yttrium aluminum perovskite

List of symbols

Bq	becquerel, radioactivity unit, 1 Bq = 1/s
Ci	curie, non-SI radioactivity unit, 1 Ci = 3.7×10^{10} Bq
E_α	alpha particle energy
E_N	energy of the primary neutron
E_R	energy of the recoiled particle
M_N	neutron mass
M_R	mass of the target material
ν	antineutrino
N(0)	number of particles entering in the absorber
N(x)	number of particles penetrating the absorber of the thickness x
Q	energy released by the reaction
R_{air}	particle range in the air
V_{bias}	bias voltage applied to the component
V_{DAC}	voltage generated by the DAC
V_{sipm}	operation voltage of the SiPM inducing the avalanche

List of figures

Figure 1: The graph shows the contributions of the three competitive processes of interaction in matter. The probability of the individual process is highly dependent on the energy [1]. 24

Figure 2: An illustration of the deposition of the charge depending on the particle trajectory angle (left) and the position of interaction (right) [2]. The particle going through the detector can deposit charge which is collected into more than one strip. Interpolation and fit of the charge distribution improve the spatial resolution. 29

Figure 3: A schematic view of a pixel detector is depicted. The pixelated sensor is attached to readout electronics. The electrical contact is provided by bump-bonding technology [2]. 29

Figure 4: The accuracy of the system is evaluated by FWHM of spectrum peak [1]. ... 31

Figure 5: Shaped pulses pile-ups cause spectrum distortion when shaping is too long (left). Decreased shaping (right) has no such an effect [2]. 31

Figure 6: Block scheme of the Timepix cell. Two parts can be distinguished. The analog signal is amplified and compared to the threshold voltage. Digital conversion depends on the chosen mode of the operation [4]..... 33

Figure 7: Typical waveforms of Timepix modes. The shutter has to be active to enable particle detection. The amplified signal is compared to the threshold. The counting mode increments the register when the signal crosses the threshold. The time-of-arrival mode counts clock periods till the end of the shutter. The time-over-threshold mode accumulates the clock pulses when the signal is above the threshold. 34

Figure 8: 3D visualization of pixel detector response (protons recoiled by fast neutrons) at two different bias voltages is depicted. Event clusters measured with bias of 20 V are high and narrow (left) while low 5 V bias allows the charge to spread out to more pixels (right). 35

Figure 9: Integrated frames measured by pixel detector Timepix in different radiation fields. Heavy charged particles (left) significantly differ from long tracks (right) made by fast electrons. 35

Figure 10: The stack of three Timepix detectors allows tracking the particle. A signal path of the serial readout is highlighted [15]. 36

Figure 11: A comparison of two detector arrangements: collimators used (top) and a telescopic structure (bottom). 36

Figure 12: A PE convertor bead placed above the detector Timepix [19]. 37

Figure 13: The integral image (left) is measured with a PE bead in the fast neutron field. Back projection (right) of impact angles determined from individual clusters shows the shape of the bead [19]. 37

Figure 14: The Timepix detector is supplemented by the scintillator and the SiPM. The signal from the SiPM can be used for starting the acquisition. Addition of the scintillator (b) shows more events in comparison to background (a). Starting the acquisition by the SiPM suppress the background significantly [19]. 37

Figure 15: The enhanced double-scatter neutron detector is depicted. Two layers of pixel detectors are coupled to the scintillator. The scintillation light from one scintillator is sensed by a pair of silicon photomultipliers [20]. 38

Figure 16: The quenching cycle of the SiPM avalanche is depicted. The incident light causes the breakdown. The current increases the voltage drop on the quenching resistor and the avalanche is quenched. The conditions get back after the recovery time [23]... 39

Figure 17: Thus schematic diagram shows the parallel connection of the cells in the SiPM. Each cell is composed of the avalanche photodiode and the quenching resistor [23]. 39

Figure 18: Types of SiPMs used at the IEAP and directly by the author are shown. A single pad detector in a ceramic case with through-hole pins is mature technology (a). A thin 4-side tileable SMT case allows to cover large areas (b). A ceramic array with a socket is an appropriate case when more devices should be tested. Unfortunately, it is no longer available (c). Custom-made arrays based on SMT components can be used or adapted according to the application (d). [26], [27], [28] 40

Figure 19: A schematic diagram of the basic element containing the silicon pixel sensor and the monolithic plastic scintillator is depicted. Outer sides are covered by readout electronics. The diagram is not in scale. 42

Figure 20: The block scheme of the new Multi-coincidence system is shown. A bottom part with Timepix and FITPix is used as a state-of-art technology. A plastic scintillator covered by a SiPM array and a following electronic readout will be designed. Synchronization of the two parts can be performed. 43

Figure 21: 2D cross section hit maps of neutron collision points in the scintillator are shown. Only events which fulfilled the condition (deposited energy in the scintillator > 1 MeV and in the pixel detector > 1 MeV) are included. Interaction depth is stated at y axis. Number of events is expressed by the color. The left plot is for the AmBe source while the right one is for 14 MeV monoenergetic neutrons. 46

Figure 22: Spectra of energies deposited in the Timepix by the recoiled protons. The left plot is for the AmBe source while the right one is for 14 MeV monoenergetic neutrons. 46

Figure 23: Wiring diagrams of SiPM readout circuits. Both work as a current-to-voltage converter. The simple one employs a load resistor (left). A transimpedance amplifier allows to decrease a bias current flowing through the sensor (right). 48

Figure 24: This plot shows IV characteristics for two sensors made in different technologies – blue sensitive FC series and green sensitive FM series (retired type). ... 48

Figure 25: IV characteristics of 16 elements of ArraySB-4 show limited uniformity. This issue has to be solved by the design. 49

Figure 26: The graph of temperatures recorded during the dark noise measurement. Blocks labeled by the red dots are those which provided spectra for evaluation. 50

Figure 27: The dark noise spectra measured at specified temperature are shown. Separation of photon peaks is influenced by the noise. Detail of the first photoelectron peak is shown. Spectrum shift is apparent. 50

Figure 28: Graphical representation of the temperature instability is shown. Positions of the photoelectron peaks get lower with the rising temperature and vice versa. 51

Figure 29: A sketch of the temperature measurement is shown. Cosmic rays passing through both triggering scintillators generate signal in the interposed scintillator. Almost all trajectories are perpendicular because of the selective angle. Fulfilled coincidence condition (signals at CH2 and CH3 simultaneously) starts the acquisition. Signal CH1 is then used to generate the spectrum. 52

Figure 30: The plot shows spectra of cosmic rays measured at different ambient temperatures. Shift caused by the temperature dependence of the SiPM is noticeable but negligible in comparison to the resolution. 52

Figure 31: Spectra of Cs-137 in a 1 inch NaI:Tl scintillator measured by two different optical sensors – the photomultiplier tube (top) and the silicon photomultiplier (bottom). The shape corresponds sufficiently although the resolution of the SiPM spectrum is worse (20% against 7% with PMT) and the noise level is higher. 54

Figure 32: An arrangement of VATA64HDR16 pads is shown. Input pads are situated at the left side of the chip. Configuration and readout pads are at the right side of a horseshoe [41]. 57

Figure 33: The diagram of a VATA64HDR16 structure is depicted. A front-end part incorporates 64 analog paths for signal processing. A calibration matrix enables external charge to be fed in the chosen channel. A back-end circuitry handles signal readout through an output buffer [41]. 58

Figure 34: A block diagram of the front-end part of the VATA64HDR16 shows the main functionality of the chip [41]. 58

Figure 35: A readout sequence of VATA64HDR16 is depicted. An external logic is activated by a trigger signal (not shown). Channels are sampled after shaping period and preserved for the whole readout sequence. Clocking the bits through the shift register updates the analog output of the chip. Value of the output corresponds to the value sampled by the particular channel [41]. 59

Figure 36: A block diagram of the interface board is depicted. Main connections are emphasized. 61

Figure 37: A block diagram of the universal chip dongle is depicted. Components and wirings are adapted according to the type of the ASIC. 63

Figure 38: A block diagram of the firmware structure. Blocks correspond to the components in the hierarchical design. 64

Figure 39: A flowchart of the readout sequence is shown. When the starting condition is met, necessary steps are processed to read, convert a transfer data to a computer. 66

Figure 40: A prototype of the SiPM readout system is depicted. It consists of several separated boards. 71

Figure 41: The picture shows the detail of the chip dongle board. ASIC pads are wire bonded to the PCB including input signal pads. The universal Interface board is in the background. 72

Figure 42: An alignment of the silicon pixel detector and the scintillation detector is depicted. It is desired to maximize the overlap of the sensitive volumes. 72

Figure 43: The prototype of the Multi-coincidence system is depicted. A light shielding covers the sensitive volume (the scintillator and the pixel detector) together with FITPix. 73

Figure 44: The main window of the acquisition software is depicted. 75

Figure 45: An example of the text file with ASIC configuration parameters is shown. A structure of the file allows to change the parameters for the particular ASIC..... 75

Figure 46: The ASIC configuration can be done in several ways. Any change is mirrored to all the field. 76

Figure 47: Components for acquisition and mode settings are highlighted. Acquisition overview shows information about the elapsed time, the events count and so on. 76

Figure 48: An example of events recorded in the file. Each line contains timestamp of the event and amplitudes of all 16 SiPM segments. 77

Figure 49: The event window shows two protruding channels. Red points mark connected ASIC channels while the rest is unconnected and red. 77

Figure 50: Window with individual spectra is depicted. Buttons allows to store spectra in several formats. 78

Figure 51: Window shows integral spectrum which is calculated from all connected channels. The range can be adjusted according to the signal magnitude. 78

Figure 52: An example of the event visualized in a matrix configuration is depicted. Segment J measures the highest signal. 79

Figure 53: This picture shows a screen of the newly developed software for the SiPM readout system. 79

Figure 54: Difference between an integral frame and a hit map is shown in 3D plot. Integral frame (left, top) accumulates whole clusters while hit map (right, top) replaces cluster by the dot with the uniform height. Bottom pictures show the detail of the frames..... 81

Figure 55: The main window of the processing software developed for the thesis project is shown. There are two input streams needed to be chosen. Parsing messages are written to the log. A number of events to be processed and a coincidence criterion can be adjusted. Additional filtering conditions can be assigned. The corresponding response of both detectors can be clearly seen. 82

Figure 56: A response of the ASIC to the charge pulse simulated by the waveform generator and a 1 pF coupling capacitor is shown. The waveform shape before and after the pulse is caused by the noise. 83

Figure 57: The output waveform of the ASIC is depicted. A LED illuminated the SiPM array connected to the 16 chip channels of the readout chip. Rectangular stubs correspond to the channel coordinates. Unconnected channels show only the noise superimposed to the pedestal value. 84

Figure 58: Pedestal values of the spectroscopic ASIC are depicted in the plot. The shape has increasing tendency. It is caused by the power supply distribution on the chip. 85

Figure 59: A block diagram of the ASIC structure shows the channel equalization possibilities. The SiPM segment is biased from a common source V_{bias}. The operation voltage V_{sipm} is derived and influenced by the input DAC settings. The amplification affects the trigger count too. The threshold level correction aligns the trigger responses of the channels. 86

Figure 60: Mean values of the spectral peaks generated by the LED are depicted. Two measurements were performed. The gain correction of the ASIC channels was made between them. 86

Figure 61: A noise spectrum is used for the trigger level optimization. The left side peak contains pedestal values while the right side peak accumulates high level events which were triggered by the particular channel. The goal is to balance all channels to get similar area of the right side peaks. 87

Figure 62: Spectra of four individual SiPM segments are depicted. No peaks are noticeable because of the low area of the segments. 88

Figure 63: An integral spectrum obtained by adding up of the digital amplitudes of the individual elements. 88

Figure 64: A 3D visualization of two pairs of matching frames is depicted. A coarse coordinate from the SiPM array roughly corresponds to the fine coordinate in Timepix. 89

Figure 65: The cross section of the experiment with fast neutrons. 90

Figure 66: Integral Timepix frames of the measurement before (left) and after (right) the cluster analysis are shown. In both cases, concentration below one SiPM segment which was chosen to generate a trigger is clearly visible. 91

Figure 67: A comparison of the integral Timepix frames of two measurements triggered by different SiPM segments (marked by a pink rectangle) is shown. 91

Figure 68: Three screens of the processing tool after investigation of the first 100 events of the measurement are shown – integral (left), condition 1 (middle), condition 2 (right). Setting of the conditions, i.e. magnitude of the SiPM signal, is stated in the SiPM frame (top). A missing number means that the segment is not considered. Timepix frames (bottom) show only events fulfilling the condition. Very distant Timepix clusters can be found and can be explained by too benevolent timestamp criterion. 92

Figure 69: Processing of all the events resulted in these records. The integral Timepix frame (bottom, left) is uniformly covered. The SiPM frame (top, left) suffers from limited homogeneity. The condition 1 results (middle) shows symmetric clouds in both detectors. Compared to that, the condition 2 (right) filters events which form an asymmetric group. It is caused by the suppression of the events from the right side element. 93

Figure 70: A sketch of the measurements arrangement (top view). The AmBe source positions are represented by circles. The sensitive volume (a dashed square) is placed to the origin of the coordinate system. Index of the measurement is assigned by the red number 94

Figure 71: The image shows the naming convention established for the conditions definitions. 94

Figure 72: Horizontal and vertical projections of the Timepix integral frame are shown. The vertical projection is fairly symmetrical. This does not apply to the horizontal projection which is influenced by the direction of the incoming neutrons. 95

Figure 73: Coordinates of the center of mass of the horizontal projection are arranged according to the impact angle of neutrons. The monotone trend is evident. 97

Figure 74: The trend is preserved regardless the filtering condition. The average coordinate was calculated and trend equation expressed. 97

Figure 75: A plot of raw values of vertical projections is depicted. There is very broad scale because of diverse coordinates resulting from the filtering conditions. 98

Figure 76: A plot of vertical projections of the four measurements after subtraction of the average shows a good correspondence of three measurements while the fourth one differs significantly because of the different position of the neutron source. 98

Figure 77: The trend of the angular dependence of vertical projections has very limited statistical basis. Only two angles were measured in this direction. 99

Figure 78: Spectra from three individual channels have different shapes. The trigger channel (blue) collects highest amount of light which can be slightly shared by the adjacent channel (red) while the distant channel (green) has no such a contribution. . 100

Figure 79: Error function fit of the threshold region with the fit parameters is shown. 100

Figure 80: The adjacent channel spectrum filled mainly by the noise is fitted by the Gaussian function. 100

List of tables

Table 1: Comparison of different types of optical sensors is summarized in the table. A PIN diode, an avalanche photodiode (APD), a glass photomultiplier (PMT) and a silicon photomultiplier (SPM) are evaluated at basic parameters [25]. 40

Table 2: Positions of photoelectron peaks of four spectra measured at slightly different temperatures. 51

Table 3: Evaluation of cosmic ray spectra. 53

Table 4: A brief summary of parameters of ASICs designed for SiPMs [40]. Not only number of channels but also the output signal type (analog/digital), the input range, features etc. have to be taken into account. 56

Table 5: A table shows the commands used by the system. The left side commands are used for normal operation. The right side commands are implemented for debugging purposes. 65

Table 6: A table shows the structure of transfer packets used for sending data from the hardware to the computer. There is only one header packet followed by several data packets per each event. 67

Table 7: Combinations of the trigger modes of the new SiPM readout system and the FITPix interface define the coincidence operation. 69

Table 8: A project report of the synthesis and PAR of the thesis project VHDL code is shown. Below the half of available resources is consumed by the whole design. 70

Table 9: Results of four measurements are summarized in the table. Centers of mass for horizontal and vertical positions were calculated. Measurement statistics can be found including duration, event rate (number of events of the scintillator) and neutron rate... 96

Table 10: Some parameters of directionally sensitive neutron detection systems are stated and compared to the solution achieved and presented in this thesis (highlighted as red). 101

1. Introduction and Thesis Overview

Ionizing radiation is a common part of the environment we live in since the beginning of the universe. There has been massive progress in the exploration of mechanisms of ionizing radiation in the last century. Together with that new particles were discovered and the understanding of the structure of matter changed significantly. The effort was definitely not slacked down. Newly available technologies caused that detection and evaluation of the ionizing radiation is more effective and contributing and is used in many industry branches (material defectoscopy), in medicine (diagnostics and radio therapy), in security (airports, guarded buildings), in nuclear power plants and so on. Furthermore, wide knowledge about fundamental radiation types causes an increase in requirements. The exhaustive information about an unknown radiation field and particle processes leads to very complex devices employing different detection technologies because there is no ultimate detector which can effectively detect all types of particles.

Especially neutrons can be considered as difficult to detect and to be separated from other particle types. They have no charge which would cause a direct interaction with matter by ionization. Their harmfulness or importance for fission processes make them attractive and challenging at the same time. Detection of the secondary radiation induced by a neutron field distorts the parameters of the primary particles. The simplest information is the presence of the radiation, then its type, energy, direction etc. At least energy and direction of incoming neutrons can't be easily determined.

The motivation of the thesis is to enhance the state-of-art technology for detection of neutrons and provide more complex information than is currently available.

1.1. Research goals

The goal of this thesis is to refine the methodology for detection and tracking of particles in the environment with the special attention given to neutrons. The improvement of the state-of-art technology is based on exploitation of advantages of scintillating and semiconductor detectors in one device. Following tasks are set out:

- Design the structure which is able to detect, recognize and characterize different particle types. The main focus is devoted to position and directional detection.
- Develop the electronic architecture for particle detection with an emphasis on scalability, interoperability and portability. Activation and synchronization of detection units is to be provided.
- Prepare the algorithms for control and processing the measurements and detection evaluation. Elaborate on the coincidence technique and easy-to-use solution.
- Support the concept by the assembled device. Tune up the device performance and test and verify it by practical measurements with radiation sources.

1.2. Thesis structure

Introductory chapters (2, 3, 4) of this thesis serve as theoretical background and provides general information about ionizing radiation, detectors and state-of-art technologies. Terms and principles important for the thesis project are pointed out.

Chapter 5 is devoted to the introduction of the overall concept of the Multi-coincidence system.

Following chapters describe technical details of individual parts used in the design which are the direct contribution of the author. Chapter 6 describes the plastic scintillator and the silicon photomultipliers sensing the scintillation light. Chapter 7 compares integrated solutions for a multi-channel readout of silicon photomultipliers. Chapter 8 is focused on the system employing the spectroscopic ASIC. Chapter 9 is devoted to the firmware of the FPGA. Chapter 10 shows the appearance of the designed prototype. Chapter 11 describes the acquisition software and the data processing tool.

Last two chapters, number 12 and 13, summarize and compare results of measurements performed during the whole development.

2. Ionizing radiation

Ionizing radiation is the radiation which is capable to ionize the surrounding material. The source of the ionizing radiation can be natural processes or human activities or instruments. The complex knowledge about the radiation is essential for estimation of threats.

The ionizing radiation can be classified by many of its parameters. The combination of a type, energy and others influences the behavior in matter [1]. This work does not aim to the exhaustive definition of the types same as their detailed categorization. But it is appropriate to briefly mention the basic groups with pointing out the importance for this work.

2.1. Heavy charged particles

Heavy charged particles are protons, alphas and fission fragments. Common property is charge and mass of one atomic mass unit or greater. It makes heavy charged particles very reactive with matter through Coulombic forces. The effect is as high as heavy the particle is (fission fragments are most reactive).

There are two processes to be mentioned. Both start with a heavy element such as uranium, polonium, americium, californium etc. The process of creation of the alpha particle can be described by the formula (1) and the fission fragment follows the formula (2)

$$ {}^{A}_{Z}X \rightarrow {}^{A-4}_{Z-2}Y + {}^{4}_{2}\alpha \tag{1} $$

$$ {}^{A}_{Z}X \rightarrow F1 + F2 + (2-3){}^{1}_{0}n + Q \tag{2} $$

where X is the initial nuclear specie, Y,F1, F2 are the final species or fission fragments and Q is the amount of energy released by reaction.

Energy of resulting alpha particles is always discrete and very well known so they are very often used for calibration of the detectors. On the other hand, fission products are created asymmetrically making their energy blurred.

Other sources of heavy charged particles are accelerators. A container with gas such as hydrogen, oxygen, carbon dioxide and many others provides stable medium. Ionized gas is accelerated by an electric field so the energy of particles is very well defined and tunable. It is another way of detector calibration and it is very valuable for the wide range of possible conditions.

Recoils are the last process of originating of heavy charged particles needed to be mentioned. A particle hits the lattice of the target material and transfers part of its energy to the bound particle which escapes the lattice and continues through the material. The energy of the escaped particle is dependent on the impact angle. This process needs to be stressed out because it is important for this work. Further details about that will be examined in the following chapters.

All heavy charged particles are highly interacting. The trajectory of the particle is straight because the high mass ratio. The energy of the particle is decreasing with the distance in the absorber. The maximum distance is lower for heavier absorbers and lower particle energy. The energy loss increases as the charged particle's momentary energy decreases. This behavior is described by Bragg curve. Empirical equations are determined, such as for alpha particle in the air (3)

$$R_{air} = 0.31 \times E_{\alpha}^{\frac{3}{2}} \qquad for\ 4\ MeV < E_{\alpha} < 7\ MeV \tag{3}$$

where R_{air} is the particle range in centimeters and E_{α} is the alpha energy in MeV.

The maximum distance for different particles, energies and absorbers can be obtained by special calculation tools.

2.2. Light charged particles

Light charged particles are electrons and positrons. Electrons are created by a beta decay of the relevant radioisotope and it applies analogically for positrons. This process can be described by the formula (4)

$$^{A}_{Z}X \rightarrow {}^{A}_{Z+1}Y + {}^{0}_{-1}\beta^{-} + {}^{0}_{0}\bar{\nu} \tag{4}$$

where X and Y are the initial and final species and ν is the antineutrino.

An energy spectrum of resulting beta particles is always continuous because the initial fixed decay energy is shared with a neutrino.

The mass of a beta particle is equal with the mass of orbital electrons in the target material so the trajectory is significantly influenced by interactions. The range of penetration is almost always lower than the total particle trajectory. The straightness of the trajectory increases with the energy and in the lighter absorber. While the interactions has statistical basis, a number of particles going through the absorber is highly dependent on the absorber material and has an exponential distribution according to the equation (5)

$$N(x) = N(0)e^{-nx} \tag{5}$$

where N(x) is the number of electrons leaving the absorber, N(0) is the number of electrons entering the absorber, n is the absorption coefficient and x is the material thickness.

From the point of view of this work, this group of ionizing radiation is the less interesting so details can be fairly omitted.

2.3. Electromagnetic radiation

Electromagnetic radiation is the set of charge-less radiation with extensive categorization. Because of the principle of the corpuscular-wave dualism it could be

considered as gamma particles or gamma rays. The gamma radiation is generated during de-excitation of products of decays, e.g. beta decay, fissions, during annihilation of a positron or when acceleration affects electrons (bremsstrahlung, synchrotron radiation). Excitation can be caused even externally such as X-ray fluorescence.

The energy spectrum of electromagnetic radiation can be both discrete and continuous depending on the process of generation. Discrete energies have, for instance, decays or annihilations.

There are three groups of interaction mechanisms of electromagnetic radiation according to its energy:

- Photoelectric absorption – low energy radiation interacts to atom, the whole energy is deposited
- Compton scattering – reaction of middle energy radiation with an electron, the angle of the collision defines the amount of transferred energy
- Electron-positron pair production – radiation of energy higher than 1.02 MeV

It should be noted that the interaction of the electromagnetic radiation has statistical basis. The interaction mechanisms are competitive to each others. Furthermore, the absorber material affects the processes (see Figure 1).

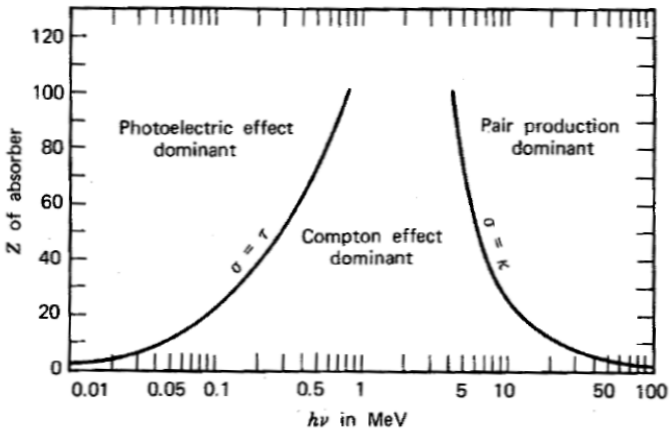

Figure 1: The graph shows the contributions of the three competitive processes of interaction in matter. The probability of the individual process is highly dependent on the energy [1].

Electromagnetic radiation is a significant part of a natural background. Unfortunately, it is generated by excitation of the surrounding material. In the majority of experiments it is unwanted effect that needs to be suppressed. It applies for this work too. The solution for gamma recognition and separation is described in following chapters.

2.4. Neutrons

Neutrons are particles with no charge and mass similar to protons. Their neutrality makes them very difficult to detect. Binding energy of a neutron is higher than the common natural excitation. Therefore neutrons are rare in comparison to gammas.

One of the production processes of neutrons is fission of nuclei of heavy elements, such as californium, see equation (2). Another source of neutrons is interaction of particles. This can be further distinguished according to the initiating particle type like alpha, gamma or accelerated ions. The very common examples of the first group are laboratory radioisotope sources AmBe or PuBe. The second one is preferred because it does not contribute by own gamma radiation although it has slightly lower yield per unit mass. The neutron generation mechanism is illustrated by equation (6)

$$ {}^{4}_{2}\alpha + {}^{9}_{4}Be \rightarrow {}^{12}_{6}C + {}^{1}_{0}n \tag{6} $$

Higher neutron energies can be obtained by accelerating incident particles. Two significant reactions of deuterium have to be mentioned, see formula (7) and (8). They are used in even portable and tunable neutron generators.

$$ {}^{2}_{1}H + {}^{2}_{1}H \rightarrow {}^{3}_{2}He + {}^{1}_{0}n \tag{7} $$

$$ {}^{2}_{1}H + {}^{3}_{1}H \rightarrow {}^{4}_{2}He + {}^{1}_{0}n \tag{8} $$

Energy spectra of neutrons are continuous for fission and alpha interactions and discrete or almost discrete for gamma and accelerated particles interactions. In principle, accelerated particle induced neutrons can be slightly tuned in terms of energy and flux.

Neutron radiation can be divided in groups according to the energy from ultra-cold (lowest energy) to ultra-fast (highest energy). This work is focused on region of fast neutrons with energies in order of MeV which is expected range for fission products. The introduced AmBe source and D-T reaction can be used and mentioned in following chapters of this work.

An interaction of the neutrons in matter is highly dependent on the energy. A different detection approach is needed for specified energy ranges because the cross section can vary by factor of 1000. Because of the absence of the charge, neutrons can't be detected directly similarly to electromagnetic radiation. Low energy neutrons are mainly detected by nuclear reactions of conversion materials like ^{6}Li, ^{10}B or ^{157}Gd. The secondary radiation (gamma, heavy charged particles) is detected. The energy depends on the reaction Q-value.

High energy neutrons have high cross section of elastic scattering with light materials where the recoiled particles are created. The transformation itself inserts uncertainty of the angle of collision so the transferred energy has statistical basis. The energy of the recoiled particle follows equation (9)

$$ E_R = E_N \left(\frac{4 M_N M_R}{(M_N + M_R)^2} \right) cos^2 \varphi \tag{9} $$

where E_R is the energy of the recoiled particle, E_N is the energy of the primary neutron, M_N is the neutron mass, M_R is the mass of the target material and φ is the interaction angle.

The ratio of the neutron mass (M_N) and the mass of target material (M_R) limits the highest possible transferred energy. Hydrogen based materials have mass ratio close to

one so full range of energies can be obtained (from 0 to E_N). Only fraction of energy is transferred in heavier targets.

3. Ionizing radiation detectors

A detector of ionizing radiation is a device capable to interact with the radiation and provides information about that interaction. There are plenty of types, design solutions, processing algorithms and output responses of the detectors. Huge effort has been spent to obtain the best detection tool. Unfortunately, properties of different radiation types do not allow to find the ultimate solution. Brief classification of the most common detectors is following:

- Gas chambers – They are containers with gas filling of particular conditions, such as pressure. Incident particle ionizes the originally neutral gas. It increases the conductivity of the gas. The electric field caused by the applied voltage determines the behavior of the chamber. Advantage of gas chambers is possibility to make high detection volumes. Disadvantages are necessity of gas encapsulation, granularity and slow response.
- Scintillation detectors – A scintillator is a material which is able to convert particle energy to low energy photons, simply said the light. Parameters like light yield, decay time, emission wavelength etc. of the light pulse are influenced by the composition of the material. The amount of scintillation light corresponds to the absorbed energy.

  - Inorganic crystals (NaI:Tl, LaBr, YAP, LuAG etc.) withstands higher temperatures, have higher light yield, higher detection efficiency because of the higher density, are often hygroscopic, demanding for production of defect-free lattice and suffer from long afterglow.
  - Organic crystals (anthracene, stilbene, naphthalene), organic liquids (toluene, benzene with additives) and plastics (polyvinyltoluene and polystyrene with additives) has fairly high light yield and very quick response without significant afterglow. Especially plastics are attractive for high volumes, simple mechanical processing and price.

- Solid-state detectors – These detectors are made from solid material, very often semiconductors. So this group is also called semiconductor detectors. The most used semiconductors are silicon and germanium. Recently, the manufacturing process was improved for binary semiconductors - gallium arsenide and cadmium telluride. High purity germanium detectors have extraordinary energy resolution. They are used in sensitive laboratory instruments like large volume gamma spectrometers. The price for the best performance is a need of cooling (liquid nitrogen is recently replaced by Peltier cooling). Silicon is used as a standard material for its well-handled technology. It can be used in room temperature. Different shapes and thicknesses with various structures can be prepared. Disadvantage is lack of large volume solutions and relatively low density making the silicon transparent for electrons and high energy gammas. This space is covered by GaAs and CdTe.

Development of ionizing radiation detectors is still ongoing as new technological capabilities arise. It is desirable to be familiar with novel technologies. In this work two

types of detectors and detection principles are used: a semiconductor silicon detector and a scintillation detector.

3.1. Detection structure optimization

Until now the detector was considered mainly from a material point of view. Detection characteristics are dependent on mechanical structure too – size, thickness, segmentation, surface finishing etc. There are two different detection principles which have to be considered separately when the detector improvement is desired.

Scintillation materials convert the deposited energy to the light which spreads isotropically (exception can be found for crystals). In the most cases the light is not the quantity that is directly processed. The real system has to employ some kind of photosensor which converts the light to an electrical signal. It is not possible to influence the trajectory of the light so the amount of collected light gets lower proportionally to the area covered by a photosensitive device. Some improvement can be achieved by modification of unused surface by application of reflective of refractive layer. On the contrary, the transparency between the scintillation material and the photosensor is to be as good as possible. An optical liquid/gel is used to minimize the difference in refractive indexes. Furthermore, high volumes have negative impact on the light collection because of the limited transparency of the material. Final shape of the scintillator and possibly segmentation is always dependent on application needs.

Semiconductor detectors, often with a p-n junction, have electrodes to apply the bias voltage. The impacting particle generates the charge that is directly sensed by dedicated electronic circuits. The collection time decreases with the higher bias voltage same as probability of charge recombination during that time. The quality (purity, lattice disorders) of the silicon is currently not the issue. On the other hand, the very well-handled manufacturing process allows to create advanced structures. The granularity of the detector in order of micrometers is achievable. Position and direction sensitivity is then available. According to the segmentation the following groups can be determined:

- Single pad – Only one sensitive element is in the volume. Size can vary from sub-millimeter values to more than centimeters. It is simple to operate, only one bias and one signal path is needed. Spectroscopic resolution can get worse with larger area (effect of larger capacity). Can be considered as position sensitive when the area is small.
- Strip detector – Strip shaped elements are integrated to one volume. The total sensitive area is divided same as the capacity of the individual element so the noise is reduced. The length-width ratio is up to the use. Each sensitive element needs to have own signal path to preserve position information. The precision depends mainly on strip pitch (spacing factor). Assuming the pitch small enough, the charge sharing effect (see Figure 2) and induction effect appears. The advanced multi-channel electronic is needed to take advantage of the structure. The possibility to situate the electronics aside the sensitive volume predestine it to use it in the telescopic configuration.

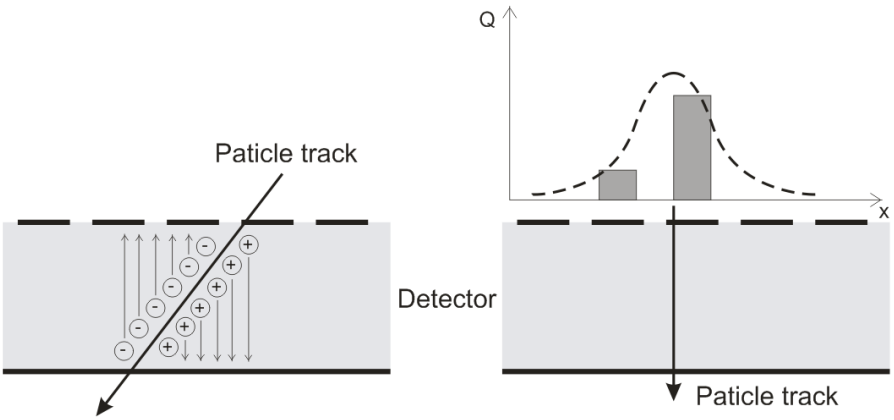

Figure 2: An illustration of the deposition of the charge depending on the particle trajectory angle (left) and the position of interaction (right) [2]. The particle going through the detector can deposit charge which is collected into more than one strip. Interpolation and fit of the charge distribution improve the spatial resolution.

- Pixel detector – The matrix of elements is the basis of pixel detectors. The size of pixels can go down to tens of micrometers. In comparison to strip detectors, 2D position information can be obtained. The effect of charge sharing and induction is registered too. The concept of a matrix predestines utilization of integrated electronics in close contact to the detector (see Figure 3). The closed geometry and usually small pixel size further decrease the noise. On the other hand, the electronics are exposed to the same radiation field which can be harmful in high fluxes. Current abilities of electronics industry allow to prepare sophisticated processing for each pixel.

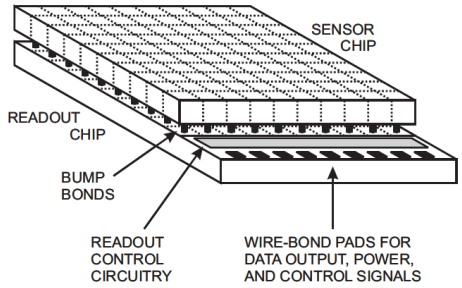

Figure 3: A schematic view of a pixel detector is depicted. The pixelated sensor is attached to readout electronics. The electrical contact is provided by bump-bonding technology [2].

Semiconductor pixel detectors are the most capable detection structures so far. They offer high granularity and high level of integration allowing find the very compact solution for radiation detection. The pixel detector is one of the fundaments of this work.[1]

[1] The author finds appropriate to be noted that he devoted not strictly to pixel detectors. He got acquainted with single pads and strip detectors during the PhD study. However these projects are not related to this thesis ([NT1], [NI1], [NF2], [NF4] or [NF7]).

3.2. Processing of the signal from the detector

An inseparable part of the detection system is signal acquisition, processing and reconstruction. Semiconductor detector provides the electric charge proportional to the absorbed energy. The first stage of a signal path is a preamplifier. This part is not omissible and is structurally almost same for all semiconductor detectors. It is a high input impedance circuit with a gain. From electrotechnical point of view, it is a transimpedance amplifier with a FET at the input. This circuit is susceptible to noise so the design has to take it into account. The output signal from the preamplifier is a low impedance signal and can be handled as ordinary analog signals.

Different situation occurs when a scintillation detector is employed. Scintillation light is proportional to the absorbed energy. An optical sensor collects the light and converts it to an electrical signal. Following types of optical sensors are mainly used:

- Photomultiplier (PMT) – A conventional photosensor exploiting multiplication effect of accelerated electrons. A bias voltage in order of hundreds volts is required. However the size of a PMT gets smaller it still occupies few cubic centimeters. A photomultiplier usually provides high enough voltage pulses so no special impedance matching is required. Length of a pulse can reach few nanoseconds that could be challenging for following stage.
- Avalanche photodiode (APD) – It is a kind of photodiode working in the avalanche region. It has lower gain in comparison to a PMT. A lower bias is needed to reach the avalanche regime. Complex electronics are used for a signal readout and avalanche quenching. In principle, a small size and integrable device can be made.
- Silicon photomultiplier (SiPM) – A novel type of photosensor was developed as a descendant of an ADP. It overcomes the low gain of the APD and implements a simple resistor-based quenching circuit. It further decreases a bias voltage to order of tens of volts. The output signal can be sensed as a voltage pulse on a load resistor. Its resistivity together with an operation point can increase the signal to comfortable values. It is the favorable solution for compact devices because it is component-size sensor.

In some cases there can be desired to use some additional circuit after an optical sensor such as an amplifier or a buffer. The requirement results from specific needs of the application.

The following second stage is mutual for both semiconductor and scintillation detectors. The shaping amplifier provides the additional gain and simultaneously limits the signal bandwidth that results in the increased signal-to-ratio. Signal shape can be changed significantly. Both parameters are strictly application-specific depending on the input signal type and the output signal processing. The second stage is to be a linear circuit.

The last acquisition part provides the desired information. Based on the signal from a detector and a predefined threshold the counting can be performed as the simplest processing. A conversion of the analog amplitude to a digital form by a multichannel analyzer creates the spectrum. Distribution of the radiation energies gives

better information about the radiation field. Complex structures enrich the spectroscopic information about segment address, timestamp of the event etc.

The processing chain influences the overall performance of the system. Following terms can be used to describe the detection precision and limiting factors. Precondition for the highest optimization of the detection system is to be limited mainly by the detector, not the acquisition part.

Resolution – It defines the precision of the detection. The response to the monoenergetic radiation is limited by the charge generation in the detector and the noise of the processing chain. The detector resolution is frequently given by FWHM (full with at half maximum) of the spectrum peak (see Figure 4).

Pile-ups – When two independent interactions happen in very close moments the pulses overlay (see Figure 5). Depending on the processing algorithm the spectrum may be distorted. While the charge generation and collection is quite fast (not true for high volume detectors) the main originator is a processing circuit. There is only limited change how to get over this issue, for instance decrease the shaping time, but it can have negative impact to the resolution.

Dead time – There is some time needed to process each event. During this time no new events can be recorded and they are lost. While the pile-ups are rather related to analog processing, the dead time is influenced by digital acquisition. The clear example is limited data transfer speed of the interface or insufficient amount of memory allocated to store the data.

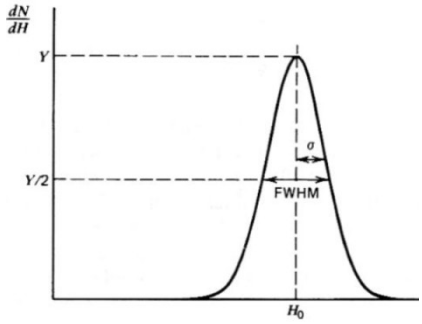

Figure 4: The accuracy of the system is evaluated by FWHM of spectrum peak [1].

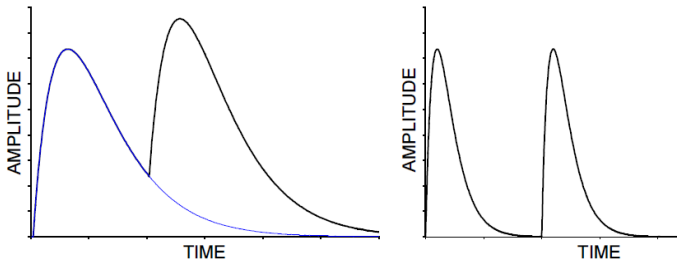

Figure 5: Shaped pulses pile-ups cause spectrum distortion when shaping is too long (left). Decreased shaping (right) has no such an effect [2].

4. The state-of-art ionizing radiation detectors

There is no doubt the most advanced ionizing radiation detectors are pixel detectors. Much effort was put in the development in last decades and still continues. Both parts, the detector and the readout chip, are influenced by new ideas and technological possibilities. The detector material changes from silicon to heavy materials (CdTe, GaAs) for higher gamma detection efficiency. Increasing thickness allows to use detectors in high energy physics and space applications. Moreover, new detector structures can be found [3]. Readout technology is highly optimized for performance, power or typical usage of the pixel detector.

In spite of that, there is still need of utilization of scintillation detectors. Investigation of new materials and improvement of a manufacturing process make the resolution better and production more reliable. Fortunately, new technologies also affected means usable for light detection so new scintillators can be used even in areas where the conventional photomultipliers were an obstacle.

4.1. Pixel detector Timepix

Pixel detector Timepix is widely used in the Institute of Experimental and Applied Physics (IEAP). Together with the technology itself many years of experience, algorithms and processing tools make it the ideal platform for further refinement presented in this thesis.

The Timepix [4] detector belongs to the family of pixel detectors made in the Medipix collaboration at CERN [5][2]. It is the high-end hybrid device developed for imaging, although particle detection is available too. This pixel detector can operate with different sensor materials while the read-out chip is still same. The sensor is bonded directly to the read-out chip. The front-end cell size corresponds to the sensor pixel size. The area is $55 \times 55\ \mu m^2$. Each Timepix cell consists of 549 transistors which create analog processing (amplification and discrimination) and conversion to digital value. The channel uniformity can be adjusted by the 4-bit threshold adjustment register. The digitized information is stored in the 14-bit shift register which provides the interface to all the cell communication. See the block scheme in Figure 6. The big disadvantage is absence of self-triggering so the detector itself does not provide information that the particle came. This drawback will be solved in the next generation of the chip.

[2] History of the development of Medipix chips can be found in this website, same as parameters and features of the chip generations.

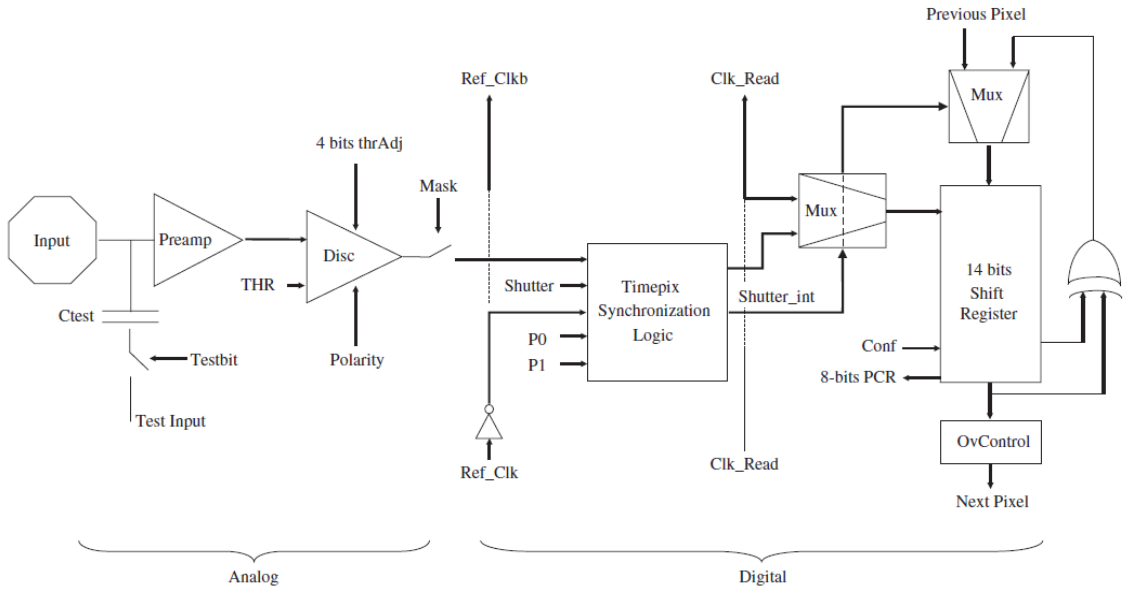

Figure 6: Block scheme of the Timepix cell. Two parts can be distinguished. The analog signal is amplified and compared to the threshold voltage. Digital conversion depends on the chosen mode of the operation [4].

There is 65536 pixels in total organized in matrix 256 × 256. The sensitive area is about 2 cm^2 (1.4 cm × 1.4 cm). The whole detector (the readout chip and the sensor) is slightly bigger than the sensor because of readout bonding pads situated at one side of the chip. The control and interface circuitry is common for all the pixels. Reading data in and out of the chip is performed through dedicated shift registers. Each pixel can be independently configured to one of the three modes (see Figure 7):

- Counting mode – The pixel counts the number of events when the signal exceeds the threshold value during the active shutter interval. This behavior is same as the behavior of the classical Medipix chip.
- Time-of-arrival mode – The counter is incremented since the first particle energy steps over the threshold till the end of the shutter signal.
- Time-over-threshold mode – The counter is incremented only when the analog signal is higher than the threshold voltage and the shutter signal is active. In this mode the count corresponds to the amplitude of the signal so the energy deposited in the pixel.

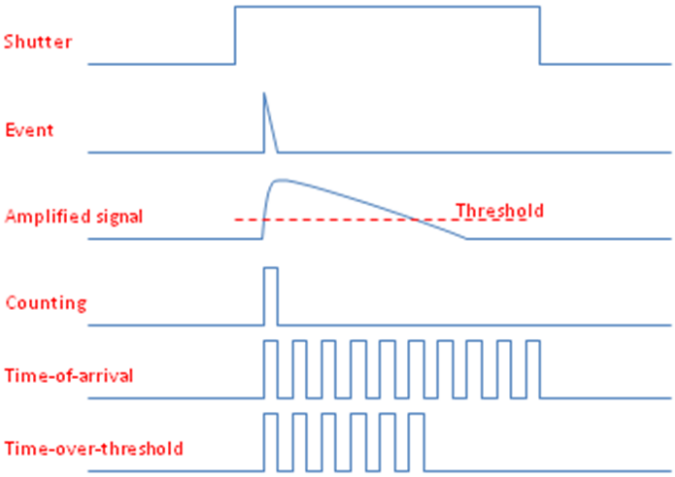

Figure 7: Typical waveforms of Timepix modes. The shutter has to be active to enable particle detection. The amplified signal is compared to the threshold. The counting mode increments the register when the signal crosses the threshold. The time-of-arrival mode counts clock periods till the end of the shutter. The time-over-threshold mode accumulates the clock pulses when the signal is above the threshold.

Operation of the detector is controlled by the interface FITPix [6] and the software Pixelman [7].

Equalization and calibration

Despite the well-managed production process the uniformity of pixels is limited. The fault can be caused by both parts, the detector and the readout chip. The detector is influenced by a quality of the substrate material or manufacturing processes such as polishing. The consequence of the imperfections is a higher noise and a leakage current. The readout chip contains the analog part (a charge sensitive amplifier and a shaping amplifier) which suffers from limited reproducibility same as ordinary analog circuits – transistors or operational amplifiers.

For uniform response across the detector the compensation circuits implemented in the readout chip are available. Threshold equalization can be adjusted in range of 4 bits. In case of significant disorder the problematic pixel can be masked [8].

Energy calibration is another process needed for proper detector response [9]. This is a very common task which has to be done with any spectroscopic detector. Unfortunately, the ionizing radiation detection is influenced by the detector itself. Small pixel volume causes that the charge generated in the detector can be shared by more pixels, especially for high energies and heavy particles.

Charge sharing and particle recognition

The charge generated by the particle is collected by the electric field induced by the applied bias. The charge carriers travel from the point of interaction to the electrodes along the field and respect its course. The bias voltage is significant determination factor (see Figure 8). The direction and the type of particle are also important. In general, the charge sharing effect is noticeable in high granularity sensors like pixel and strip detectors. Other processes like charge diffusion and charge induction influences the charge collection, thus the response of the detector [10], [11].

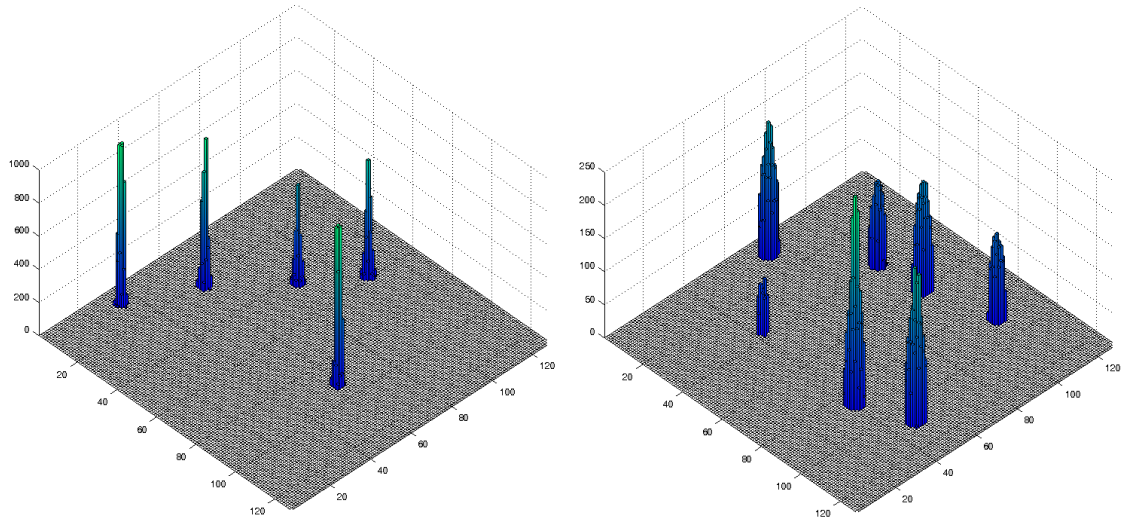

Figure 8: 3D visualization of pixel detector response (protons recoiled by fast neutrons) at two different bias voltages is depicted. Event clusters measured with bias of 20 V are high and narrow (left) while low 5 V bias allows the charge to spread out to more pixels (right).

The charge sharing effect can be even advantageous in some cases [12]. The pixel detector Timepix has saturation limit of the pixel preamplifier about 1 MeV [13]. If the charge is higher than this value, spectroscopic information is lost. Otherwise, the charge collected by one pixel is a fraction of the totally deposited charge which can be higher than the pixel charge range. Furthermore, the distribution of the charge detected by adjacent pixels is characteristic for different radiation types [14]:

- Dots – minimum ionizing particles (MIPs), relativistic electrons, gammas
- Long straight tracks – relativistic particles
- Curly tracks – electrons
- Large blobs – protons, alphas and other charged particles

Two example of the response of the detector Timepix to different radiation types can be seen in Figure 9.

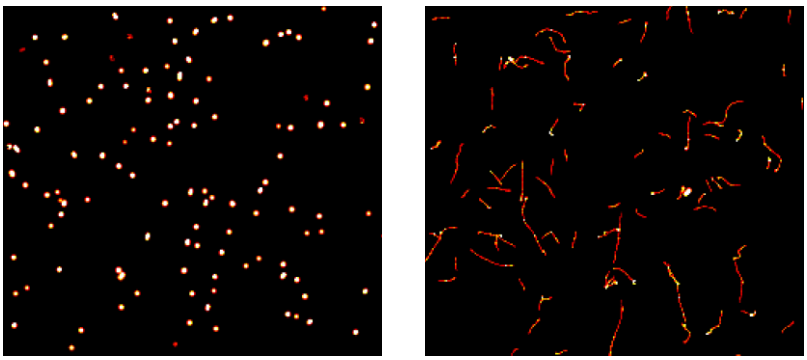

Figure 9: Integrated frames measured by pixel detector Timepix in different radiation fields. Heavy charged particles (left) significantly differ from long tracks (right) made by fast electrons.

Unfortunately, there is still uncertainty in the recognition of the external radiation field. For instance, high energy gammas can generate the positron-electron pair or neutron, regardless if fast or thermal, interacts with convertor and generates heavy

charged particles. These secondary particles can't be distinguished from the same primary radiation.

Advanced structures with Timepix

The stacking of the pixel detectors was introduced by the IEAP [15]. Such an arrangement, which can be seen in Figure 10, provides the third coordinate (the layer coordinate is added to the 2D information from the pixel detector). A telescopic configuration is used for tracking purposes very often regardless the detector technology [16], [17], [18]. Information about the direction of the impacting particle is determined by the straight line interleaving the hit points in the pixel detector. In general, few requirements need to be fulfilled:

- The particle passing through the detection layer has to be recorded. It means the deposited energy has to be high enough to overcome noise and threshold levels.
- The source of particles has to be situated in the field of view of the telescope. In principle, even two layers are enough for direction evaluation. It makes the field of view very wide.
- The particle has to be capable of passing through the detection layers. The particle interaction should not be influenced. The energy lost in the inactive materials (readout chip, air gap) should be low enough not to stop the particle. It can be accomplished by high energy particles.
- All the system has to be synchronous from the point of view of the particle interactions. Only events detected in the same (or very close) moment should be interleaved and taken into account. Otherwise, false detections will degrade the results.

Despite the complexity, the telescopic arrangement of detectors is much powerful way in comparison to usage of collimators which suffers from high weight and decreased detection efficiency (see Figure 11).

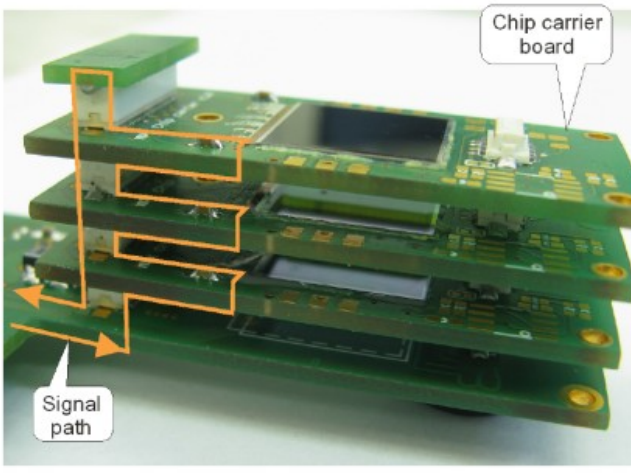

Figure 10: The stack of three Timepix detectors allows tracking the particle. A signal path of the serial readout is highlighted [15].

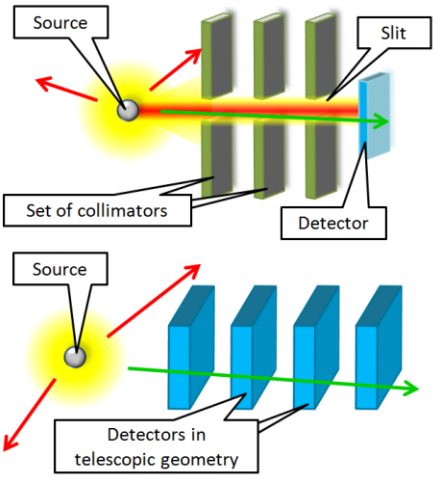

Figure 11: A comparison of two detector arrangements: collimators used (top) and a telescopic structure (bottom).

Regardless the limitation of a telescopic structure, it is the way how to obtain more complex information about the radiation field. The detection efficiency is as high as available with one detector. In this thesis, only one pixel detector is utilized but the overall concept aims to the telescopic arrangement and the design reflects this demand.

Neutron detection with Timepix

The detector Timepix allows separating events on the basis of the radiation type. The weak point is the neutron detection. The detection efficiency directly in silicon suffers from a very low cross section. The measurement of the angular and energy response with a polyethylene (PE) bead used as a neutron convertor (see Figure 12) was published [19]. The integrated data shows the homogenous irradiation of the whole detector. In spite of that, the back projection of the impact angles depicts the bead shadow (see Figure 13).

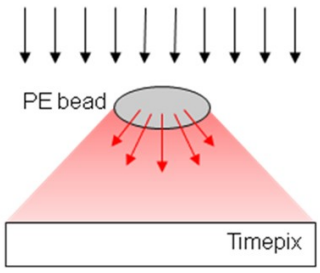

Figure 12: A PE convertor bead placed above the detector Timepix [19].

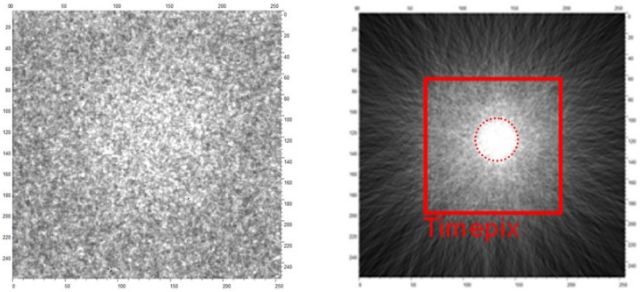

Figure 13: The integral image (left) is measured with a PE bead in the fast neutron field. Back projection (right) of impact angles determined from individual clusters shows the shape of the bead [19].

The neutron field is always accompanied by other types of radiation. The Timepix is also sensitive to electrons or gammas. The usage of the hydrogen rich plastic scintillator and the SiPM (see Figure 14) decreases the background by proper knowledge of the neutron interaction moment. The triggering signal starts the acquisition as a consequence of neutron-hydrogen collision. The acquisition window can be optimized to suppress non-neutron events. Three different measurements can be compared (see Figure 14). The first image shows the background measurement. When the converter covering some part of the detector is added, the significant pattern appears because of presence of the recoiled nuclei. The triggering by scintillation light removes the background significantly and the shadow of the converter can be recognized.

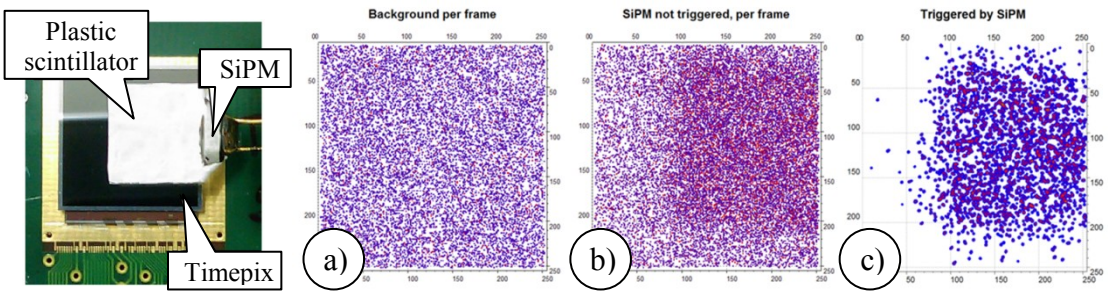

Figure 14: The Timepix detector is supplemented by the scintillator and the SiPM. The signal from the SiPM can be used for starting the acquisition. Addition of the scintillator (b) shows more events in comparison to background (a). Starting the acquisition by the SiPM suppress the background significantly [19].

Usage of the active scintillating converter was further refined by combining with the Timepix stack structure (see Figure 15) [20]. More sensitive layers increase the detection efficiency and provide data with multiple recoils. Signals from two optical sensors (silicon photomultipliers) attached to the scintillator can be processed in coincidence to exclude false detections caused by the dark noise.

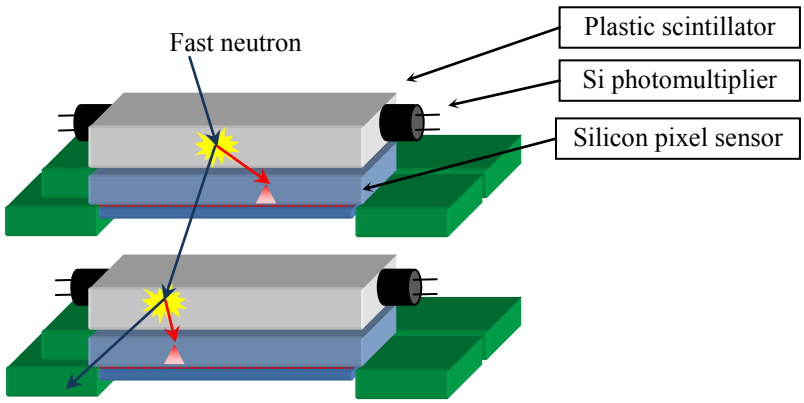

Figure 15: The enhanced double-scatter neutron detector is depicted. Two layers of pixel detectors are coupled to the scintillator. The scintillation light from one scintillator is sensed by a pair of silicon photomultipliers [20].

4.2. Silicon photomultipliers

The silicon photomultiplier (SiPM) is an advanced light detector with outstanding parameters in comparison to previous technologies. The concept was patented in 1996 [21]. Since that time this perspective technology is under development. There is many manufacturers focused on this issue, some are fully dedicated, some have SiPMs as a part of their portfolio. Few examples can be mentioned: Hamamatsu, SensL, Ketek, Zecotek, ST Microelectronics or Philips. Different terminology can be found in the community. Manufacturers use own titles very often although the fundament is still the same. Other terms like a multi-pixel photon counter (MPPC), a solid state photomultiplier (SSPM) or a geiger-mode avalanche photodiode (GAPD) can be found. Further development aims to the improvement of parameters and integration of the readout logic directly to the chip [22].

Only the term silicon photomultiplier (SiPM) is used in this thesis and in author's speech because it is the preferred name in the community.

The principle of operation of the SiPM is derived from avalanche photodiode (APD). The reverse bias voltage induces the electric field across the junction of the APD. It is high enough to allow avalanche generation thus multiplication of the primary stimulus. There are two main sources of the stimulation – the impacting light which is the object of the interest and thermally generated events creating so called dark noise. The ordinary APD is used in the complex circuit which is responsible for quenching the avalanche. This is caused by lowering the bias voltage. The indicated gain of the APD is about 100.

On the contrary, the SiPM simplifies the quenching by the implementation of the quenching resistor directly in silicon. It is an inseparable part of the device close to an

avalanche photodiode. The applied bias voltage is then shared by the quenching resistor and the photodiode with the ratio depending on the operation point, temperature etc. When the SiPM is in the dark, all the events are generated thermally. These events (a dark noise) cause the current (a dark current) flowing through the SiPM. This current makes the voltage on the internal resistor. The remaining voltage on the junction decreases and the electric field decreases too. The lower electric field generates fewer avalanches and reduces a dark noise. This process results in the equilibrium. Graphical representation of the process can be seen in Figure 16. External photons impacting the SiPM break the equilibrium and the stabilization process repeats. The incident light can be measured as a current pulse flowing through the device. The feedback suppresses the avalanches. Strong lighting can be considered as high amount of close pulses. In this case, the electric field remains weak and new equilibrium is found. In this situation, the SiPM can't measure the light but the protection against the burnout is guaranteed.

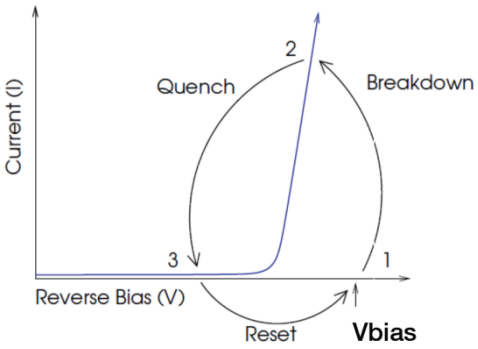

Figure 16: The quenching cycle of the SiPM avalanche is depicted. The incident light causes the breakdown. The current increases the voltage drop on the quenching resistor and the avalanche is quenched. The conditions get back after the recovery time [23].

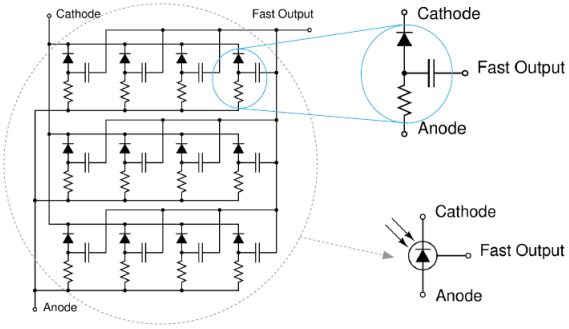

Figure 17: Thus schematic diagram shows the parallel connection of the cells in the SiPM. Each cell is composed of the avalanche photodiode and the quenching resistor [23].

The quenching effect described in the previous paragraph takes some time (recovery time). During this period the avalanche photodiode is in the unknown state and should not be fired again. The dark noise is dependent not only on material quality but on the size too. The reasonably large devices (in order of square millimeters) would be inhibited by a thermal noise, as in the case of strong lighting. The SiPM is therefore composed of high number of cells. Each cell is the small APD with a quenching resistor. These cells are connected in parallel and contribute to the overall operation (see Figure 17). The size of a cell is in order of square micrometers. When the photon starts the avalanche in the particular cell, it is inhibited for the duration of the recovery time. Other cells are able to react to impacting photons. Fired cells contribute to the resulting current pulse. There are hundreds or thousands of cells in the current devices regardless the total size or manufacturer.

The quenching and the cell structure are the main features of the SiPM but more advantages can be found (see Table 1). As the new technology it is compared to others very often. It can't be said that a SiPM can completely replace other optical sensors, particularly photomultiplier tubes [24]. Focusing on advantages can blind an unbiased judgment. There are disadvantages which have to be taken into account and properly considered during the development.

Table 1: Comparison of different types of optical sensors is summarized in the table. A PIN diode, an avalanche photodiode (APD), a glass photomultiplier (PMT) and a silicon photomultiplier (SPM) are evaluated at basic parameters [25].

	PIN	APD	PMT	SPM
Gain	1	10^2	10^6	10^6
Operational Bias	Low	High	High	Low**
Temp. Sensitivity	Low	High	Low	Low
Mechanical Robustness	High	Medium	Low	High
Ambient light exposure?	OK	OK	NO	OK
Spectral range	Red	Red	Blue/UV	Green
Readout / Electronics	Complex	Complex	Simple	Simple
Form factor	Compact	Compact	Bulky	Compact
Large area available?	No	No	Yes	Yes
Sensitive to magnetic fields?	Yes*	Yes*	Yes	No
Noise	Low	Medium	Low	High
Rise time	Medium	Slow	Fast	Fast

** Due to the requirement for the external electronics to be located close to the detector*
*** SPM from SensL, having an operational bias of 30V, meet the requirements of the Extra Low Voltage directive*

There are many types of physical appearance of silicon photomultipliers (see Figure 18). The latest trend is the production of large-area devices.

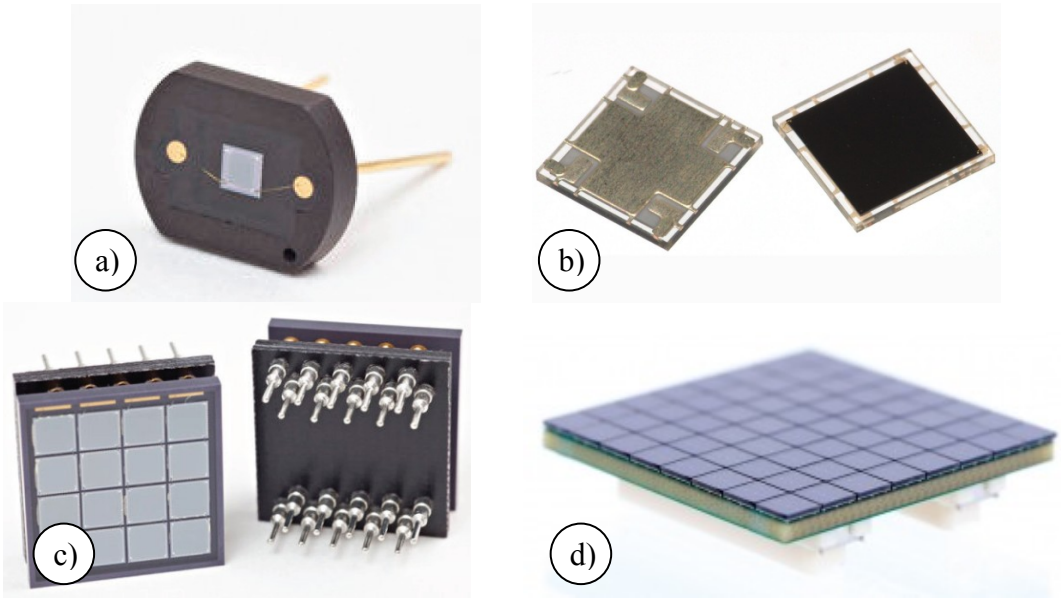

Figure 18: Types of SiPMs used at the IEAP and directly by the author are shown. A single pad detector in a ceramic case with through-hole pins is mature technology (a). A thin 4-side tileable SMT case allows to cover large areas (b). A ceramic array with a socket is an appropriate case when more devices should be tested. Unfortunately, it is no longer available (c). Custom-made arrays based on SMT components can be used or adapted according to the application (d). [26], [27], [28]

5. Design of the Multi-coincidence system

In the following chapters the contribution of the thesis is described. Its aim is to extend the state-of-art detection system according to the recent experience. The utilization of the most modern technologies is desired.

The Multi-coincidence system is meant to be the complex system able to detect, recognize and characterize different radiation fields. Various detectors sensitive to different radiation types have to be used for reasons mentioned in chapters 1 and 2. The simultaneous operation of all detectors brings the complex information about the radiation. Increasing the sensitivity to the desired radiation and suppression of the unwanted events increase the information yield of the measurement. Coincidence operation allows to adapt the measurement mode according to the particular needs so recognize the particles in the background signal, reduce the amount of data for offline processing and decrease the dead time of the system. The new Multi-coincidence detector system is based on the principles summarized in chapter 4.

5.1. Requirements of the system

The new design has to offer the universal solution which provides as much information about the measurement as possible without need of repetition of the measurement. This is the advantage in unknown radiation fields when data are processed and analyzed offline to get the complete characterization. The basic event filtering on hardware level is to be implemented. This is the efficient way when looking for the particular radiation. The architecture takes it into consideration that various detectors and devices could be part of the system [RP2]. The concept must not be limiting for future development.

To fulfill the goals of the thesis the design has to provide following features:

- Particle tagging – The incoming particle generates the signal which is further processed. The form of acquisition of the event can vary. Fast information about the particle detection can be used to start the acquisition or takes part in more complex logical condition.
- Position of detection – The place of interaction in the detector allows to reconstruct the path of the initial particle and consequent processes. Also determination of the detector is needed in case of multi-layer. The position information is to be available for offline processing. Online position investigation in not required.
- Event timestamp – The moment of the event detection is to be determined. The system is designed as a synchronous one so the data can be matched. Events detected in the same moment can be considered as these originating from one particle. Event tracking is then available.
- Deposited energy measurement – The energy lost in each sensitive volume is to be measured including conversion materials. Insensitive objects between detectors are to be reduced.

- Particle recognition – Different response to radiation types in the detectors and reconstruction of the trajectory defines the originating particle, although the secondary radiation is detected.
- The direction of the particle – The impact angle of the incident particle is to be defined if the detection principle allows that. If the particle trajectory in the detector is influenced by the interaction itself and the impact angle is not reliable the event is to be marked for discarding.

Fulfilling these requirements needs a complex structure based on more independent devices. A stackable structure and possibility of multiplication of the layers increase the sensitive volume without any influence of position resolution. This was taken into account in this project. The design should also be compact, portable and fully remotely configurable through a computer.

5.2. Structure of the sensitive layer

The basic element of the design of the Multi-coincidence system is not the only one detector but the composition of the silicon pixel detector and the plastic scintillator. Thus, the sensitive volume contains two materials with different characteristics. There is a minimum of insensitive materials between the sensitive ones, mainly formed by an air gap. On the outsides, there is readout electronics.

Figure 19 shows the diagram of the basic element. A silicon pixel detector is in close geometry to a plastic scintillator. A charge deposited in the silicon sensor is processed by the Timepix readout chip. A monolithic piece of the plastic scintillator is covered by an array of silicon photomultipliers. All the area of the scintillator is sensed. The largest side is used to increase the light yield.

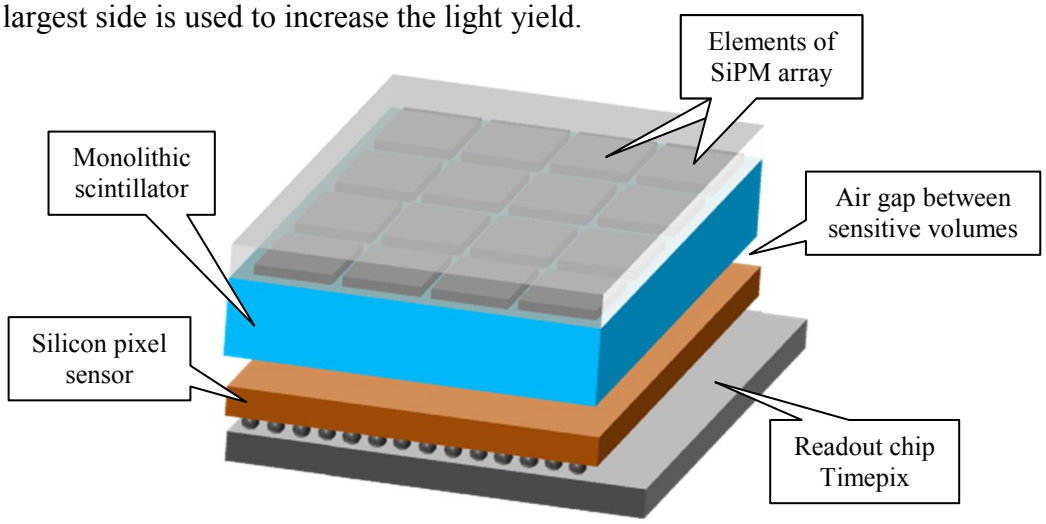

Figure 19: A schematic diagram of the basic element containing the silicon pixel sensor and the monolithic plastic scintillator is depicted. Outer sides are covered by readout electronics. The diagram is not in scale.

The pixel detector Timepix together with its readout is a fairly closed system. The main effort presented in the thesis was put into processing of the light from the scintillator and the development of the system synchronization.

5.3. *System design*

The Multi-coincidence system is an architecture consisting of a silicon detector and a scintillation detector working in close cooperation (see Figure 20). A silicon detector part is fully covered by Timepix, FITPix interface and Pixelman software. Managing the plastic scintillator needs to be solved together with the system synchronization. Separation of the system into two parts has following advantages:

- Timepix and FITPix part can remain unchanged and be used as a verified block. Only the interface signals are used for data synchronization.
- Development of a scintillator readout system is not constrained by any existing architecture. Any requirement can be taken into account during the development.
- A newly designed system for the scintillator readout can be used as a standalone device. Other projects, where pixel detector would be unsuitable, could exploit it. Thus, the benefits of the work go beyond the thesis project.
- Even in the case of a complete Multi-coincidence system, the parts may be used independently. The variability of the system is higher.

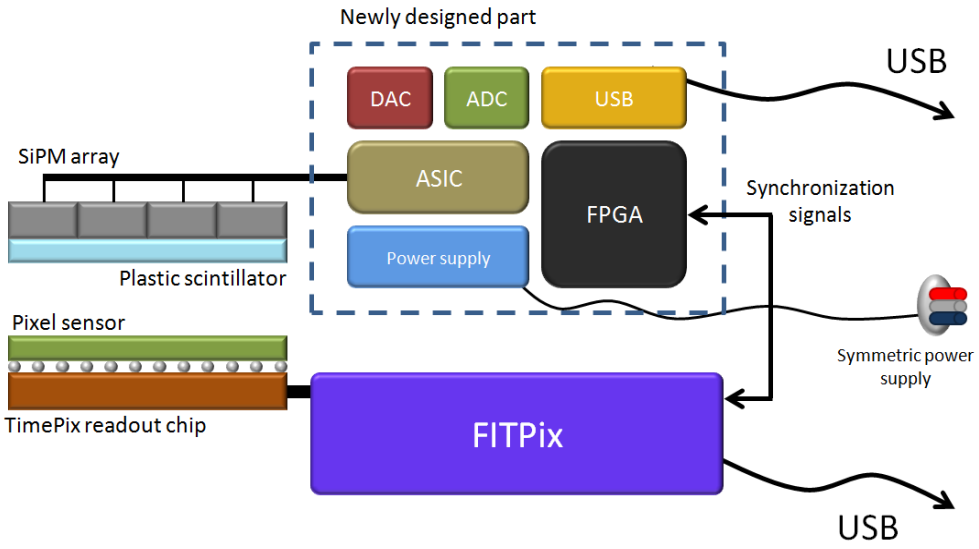

Figure 20: The block scheme of the new Multi-coincidence system is shown. A bottom part with Timepix and FITPix is used as a state-of-art technology. A plastic scintillator covered by a SiPM array and a following electronic readout will be designed. Synchronization of the two parts can be performed.

The new readout part for a plastic scintillator employs an application specific integrated circuit (ASIC) which process signals from an array of silicon photomultipliers. Control and operation of the ASIC and the rest of the system is implemented in a field programmable gate array (FPGA). Its firmware defines the behavior but allows addition of new features in future when needed. Analog signals from the ASIC are converted in an analog-to-digital converter (ADC). These data are handled by the FPGA to a computer through a universal serial bus (USB). Setting of the ASIC is defined by a user from the computer software. Commands decoded in the FPGA are sent to the ASIC through digital signals or as analog voltages generated in digital-to-analog converter (DAC). The system is supplied by a symmetric source. Voltages needed by different parts of the system are derived on the board. A bias voltage for the SiPM array is provided on the board too. Synchronization of both parts

is ensured by signals between FITPix and the FPGA in the new readout. At least two signals are needed: a trigger signal from the FPGA to FITPix to start the data acquisition of the pixel detector and a busy signal from FITPix to the FPGA to inform about occupancy of the pixel detector. A coincidence regime needed for the data synchronization requires the new scintillation part to work as a master device.

Software is also part of the project. Because the design needs to be controlled by the user, the proper tool has to be made. The functionality of the user software supports setting of the hardware, control the measurement and accept the data for visualization and storage.

There are two independent streams – pixel detector data acquired by Pixelman software and associated plug-ins and scintillator data from the newly developed system or software tool. To prove the desired functionality the basic offline processing algorithm is presented as a part of this thesis.

The following chapters are devoted to detailed description of the parts of the system.

6. Scintillator & SiPM array

A scintillator converts the deposited energy to the light. It can be expected that the conversion is linear. Because the light is not processed directly the silicon photomultiplier is employed to convert the light to the electric signal. Although each of them has its own characteristics and parameters the performance is highly influenced by their mutual contact. Stable results are not guaranteed if any change is made, for instance separation and attaching again. This fact limits the possibility to test the components separately and with that knowledge predict behavior of the joint piece. The performance has to be verified in the final setup.

The thin plastic scintillator with the array of silicon photomultipliers was employed in the thesis project. The final solution is described in detail.

6.1. Plastic scintillator

With respect to goals of the thesis the plastic scintillator is used. It is light material with low stopping power that makes it usable in the telescopic configuration. It has high cross section for fast neutrons in comparison to heavier materials. It is suitable for machine processing so any shape can be prepared. It is stable in a standard environment without any encapsulation. There are many types of organic solid scintillators. With respect to the application, there are no specific requirements.

The thin 0.7 mm slab of polystyrene-based scintillator is used. The base material is enriched by organic luminophores to achieve emission wavelength of 420 nm. There are two additives to be mentioned: 2% pTP and 0.03% POPOP [29]. Despite the general approach when the scintillator is covered by reflective material (mylar foil, Teflon tape, titanium dioxide etc.), no coverage is used in the project because this would restrict or even stop the recoiled proton. The contact side is polished and covered by a silicon grease BC-630 for better optical contact.

The scintillator material was chosen as the optimal solution according to the experience at Institute of Experimental and Applied Physics [30], [31], [32].

Scintillator thickness optimization

A scintillator thickness is a compromise among several demands. The overall concept needs both the interaction in the scintillator and the detection of the recoiled proton which left the scintillator in the silicon detector. It means the path in the scintillator has to be long enough to generate sufficient amount of light. This requires rather thick slab. On the other hand, the range of the recoiled proton is limited. Furthermore, the recoiled proton must have enough energy for detection in the silicon detector so thinner scintillator is preferred. The expected energy range of the device influences the maximum transferred energy according the equation (9). Thicker scintillator can cause worse light transmission although this effect can be estimated as very low in comparison to the others. The required directional detection prefers thin slab which, on other hand, decreases the detection efficiency.

The basic estimation can be done using projected range calculators, such as SRIM [33]. It shows that the scintillator of the selected type and thickness can be penetrated through by protons of energy over 8 MeV. Any proton with lower energy has limited ability to reach the successive silicon detector. In other words, low energy protons can be successfully recoiled only from smaller part of the slab. This energy range is acceptable for the project. Other ranges are provided in Appendix A which shows data obtained from the SRIM calculator.

For such a complex situation the simulation of the mentioned effects is desired. Monte Carlo simulation was prepared by Lukáš Fajt, author's colleague from the IEAP. The geometry was defined according to the assumed geometry of the prototype device. The purpose of the simulation was to confirm the correctness of the chosen scintillator and investigate the distribution of the interaction points in the scintillator. Energy spectrum of AmBe source (up to 10 MeV, mainly about 4 MeV) and monoenergetic neutrons from D-T reaction (14 MeV) were used as a simulation input. There were 10^7 events generated to narrow angle surrounding the detector. About 5×10^6 events hit the detector. Various energetic detection thresholds were set. The example of simulation results showing the number of interactions in the individual depths of the scintillator using 1 MeV threshold for both the scintillator and the pixel detector can be seen in Figure 21. Spectra of energies deposited in Timepix by the protons recoiled from the scintillator by neutrons are shown in Figure 22.

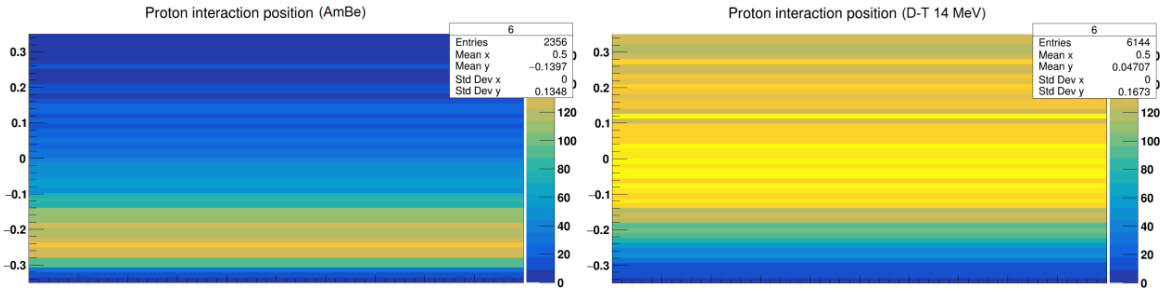

Figure 21: 2D cross section hit maps of neutron collision points in the scintillator are shown. Only events which fulfilled the condition (deposited energy in the scintillator > 1 MeV and in the pixel detector > 1 MeV) are included. Interaction depth is stated at y axis. Number of events is expressed by the color. The left plot is for the AmBe source while the right one is for 14 MeV monoenergetic neutrons.

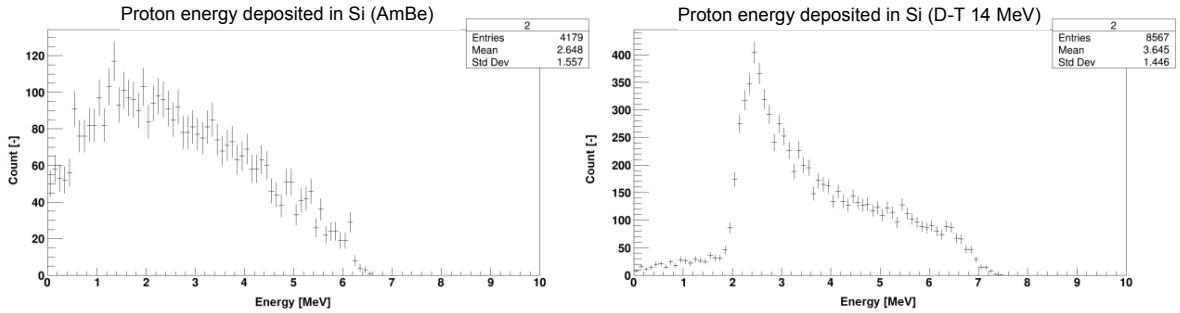

Figure 22: Spectra of energies deposited in the Timepix by the recoiled protons. The left plot is for the AmBe source while the right one is for 14 MeV monoenergetic neutrons.

The information asset obtained from the simulations is as follows:

- There is an insensitive part of the scintillator which does not provide enough light to exceed the threshold chosen to separate events from the noise. Even for 1 MeV threshold the insensitive volume is small.
- Thickness of the scintillator 0.7 mm is sufficient for energies of the AmBe source. Increasing the thickness has no positive effect.
- A thicker scintillator can be used to increase the detection efficiency when higher neutron energies are expected.
- A silicon detector 300 μm does not allow to deposit energy over 7 MeV because of the recoiled proton range in the silicon (Appendix A). Overall energy distortion can be suppressed by a thicker sensor when needed.
- Detection efficiency calculated as a ratio of number of primary neutrons and number of events fulfilling the condition (over 1 MeV deposited in a scintillator, over 1 MeV deposited in a silicon) is 4.7×10^{-4}.

The choice of detectors parameters strongly depends on the desired application. The advantage of the design is that optimization of the sensitive layers for different incoming energies is possible in future without influence of the overall concept.

6.2. Array of silicon photomultipliers

Selection of a silicon photomultiplier is influenced by many factors. As it is new technology, there was lack of experience available in the research team. This corresponds to the amount of time devoted to get acquainted. During the work on the thesis author got experience mainly with SensL products and marginally with Hamamatsu products too. They have slightly different behavior but the detailed description is beyond the scope of this thesis.

The thesis related activities were mainly performed with SensL B-series (no longer available) and C-series devices [34] which became available during the work.

Readout circuits

The SiPM is essentially a device providing a current pulse proportional to the incident light. A current-to-voltage conversion is needed to make the signal suitable to the acquisition system. Amplification is not always needed. Two circuits can be mentioned: resistor load and transimpedance amplifier (see Figure 23). A bias RC filter is obligatory in any case because of very high sensitivity to a bias noise. Choice of the resistor value is not unrestricted. The lower value has lower noise suppression. On the other hand, the higher value similar or higher than the quenching resistor value has negative impact to the temperature stability. A load resistor defines the voltage of the output pulse. Increasing the value increases the voltage level (up to order of hundreds of millivolts) that makes the signal directly suitable for the acquisition. Unfortunately, it prolongs the pulse length and can result in reflections on conducting lines. A transimpedance amplifier is favorable when a current floating through the SiPM is to be low. Furthermore, integrated solution is always based on the amplifier front-end.

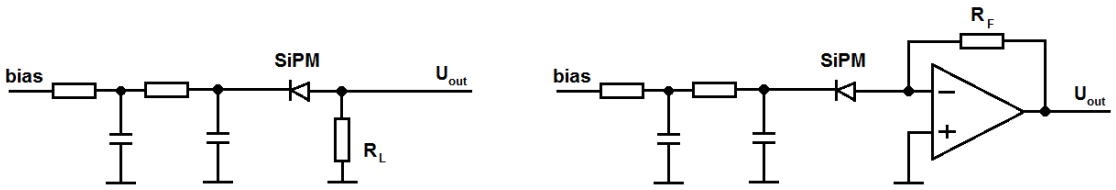

Figure 23: Wiring diagrams of SiPM readout circuits. Both work as a current-to-voltage converter. The simple one employs a load resistor (left). A transimpedance amplifier allows to decrease a bias current flowing through the sensor (right).

The most of performed measurements for getting experience with SiPMs were done with a resistive load. The simplicity of the circuit doesn't have a negative impact on the operation of SensL SiPMs.

IV characteristics

Choice of the operation point (i.e. bias voltage) of the SiPM strongly depends on the application, particularly a scintillator light yield, an energy range and a desired level of the output signal. The bias voltage influences the avalanche so the amplification. Furthermore, a noise level changes too. There can be found some limitations for both the low limit (no avalanche is generated) and high limit (device overloaded). The typical value of the breakdown voltage of the particular type is available in the datasheet. This value can be used as the initial value for further optimization.

IV curves for two different sensors were measured. Both devices have a similar structure: dimensions 3 × 3 mm^2, cell size 35 µm, but the technology is different. Older M-series (FM) is manufactured in the N-on-P technology with a peak wavelength over 500 nm. Newest C-series (FC) is based on P-on-N technology (same as B-series) resulting to a peak wavelength about 420 nm which is more suitable for scintillators. Different characteristics are noticeable in Figure 24. Switching to a new device therefore requires slight changes in the configuration.

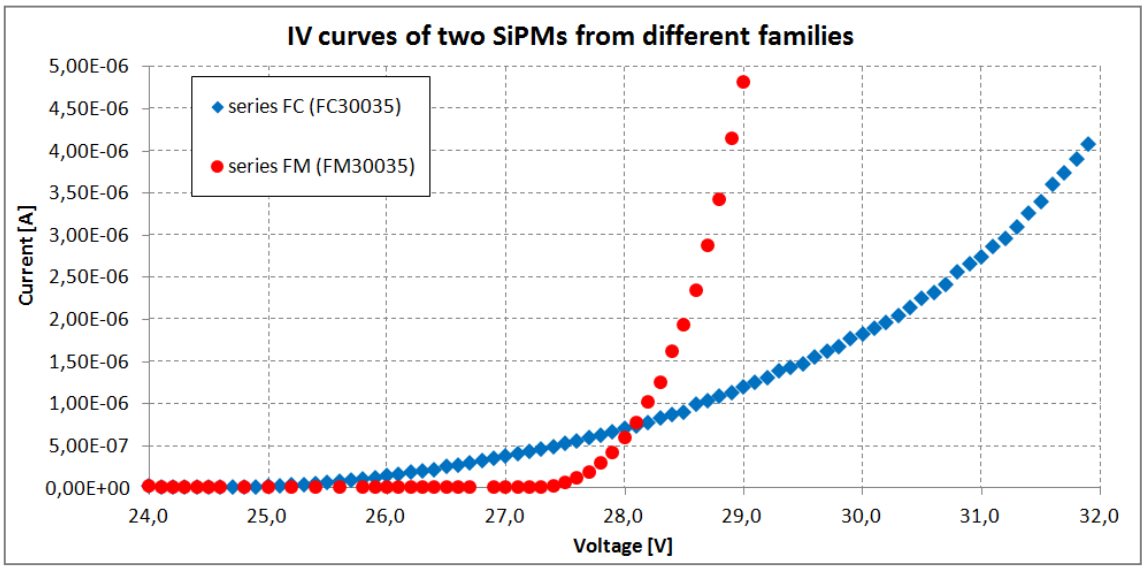

Figure 24: This plot shows IV characteristics for two sensors made in different technologies – blue sensitive FC series and green sensitive FM series (retired type).

An array sensor ArraySB-4 has 16 elements, each of size $3 \times 3\ \mathrm{mm}^2$. The uniformity of elements declared by the manufacturer is better than 1:1.5. Comparison of IV characteristics shows the difference (see Figure 25). This has to be taken into account during the development [RF3]. The element-to-element matching is addressed in next chapters.

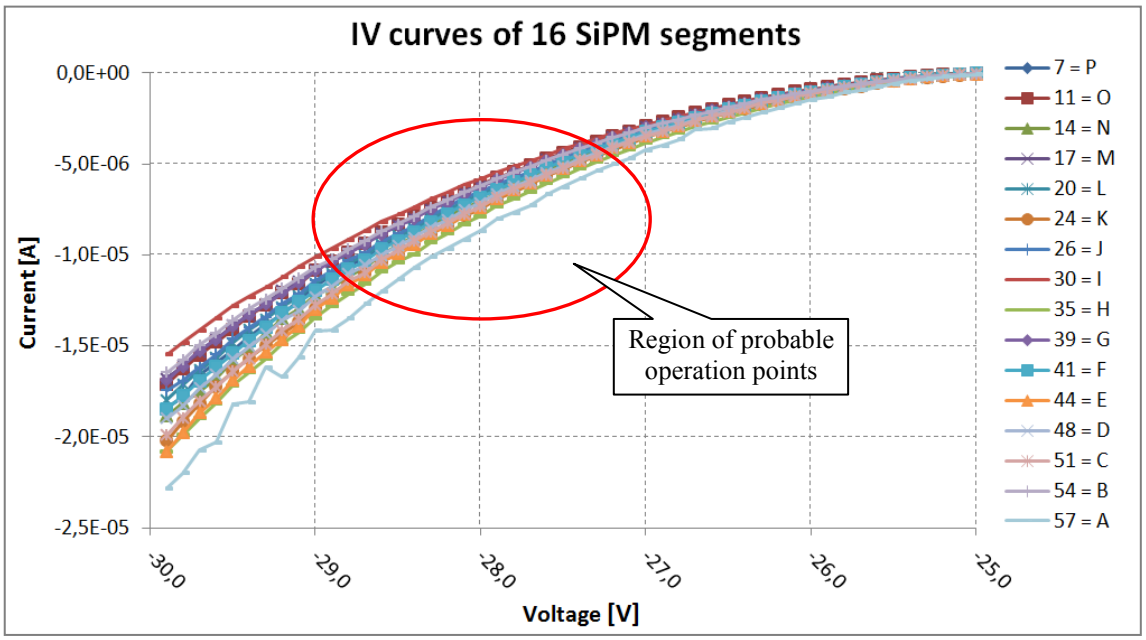

Figure 25: IV characteristics of 16 elements of ArraySB-4 show limited uniformity. This issue has to be solved by the design.

Temperature stability

Temperature instability is frequently mentioned deficiency of SiPMs. The referred breakdown voltage is about -20 mV/°C. Due to the indefinite definition of the breakdown voltage the gain dependence of -0.8% is more relevant [35]. The influence of this instability depends on the expected temperature range and the resolution of the scintillator (or another light source).

There is a huge effort put in the stabilization of the gain. Many approaches can be found in papers [36], [37], [38]. That is a consequence of the integrated quenching resistor.

The temperature dependence was tested by the measurement of photoelectron spectra. Ordinary way is to trigger both the light (LED, laser) and the acquisition system. The amount of light has to be in order of photons that is achieved by absorption foils or other suppression means (distance).The resulting spectrum shows peaks whose distance is 1 photoelectron. This approach is usable for the initial calibration but not always. Sometimes, the mechanical requirements significantly reduce the possibility to illuminate the detector. Another approach based on the dark noise was investigated. There is no need to employ any light source and the measurement is not triggered externally. The principle is based on the assumption that thermally generated avalanches are evoked separately enough to distinguish the number of photons. This requirement is fulfilled by the lower bias voltage (device is not overloaded) and high-quality technology (accomplished by contemporary devices).

Series of measurements were performed in the laboratory. Dark noise spectra were stored each 5 minutes together with temperature. Figure 26 shows that the temperature changed a little. Four spectra were chosen for further evaluation and comparison (see Figure 27).

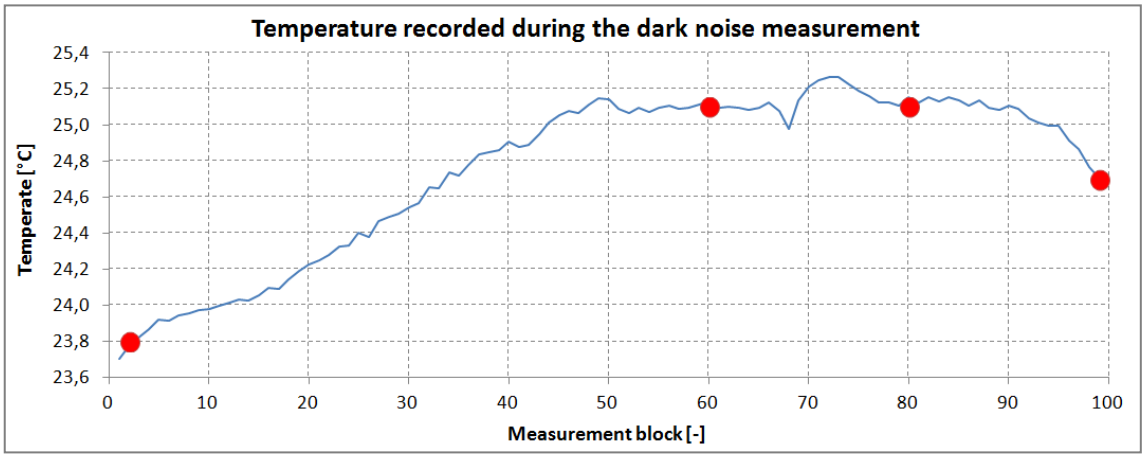

Figure 26: The graph of temperatures recorded during the dark noise measurement. Blocks labeled by the red dots are those which provided spectra for evaluation.

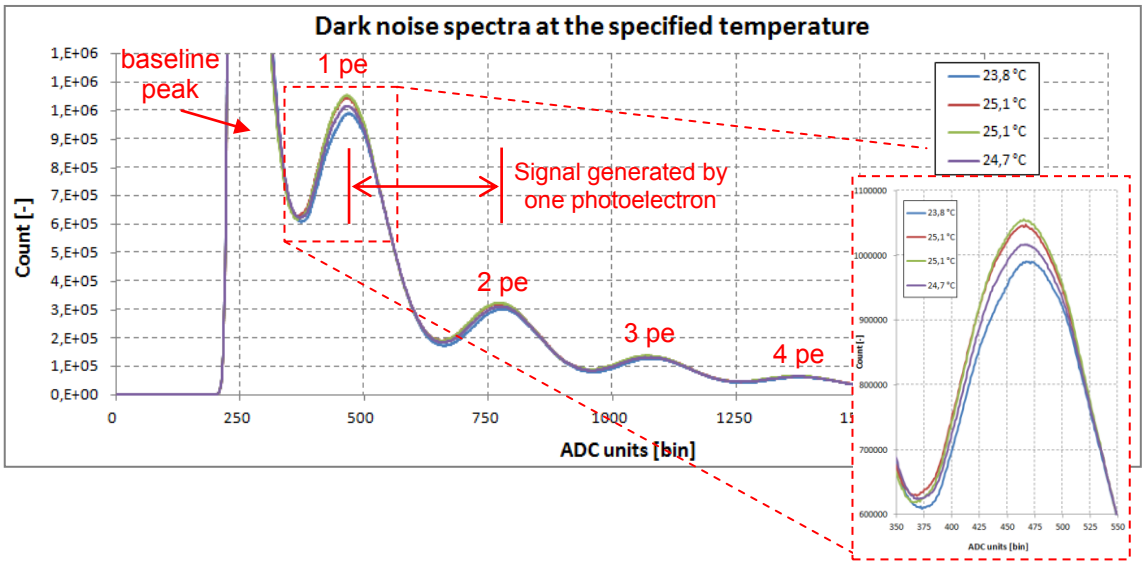

Figure 27: The dark noise spectra measured at specified temperature are shown. Separation of photon peaks is influenced by the noise. Detail of the first photoelectron peak is shown. Spectrum shift is apparent.

More detailed analysis of the dark noise peaks shows the shift even when the temperature changed only slightly. First four photoelectron peaks was fitted and summarized in Table 2 and plotted graphically in Figure 28. The difference is very low but noticeable.

Table 2: Positions of photoelectron peaks of four spectra measured at slightly different temperatures.

	Temperature [°C]	Peak mean coordinate [-]			
		Peak 0	Peak 1	Peak 2	Peak 3
Mesurement 1	23,8	468,4	778,3	1080,7	1376,8
Mesurement 2	25,1	465,1	770,6	1068,3	1371,5
Mesurement 3	25,1	464,6	770,5	1067,2	1371,9
Mesurement 4	24,7	466,5	776,6	1073,0	1373,9

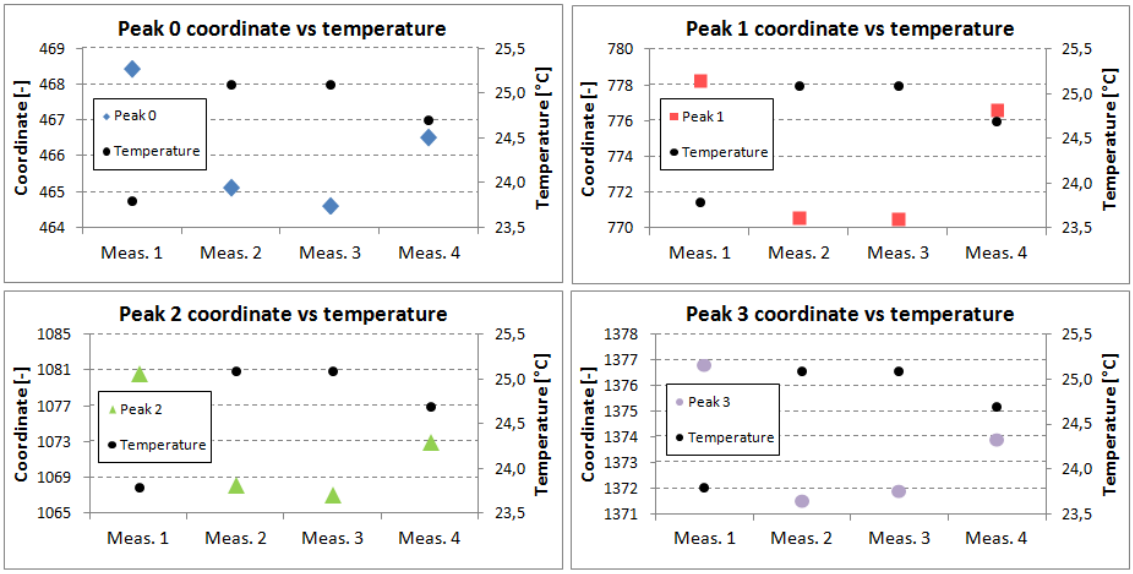

Figure 28: Graphical representation of the temperature instability is shown. Positions of the photoelectron peaks get lower with the rising temperature and vice versa.

The advantage of this approach is that the functionality can be implemented to the standard acquisition system. It can work in parallel to the ordinary data readout. There is no need to perform previous calibrations. Despite all the positives the disadvantage has to be mentioned. This procedure has high demands on data throughput. It can be fulfilled with difficulties by the common or complex readout systems[3]. It should be pointed out that trigger level is embedded in the noise and the event rate can goes up to millions of events per second. Events generated by the external radiation are then in significant minority and the measurement time has to be increased to get reasonable statistics. This fact did not permit to exploit this procedure to the thesis project.

The spectral shift in the final application is the important parameter. It is expected that SiPM is highly temperature dependent but the effect has to be considered in the relation to other parameters, such as resolution and expected temperature range of use. The measurement simulating expected temperature conditions was performed. To avoid uncertainties of a light source or a position radiation source, cosmic rays were used. Triggering by two small area scintillators defines a narrow angle, so the trajectory of the

[3] A custom-made 100 MSPS ADC module [NF9] was designed by the author during the work on PhD thesis. It aims to replace traditional crate-based acquisition modules by a portable solution and to provide more capable device for spectroscopic needs. Multi-channel sampling system [NF8] for the anti-neutrino detector is based on the module.

cosmic rays in the detector. Dispersion of the deposited energy is almost discrete. Events when both triggering scintillators provide signal in coincidence (CH2 and CH3) are acquired. Light from the interposed 1 cm thick scintillator plate is detected by the tested SiPM whose signal amplitude is used for generating the spectrum (see Figure 29). Two long term measurements at different temperatures (16 °C and 30 °C) were made.

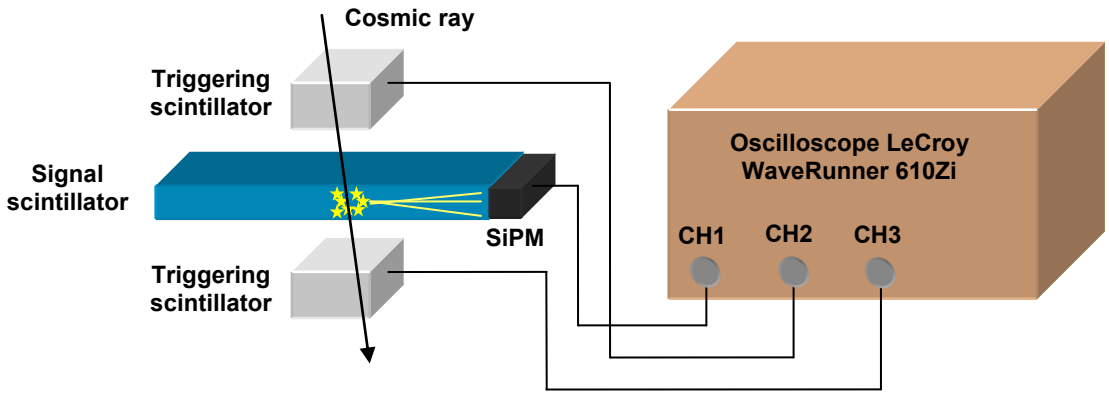

Figure 29: A sketch of the temperature measurement is shown. Cosmic rays passing through both triggering scintillators generate signal in the interposed scintillator. Almost all trajectories are perpendicular because of the selective angle. Fulfilled coincidence condition (signals at CH2 and CH3 simultaneously) starts the acquisition. Signal CH1 is then used to generate the spectrum.

Recorded spectra are shown in Figure 30. The shift of peaks is noticeable. Evaluation of spectra is summarized in Table 3. The measured temperature coefficient of the SiPM is in correspondence to the value referred by SensL (manufacturer), about 0.8%/°C. In this case, the temperature shift can be safely neglected when compared to the resolution of the scintillator. The resolution is dependent on the scintillator shape and the quality of the light transfer to SiPM [39] so there is legitimate prerequisite that the resolution of the thesis project scintillator could be better – about 20-30%.

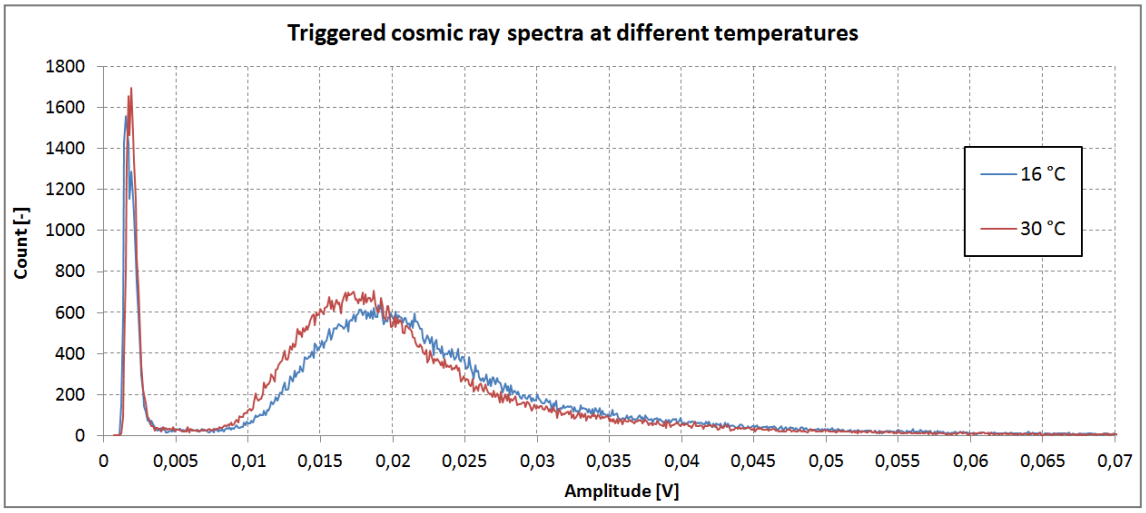

Figure 30: The plot shows spectra of cosmic rays measured at different ambient temperatures. Shift caused by the temperature dependence of the SiPM is noticeable but negligible in comparison to the resolution.

Table 3: Evaluation of cosmic ray spectra.

Temperature [°C]	Noise [V]	Peak [V]	Distance [V]	FWHM [V]	FWHM [%]
16	0,0015	0,0192	0,0177	0,0122	68,9
30	0,0018	0,0178	0,0160	0,0115	71,9

Photomultiplier tube replacement

After investigation of the SiPM characteristics the utilization in spectroscopic applications was tested. Typical and traditional way of sensing the light is with a photomultiplier tube. The SiPM has the ambition to replace it. However, the SiPM is advantageous from many points of view (size, bias), only comparison of spectra can show if it is really an adequate substitute. A measurement of a gamma spectrum was performed. To avoid influence of other parts of the system, such as a scintillator, the only change in the setup is the optical sensor. Sodium iodide doped by thallium (NaI:Tl) is understood as an etalon. It has the high light yield and the proper emission spectrum. Radioactive isotope of cesium (Cs-137) emitting photons with energy 662 keV is commonly used for calibration purposes. This combination guarantees the very reliable test. The only care has to be given to the proper size of the scintillator because photoelectric absorption is needed. The employed cylindrical scintillator was 1 inch high and 1 inch in the diameter that makes it large enough. The photomultiplier tube R1924A of size 1 inch in the diameter produced by Hamamatsu was biased by 900 V. The silicon photomultiplier FC60035 of size 6×6 mm^2 made by SensL was biased by 38 V from a laboratory source with 1.5 MΩ filter. Each measurement took 5 minutes. The radiation source was placed 2 cm far from the scintillator.

Spectra shown in Figure 31 prove shape similarity. At a closer look, the noise level and the resolution of the SiPM is worse. It should be noted that there was a small imperfection. The sensitive area of the SiPM is smaller so the amount of impacting light is lower in comparison to the PMT. Estimation based on the photoelectron spectrum indicates that a photopeak is generated by only 65 photoelectrons.

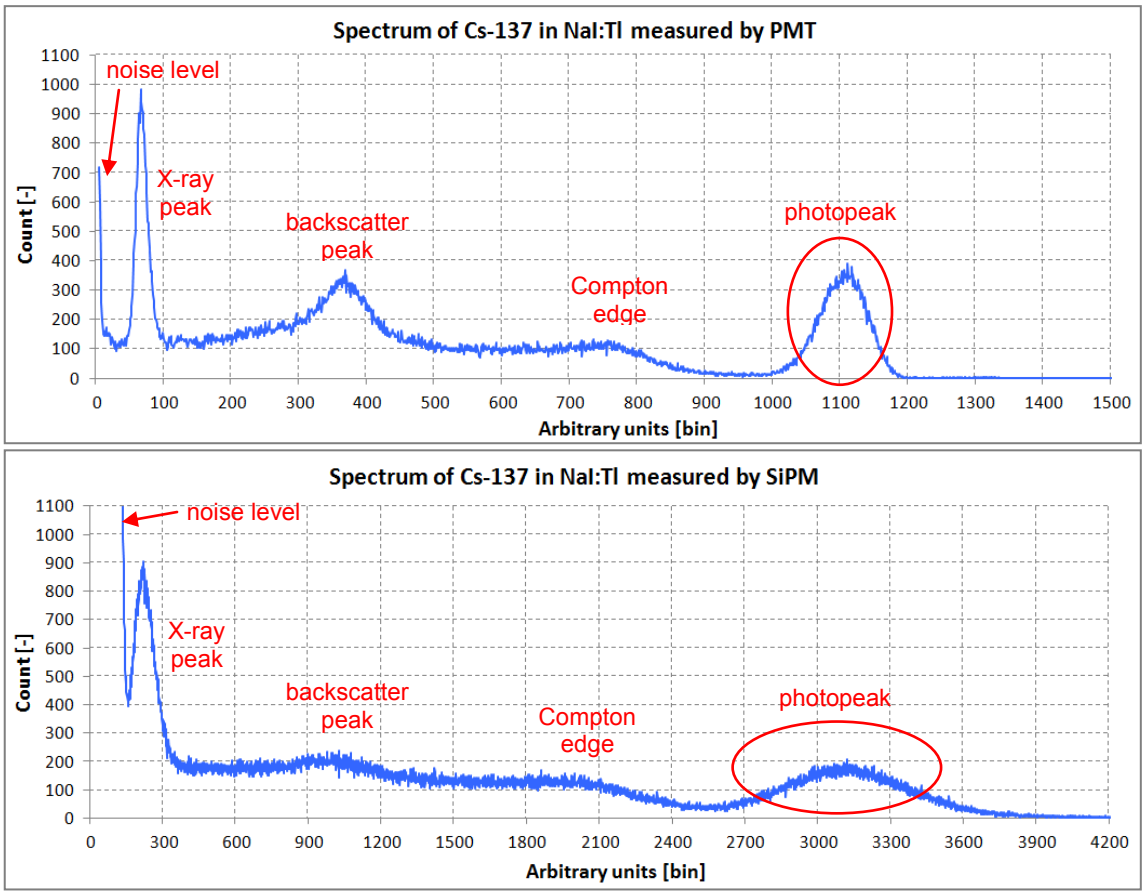

Figure 31: Spectra of Cs-137 in a 1 inch NaI:Tl scintillator measured by two different optical sensors – the photomultiplier tube (top) and the silicon photomultiplier (bottom). The shape corresponds sufficiently although the resolution of the SiPM spectrum is worse (20% against 7% with PMT) and the noise level is higher.

Silicon photomultipliers comply with expectations arose from the thesis project requirements. It is a suitable way how to acquire light from the scintillation detector. SiPMs are small but tileable to cover large areas, have enough gain and fits by spectral characteristics to the chosen scintillator. Type ArraySB-4 made by SensL is used in the thesis project.

7. Analog front-end for SiPM

Granularity of any radiation detector is always beneficial in comparison to a single segment. It allows to study distribution of charge or light in the detector. This information can be used in further investigation. The reason for the lack of high granularity detectors is the complexity of electronic circuits needed for readout and sophisticated data processing. Both needs increase the price of the development of the device.

The thesis project involves the granularity to provide additional information about the detection position and the incoming direction. The scintillator converting neutrons to recoiled protons is covered by 16 elements of the SiPM array. Although the count is not so high the discrete solution (in terms of individual components) is not ideal.

Preliminary version of the SiPM readout system based on discrete components was presented by the author [RI1], [RF4]. The final application is more demanding and another way of the SiPM signal readout had to be searched. The acceptable way is an integrated circuit designed for this purpose.

7.1. SiPM readout ASICs

Application specific integrated circuits (ASIC) are in domain of large experiments or collaborations. The reasons are as follows:

- Experiments difference – Each project/experiment is different and optimization can be impossible. Different demands on detection material, energy range, processing and many others results in a need of special ASIC.
- No universal solution – It is impossible to create somehow universal chip which could be adjusted externally like, for instance, operational amplifier. The main functionality is hard-wired in the ASIC and can't be changed.
- Costly development – Any change which has to be done in silicon influences other design layers. It results in new masks and the production run has to be repeated.
- Narrow market – There is a limited number of customers and sold goods. The fixed costs can't be so much dissolved in the sold quantity.
- Custom-made interface – ASICs need special hardware reflecting their functionality. It has to be also tailored and is often project specific.

Same as silicon photomultipliers become very popular because of their assets, new readout ASICs begin to appear. Unprecedented interest also proves the fact that special program is devoted to the readout chips at various conferences. The ASICs start to be commercialized and are available to wider group of scientists. A brief summary of available ASICs is in Table 4.

Table 4: A brief summary of parameters of ASICs designed for SiPMs [40]. Not only number of channels but also the output signal type (analog/digital), the input range, features etc. have to be taken into account.

Chip name	group	year	Technology	channels	Application
FLC_SiPM	OMEGA	2004	BiCMOS 0.8µm	18	ILC HCAL
NINO	CERN	2004	CMOS 0.25µm	8	ALICE TOF
MAROC2	OMEGA	2006	SiGe 0.35µm	64	ATLAS lumi
SPIROC	OMEGA	2007	SiGe 0.35µm	36	ILC HCAL
PETA	Heidelberg	2008	CMOS 0.18µm	40	PET
RAPSODI	Krakow	2008	CMOS 0.35µm	2	Snooper
BASIC	Bari	2009	CMOS 0.35µm	32	PET
SPIDER	Ideas	2009	CMOS 0.35µm	64	Spider rich

Cooperation between the IEAP and the Norwegian company IDEAS focused on the design of readout chips for radiation sensors was established[4]. They provide wide portfolio of chip types according to the projects they participated. It is even possible to have own chip tailored to the application. Application of SiPMs requires chip designed for higher leakage current and proper shaping, such as VATA64HDR16.

Because of the non-disclosure agreement, only the most important information essential for the thesis project can be mentioned in this text.

7.2. ASIC VATA64HDR16

The application-specific chip VATA64HDR16 [41] designed by IDEAS company in 0.35 µm technology is optimized for the spectroscopic measurements with silicon photomultipliers. Except energy measurements, timing measurements (time-of-flight/TOF) are supported by internal time-to-analog converters (TAC). The chip is a self-triggering device providing a trigger output when signal above threshold is detected. Shaping periods are optimized for SiPMs – triggering fast branch 50 ns, spectroscopic slow branch 300 ns. Slight adjustment is possible. The ASIC is able to process both signal polarities but the positive charge is needed for the whole functionality. The main difference over the chips for silicon detectors is the input stage. Each channel has leakage current compensation up to 10 µA which prevents the input amplifier saturation caused by a DC coupling and a higher dark current (in comparison

[4] Fruitful collaboration has led to a joint project AD-BANG (http://ad-bang.utef.cvut.cz/en/about/) that has successfully passed during the author's PhD study [NO1]. Author was responsible for the design of the electronic readout system for strip detectors based on VATA GP7/8.1 [NF1]. Another chip IDE3465 (and its non-public predecessor IDE3464) was tested by the author.

to radiation silicon detectors). Channel-to-channels matching of SiPMs is possible due to input DACs which change the bias for the particular channel. An adjustment of the gain is done in the chip so a common bias source for all SiPM segments can be used.

The chip is provided in a form of a naked die (unencapsulated). The total size is 9.8×6.5 mm^2. It has 64 input pads, 20 power supply pins and 60 configuration and readout pads occupying 3 sides of the chip (see Figure 32).

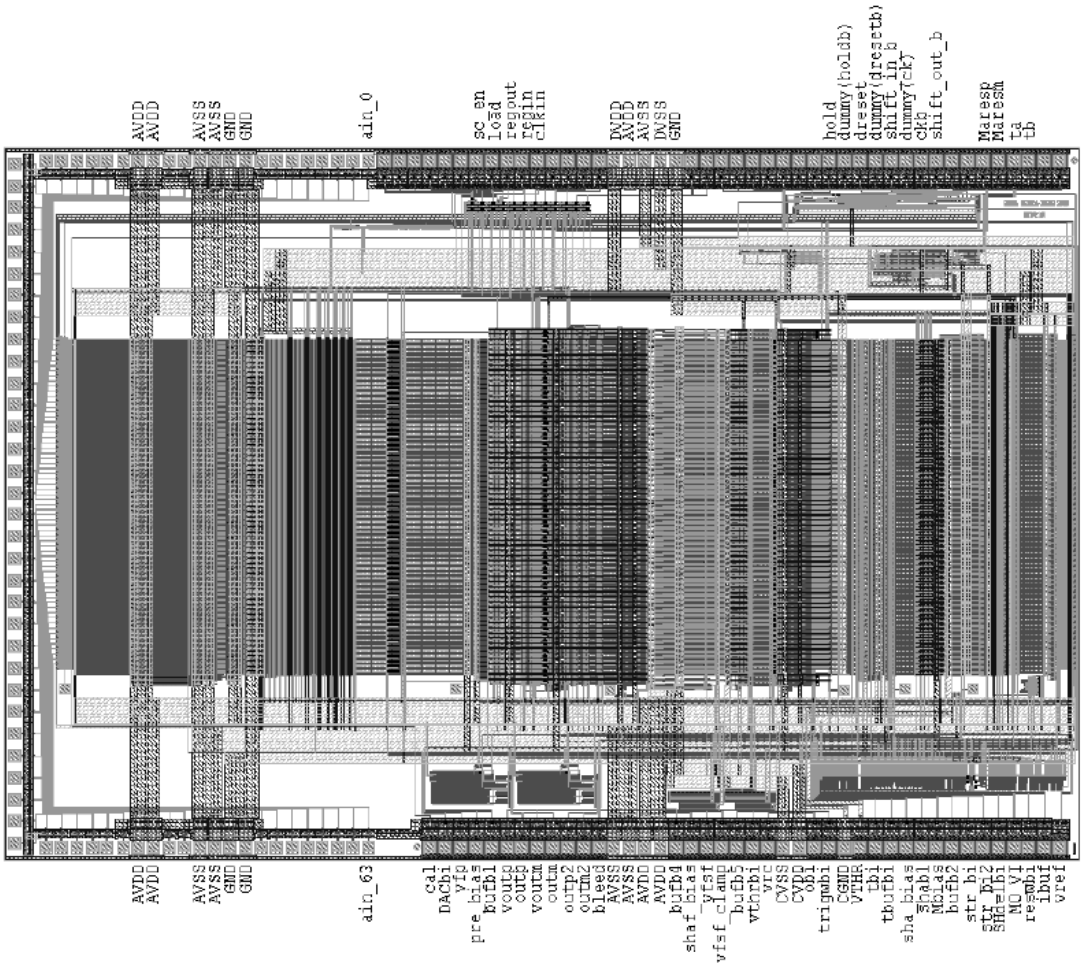

Figure 32: An arrangement of VATA64HDR16 pads is shown. Input pads are situated at the left side of the chip. Configuration and readout pads are at the right side of a horseshoe [41].

Internal structure

An internal structure of the chip is show in Figure 33. A front-end part covers the main functionality of the chip – amplification, shaping, trigger generation and storage of the sampled value. A further description can be found in the next chapter. A calibration part allows to test each channel individually. A shift register sets the switches of the calibration matrix. The particular channel is then connecter to the external calibration signal. Only one channel can be connected at a time. A readout circuitry is located in the back-end part. Outputs of all channels (energy information) are connected to a 64 channel wide multiplex. Another multiplex of the same width is used for the TAC output (timing information). Multiplexer outputs go out of the chip through differential buffers. These two multiplexers are controlled together through readout signals. Switching is made sequentially thus channel-by-channel information can be obtained.

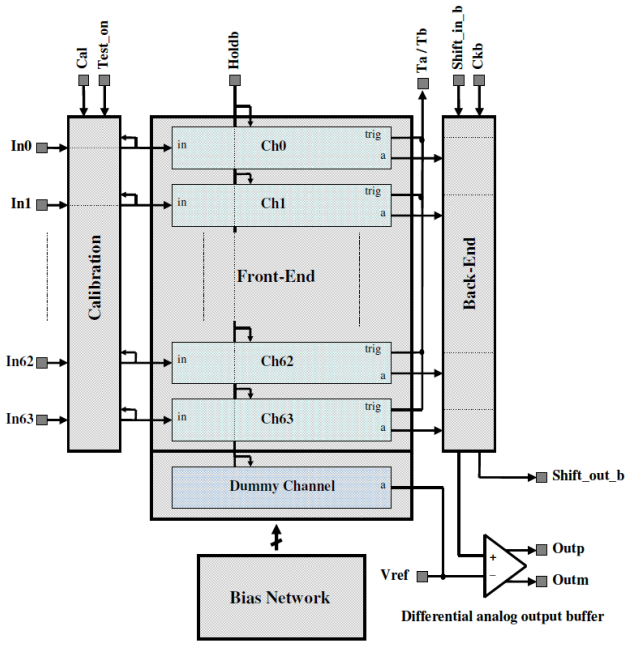

Figure 33: The diagram of a VATA64HDR16 structure is depicted. A front-end part incorporates 64 analog paths for signal processing. A calibration matrix enables external charge to be fed in the chosen channel. A back-end circuitry handles signal readout through an output buffer [41].

Front-end functionality

The core functionality of the ASIC is defined by the front-end part. Each channel has its own signal path. It starts with the charge sensitive amplifier with the adjustable bias level. The output of the first stage is branched into two paths. The fast shaper provides a sharp signal which is compared with the external threshold. The output of the discriminator is led out from the chip and used for a timing measurement in the TAC. The slow shaper makes a low noise pulse for an energy measurement. The peak hold circuit or the raw output can be used. A level of the signal can be stored in the sample-hold circuit for the sequential readout. A block diagram of the front-end is depicted in Figure 34.

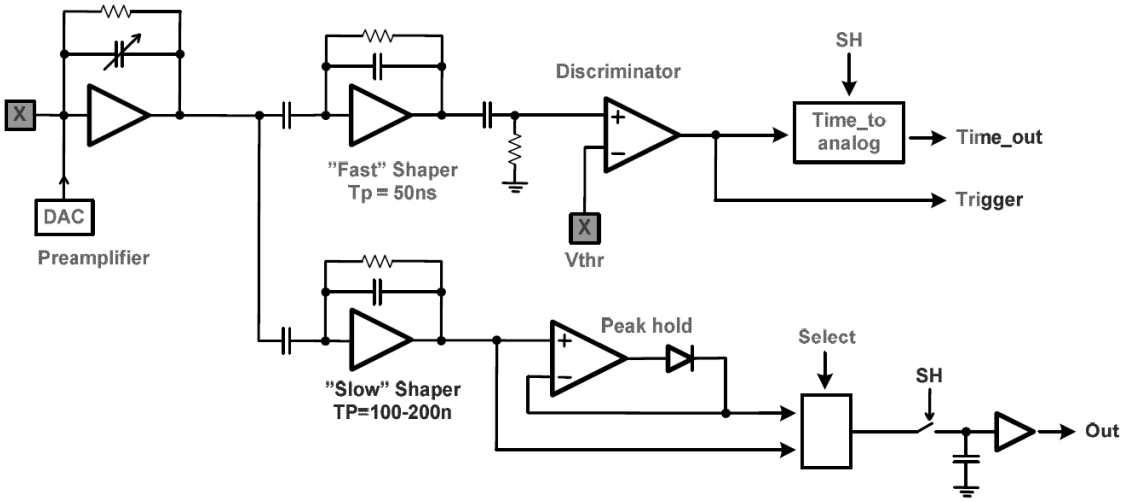

Figure 34: A block diagram of the front-end part of the VATA64HDR16 shows the main functionality of the chip [41].

ASIC configuration

The chip setting is performed by using a shift register. There is 873 bits in the shift register influencing chip behavior. It is possible to slightly change a gain or a shaping period of amplifiers. Noisy channels can be disabled. The threshold level and the input bias can be trimmed for every channel.

The content of the register is volatile. Configuration data has to be loaded after a power-up same as when change of the settings is desired. There is no storage memory in the chip so the superior system is responsible for that. Configuration mismatch caused by single event effects has to be solved by reconfiguration.

Readout sequence

The data readout of the chip is managed by an external logic through several signals. Let's suppose the chip is after reset and ready for further operations. When some event is detected by any channel, a trigger signal is generated and sent out of the chip. After the shaping period, the actual signal level at every channel should be stored in the sample-hold circuit and preserved for the whole readout period. The first bit (log. 1) clocked in the chip causes switching the readout multiplex to the first channel and the output value is set. Next bits (log. 0) clocked in the shift register make the output to update to proper value. The sequence can be completed or canceled anytime. The reset of the chip should be made to prepare it for a next event. A timing diagram of the readout sequence is in Figure 35.

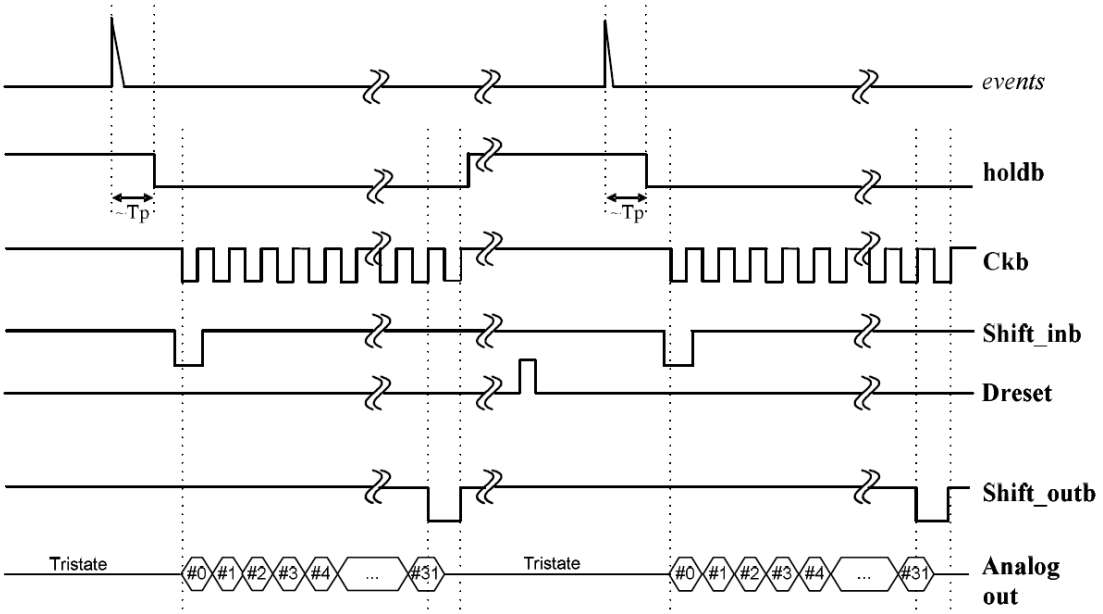

Figure 35: A readout sequence of VATA64HDR16 is depicted. An external logic is activated by a trigger signal (not shown). Channels are sampled after shaping period and preserved for the whole readout sequence. Clocking the bits through the shift register updates the analog output of the chip. Value of the output corresponds to the value sampled by the particular channel [41].

Power supply & signal levels

VATA64HDR16 has separated analog and digital power supplies for reduction of the noise. The supplies are symmetrical in both cases (+/- 2.5 V). There is no special power supply for interfacing signals. Two groups of signals are used by the chip – differential and single ended. No standards are followed and the specification is not too well defined. Single ended signals should be -2.5 V (logic 0) and +2.5 V (logic 1). Differential signals work as a comparison of positive and negative branch. Common mode voltage is not defined.

8. Spectroscopic ASIC readout system

The readout system for the spectroscopic ASIC is based on the own universal platform. It provides ability to replace the same type or even employ different types of spectroscopic chips. There are two reasons for this approach. At first, VATA chips produced by IDEAS are provided as untested. The production yield is quite high but not 100%. It can happen that the particular chip is faulty or the functionality is not completely correct. It is very confusing to accidently choose a faulty chip at the beginning of the development (happened to the author). It is much safer that the verification of the design can be made for more chips. The second reason is usability of the readout system for different chips, i.e. in different projects, that further increases the value of the effort put into the project. The platform supports chips which were met during the work: VATA GP7 [NF5], VATA GP8.1 [NF1], VATA 464, IDE3465 and of course VATA64HDR16 [RF1].

The design of the readout system is more complex to cover a dissimilarity of ASICs. There are two parts, the interface board and the chip dongle.

8.1. Interface board

The purpose of the interface board is to provide the common functionality. A block diagram is shown in Figure 36. The chip dongle is connected through Mini edge card connector MEC6-RA from Samtec. All the signals including a power supply lead through this connector. The structure of signals is selected to cover wide range of the supported ASICs. The wiring diagram is shown in Appendix B.

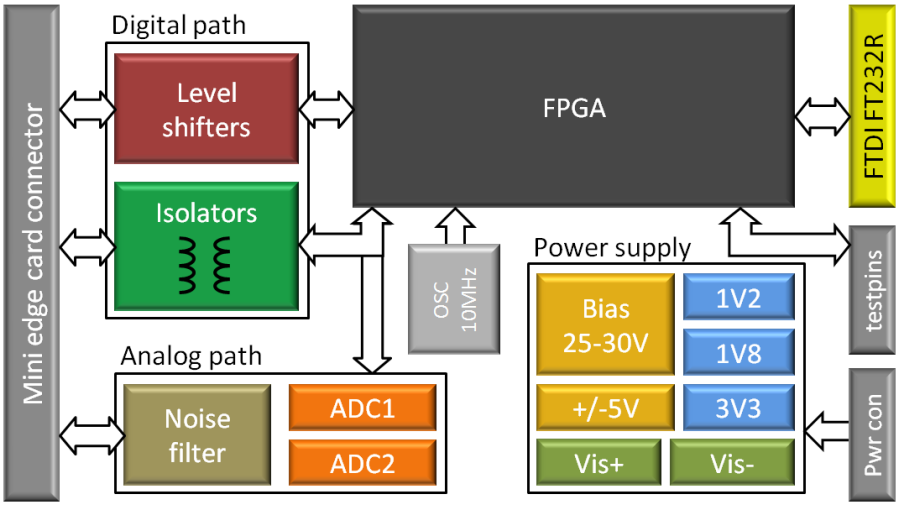

Figure 36: A block diagram of the interface board is depicted. Main connections are emphasized.

Analog path

The main functionality of the spectroscopic ASIC is to provide information about the deposited energy. There is no ADC implemented on the chip. An external converter has to be provided. Two independent ADCs LTC1402 are assembled. Resolution of

12 bits is sufficient for the presumed operation. A conversion rate up to 2.2 MSPS is high enough not to limit event throughput. A noise filter is added in front of the converter. A single-ended positive signal with range up to 2 V is supported.

Digital path

Digital signals are used to control the ASIC operation. Some signals are spared for auxiliary circuits needed for the ASIC, such as a DAC. Because the signals of the ASIC are not referenced to ground, isolators ADuM764x are assembled. This approach allows to interface various chips with different power supply. The FPGA side of the isolator has fixed voltage, same as the supply voltage of the particular FPGA bank. The ASIC side is supplied according to the chip requirements. The isolator technology is used because it can transfer even steady signals. Pulse character signals, such as trigger or clocking signals, use level shifters with AC coupling.

Power supply

The interface board is powered from an external source. The symmetric voltage of at least +/- 7 V is needed. Higher values increases heat generation with no positive effect to regulation. Linear stabilizers are used to decrease the noise. Sensitive low power ADCs are supplied through the filters. Positive and negative 5 V stabilizers are used for the chip dongle supply. Adjustable voltage for isolators can be set according to the particular chip. A negative bias voltage for the SiPM array is generated by LT3462 [RF2]. The voltage value is manually adjustable from -25 V to -30 V. This range allows setting the appropriate operation point.

Communication interface

The Universal serial bus (USB) was chosen as a communication interface. It is the well-managed technology available on all nowadays computers. A bridge FT232R made by FTDI is assembled. It encapsulates the robust USB protocol into a simple serial line (UART). The data transfer rate is up to 3 Mbaud.

A rough estimation, considering the structure of the communication protocol, gives the transferred rate up to 900 events/s. This is definitely the bottleneck for stand-alone operation of supported ASICs which can provide about ten times higher event rate. However, considering the coincidence operation with Timepix detector, which records at most similar frame count (depending on the generation of FITPix interface, usage of hardware compression etc.), makes this rate sufficient for the prototype.

FPGA

The complete logic functionality is implemented in a field programmable gate array (FPGA). The amount of needed logic and the data throughput is limited mainly by the spectroscopic ASIC. A Spartan 3AN type FPGA XC3S50AN made by Xilinx is utilized [42]. Pins are divided in four banks. Two of them are supplied by 3.3 V. They are used for the communication with the USB bridge, ADCs and control the ASIC lines through digital isolators. Another two banks are supplied by 1.8 V and are used for interfacing the ASIC through level shifters. Several I/O standards are used, such as CMOS, LVDS and HSTL.

The FPGA has volatile structure as usually. A small advantage of this type is an integrated flash memory to store the configuration of the firmware. A separate chapter is dedicated to the description of the firmware.

8.2. Chip dongle

The chip dongle is tailored for the specific chip and respect its needs. The most important is a power supply (voltage and power requirements). Supply filters are also adapted. There is a current source needed for biasing of the internal structure of the chip. A nominal value indicated in the documentation has to be kept. Significant deviation from the value can cause a malfunction of the chip operation. An external DAC assembled on the chip dongle allows setting of a threshold voltage or possibly other voltages which influence the chip behavior (a preamplifier stage gain, a shaping period). Analog output drivers on the chip have limited strength. Operational amplifiers are assembled near the chip to minimize signal distortion because of a capacitive load. Low impedance signals are then led to the interface board. Depending on the particular chip, level shifters are on the board. A block diagram of the chip dongle is shown in Figure 37.

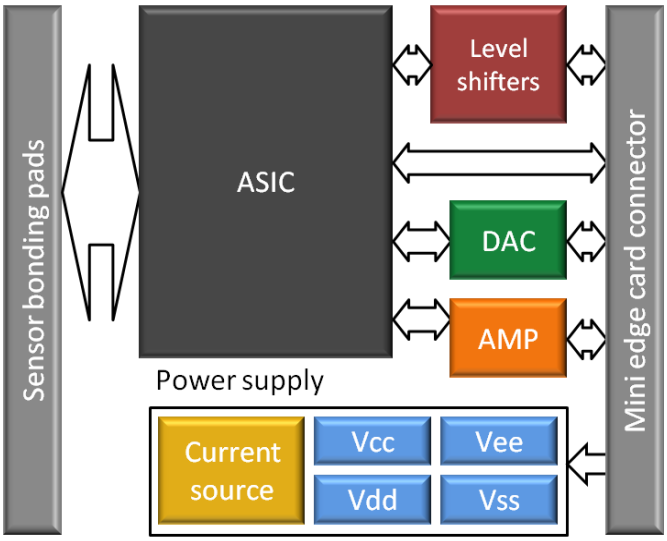

Figure 37: A block diagram of the universal chip dongle is depicted. Components and wirings are adapted according to the type of the ASIC.

VATA64HDR16 dongle

Linear stabilizers providing +2.5 V and -2.5 V are assembled on the dongle. An available current limit is 150 mA in both positive and negative branches. A current source made of LM334 is adjustable by a trimmer resistor. The prescribed value for VATA64HDR16 is 700 µA. Trigger setting is possible by 4-channel 12-bit DAC AD5724. The rest of channels can be used to override internally generated voltages. Two operational amplifiers MC33077 provide gain for analog outputs of the ASIC. Transistor level shifters based on PMDT670 are used for digital signals controlling the readout operation. Sensor pads of the ASIC are wire-bonded to PCB traces. Sensors are then connected to PCB, not to the chip directly. The connection capacity is slightly higher but the reworkability of wire-bonding is almost unlimited.

9. Firmware

The operation of the Multi-coincidence system is defined by the firmware implemented in the FPGA assembled on the Interface board. For the purpose of the thesis project, the firmware needed to be tailored. The main functionality is based on the universal solution for different spectroscopic VATA chips. The enhancement was necessary for a coincidence management which makes the part with the scintillation detector a master of all the system.

The firmware is created in accordance with the principles of the hierarchic design. Each functional block can be optimized and simulated alone. Verified blocks are then connected together. Reliability is higher and simulation simpler than designing from scratch. A block diagram of the firmware structure is shown in Figure 38.

Development of the firmware was made in the development environment ISE Design Suite 14.7 provided by Xilinx. The code is written in a VHDL.

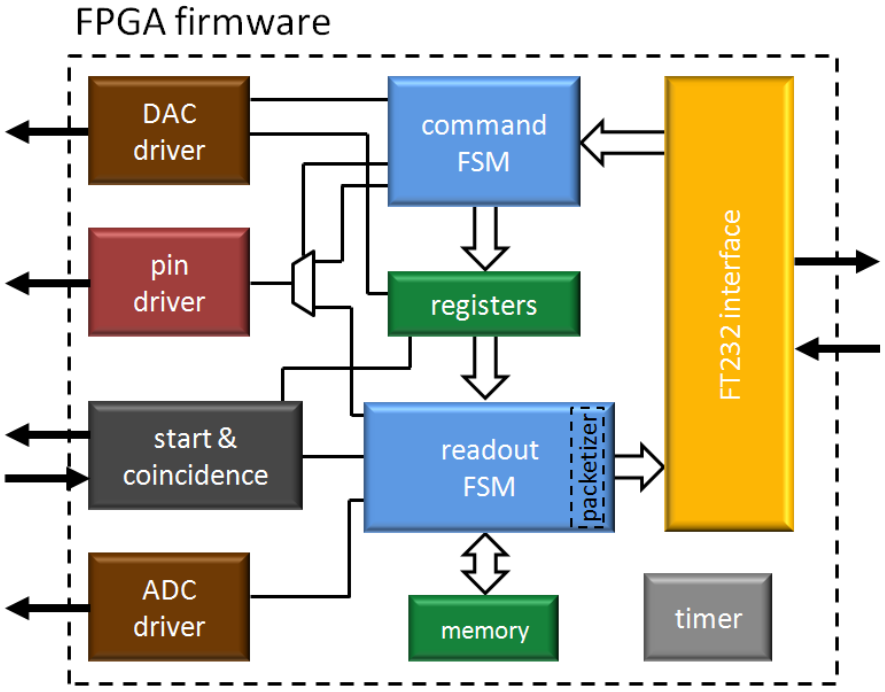

Figure 38: A block diagram of the firmware structure. Blocks correspond to the components in the hierarchical design.

9.1. Core state machines

The core of the design consists of command and readout finite state machines (FSMs). Setting of the device is separated from the data path. The readout sequence is independent on any acknowledgement from a computer. It increases the transfer rate when data blocks are small (as is in this case). The reliability of the data transfer is ensured by the checksum. Due to the anticipated operation of the system, commands are

processed preferentially before data sending. This allows the superior software to influence the data flow, such as start or stop the acquisition.

Command FSM

The command FSM block parses command packets from the control software. Each command packet has two bytes – a header and a command value. The header defines the storage register or the operation to be performed. In principle, there are two groups of commands (see Table 5). The first group associates commands for normal operation. The second group is rather redundant and serves as a debugging interface for the chip verification.

Registers are volatile. User software is responsible for loading proper values before the measurement. This applies to both command recipients FPGA and ASIC.

Table 5: A table shows the commands used by the system. The left side commands are used for normal operation. The right side commands are implemented for debugging purposes.

Command	Code (dec)	Command	Code (dec)
DAC value (23:16) + start	0x0A	Clkin (log. 0/log. 1)	0x2B / 0x30
DAC value (15:8)	0x0B	Regin (log. 0/log. 1)	0x35 / 0x3A
DAC value (7:0)	0x0C	Shift in (log. 0/log. 1)	0x3F / 0x44
Config match set	0x64	Gck (log. 0/log. 1)	0x49 / 0x4E
Enable readout (log. 0/log. 1)	0x85 / 0x8A	Res (log. 0/log. 1)	0x53 / 0x58
Readmode serial	0x8F	Samp-hold (log. 0/log. 1)	0x67 / 0x6C
Readmode single	0x94	Load (log. 0/log. 1)	0xAD / 0xB2
Read count (15:8)	0x96	Master res (log. 0/log. 1)	0xB7 / 0xBC
Read count (7:0)	0x97		
Shape delay	0xA2		
Pedestal run (log. 0/log. 1)	0xCB / 0xD0		
Coincidence mask	0xD5		
Coincidence timeout	0xD6		

Readout FSM

The readout sequence synchronizes operation of the ASIC with a signal conversion of its analog output. Timing conditions depend on a type of the spectroscopic chip, an ADC and desired features. Beginning of the sequence is related to the trigger signal regardless of whether it is external or internal.

Each event is processed according to the values stored in registers, such as readout mode or number of channels to read. Transitions between states and conditions which need to be fulfilled are represented by a flowchart shown in Figure 39. Briefly, it is possible to sum up the universal event handling to the following points:

- Waiting on a trigger
- Waiting for shaping time expiration
- An analog signal conversion and storage
- Data transfer to a PC
- Reset

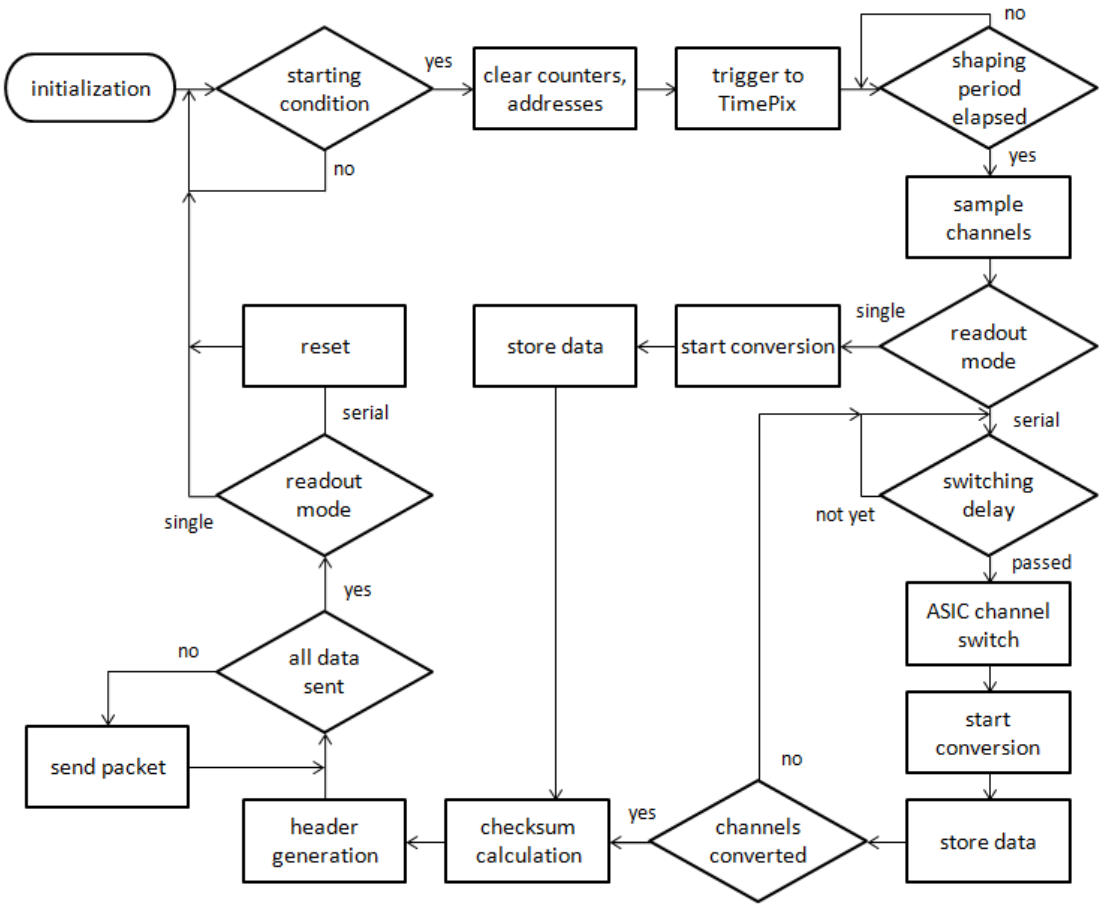

Figure 39: A flowchart of the readout sequence is shown. When the starting condition is met, necessary steps are processed to read, convert a transfer data to a computer.

There are two readout modes implemented for VATA64HDR16. The simple one is a single mode. In this case, the channel is chosen before the acquisition is started and is kept for the whole measurement. Meanwhile, there is no switching of ASIC channels. This mode is usable when only one channel is interesting for the measurement, for instance when using large sensor volumes. It is not typical usage of the ASIC and because of the nature of the thesis project it is not usually used.

The second mode is the ordinary way of the readout. Any channel detecting an event invokes a trigger. All channels are then sampled after the shaping period. The peak values are stored in sample capacitors available for each channel. When the channel multiplex is switched, the voltage value stored in the sample capacitor is brought to the output. All channels can be read or, if needed and supported by the arrangement of the detectors, only partial sequence can be performed which would make the procedure less time consuming. Both variants are supported by the firmware. Number of channels to be read can be set by the dedicated command. Unfortunately, skipping channels is not possible.

The analog output of the ASIC is converted by the ADC. Digital data are stored in the internal memory in the FPGA. There is 54 kbits of block memory available [42]. It is much more than needed for processing one event. There is only one block (18 kbits) utilized by the firmware. It is configured as a single port RAM. When desired amount of channels is stored in memory, the data checksum is calculated and the result is stored to

the data header together with a channel count. Prepared data are then sent to a computer. A new event can only be processed after the memory is unloaded.

Data are organized in packets (see Table 6). Each packet is 5 bytes (40 bits) long. A header packet situated at the beginning of the transfer contains identification bytes, number of data packets and checksum. Data packet contains one toggle bit acting as a data loss protection, 11-bit channel address and two 14-bit ADC values. This structure is suitable for all ASICs made by IDEAS used so far, even for sparse mode when only hit channels are read. There is no trailing packet. Transferring one event needs just one header packet followed by defined number of data packets. The correctness of the transfer can be checked by the identification of header bytes, a number of data packets and their toggle bits. Two consecutive successfully parsed events prove the correctness of the first one.

Table 6: A table shows the structure of transfer packets used for sending data from the hardware to the computer. There is only one header packet followed by several data packets per each event.

Packet type	Header			
bit	39:24		23:8	7:0
contents	0xAA53		data packet count	data checksum
Packet type	Data			
bit	39	38:28	27:14	13:0
contents	toggle bit	channel address	ADC 2	ADC 1

9.2. Peripherals

The core state machines are surrounded by peripheral components responsible for partial tasks. Due to the design of the structure, any change is very easy to make by modification or addition of a new peripheral.

FT232 interface

A component FT232 interface processes downstream/upstream data flow from/to the FTDI bridge. An incoming UART data stream is converted to an 8-bit parallel bus with handshaking. This applies vice versa for the inverse direction. There is no buffering provided by the component. In case it is needed, external buffering has to be added.

The component is designed as the universal one for different UART speeds. A frequency and a baud rate can be set by generic parameters in a VHDL code and other timing constants are calculated accordingly.

ADC driver

Analog signals are converted by the ADC. It is controlled by the dedicated VHDL component. It incorporates a state machine which begins the operation after the Start signal received. The sequence of signals, timing and conditions correspond to the SPI communication framework defined in the datasheet provided by the ADC manufacturer. During the operation the Busy signal is active. Readout FSM monitors it and takes the parallelized data when it expires.

Available Nap and Sleep modes of the ADC are not used because it doesn't correspond to the project needs.

DAC driver

The output values of the DAC can be set through SPI interface. There is 24-bit command needed to fill the internal shift register of the DAC. The driver component controls the signal lines which are set according to the value stored in the dedicated registers. A configuration process starts upon a request (see Table 5). Acceptance of the next command is postponed during the DAC configuration.

Pin driver

A pin driver sets or clears the signals leading from the FPGA. The most of them is connected to ASIC, several are used for debugging. There are two sources of a stimulus for ASIC pins. During the readout sequence the FSM specifies pin states and timing relation. This mode needs to be optimized in hardware. Proper knowledge about the chip is essential. A command mode is implemented as the second option for pin setting (see Table 5). Getting familiar with the chip and debugging operations are the main purposes of this option. There is high variability of the software control which can't be reached by the hardware. The disadvantage is slower timing (6.6 μs per the change of the pin). That is the reason why this mode is not usable for the normal readout operation. But the slow configuration of the ASIC uses this feature as advantage.

Start & coincidence

This part of the firmware is responsible for system synchronization and is tailor for the thesis project. As it is implemented in the newly developed readout system, it takes into account the existing interface of the FITPix device. The operation is not strictly intended for the coincidence mode.

The newly developed readout system acts as a master. The neutron collision generates light in the scintillator. It is collected by the SiPM whose signal induces a trigger signal. It starts the internal readout sequence as mentioned previously and furthermore, signal pulse is sent to the FITPix interface. According to FITPix settings, the pixel detector acquisition can be started. A busy signal is valid during the pixel acquisition including the data transfer. The pixel detector readout operation is more time consuming than the SiPM readout. The new trigger from the SiPM can be inhibited until the busy signal is cleared. This mode provides frame synchronization because acquisitions are started at the same time. Moreover, time delay of fixed length can override the busy signal.

FITPix and the SiPM readout system have similar setting. Following combination of acquisition modes stated in Table 7 are available.

Event rate throughput depends on the coincidence mode and is highly influenced by the hardware. However, throughput is not crucial for the thesis project. Increasing the readout speed of the system parts, if possible, will increase the total event count. The maximum number of events is limited by the slowest device.

Table 7: Combinations of the trigger modes of the new SiPM readout system and the FITPix interface define the coincidence operation.

Trigger condition		Repetition condition	Comment
SiPM	FITPix		
random	X	meaningless	An unnatural mode of the SiPM readout. Acquisition starts asynchronously to the incomming particles.
X	software	meaningless	A natural mode of FITPix because it doesn't provide a self-trigger.
event	hardware	none	Coincidence events possible. Higher event rate causes asynchronous data to be acquired that decreases measurement efficiency.
event	hardware	FITPix busy	Coincidence events desired. No new event is processed until the previous one is completely finished.
event	hardware	time delay	Coincidence events desired. Time delay decreases the event rate but eliminates busy handshake mismatches.

9.3. Firmware occupancy & portability

The firmware implementation is not made on the most modern FPGA. Due to the length of the development, the used technology reflects the time when the design of the system began. But the space and speed requirements are fully fulfilled by the chosen FPGA. The synthesis and PAR report is shown in Table 8.

There are 23% of flip-flops, 41% look-up tables and 36% pins used by the design. It means the design occupies less than a half of the FPGA logic resources for the desired functionality. If needed, more logic could circuits can be implemented directly to the prototype.

The VHDL code is available for future use or for further integration, for instance with FITPix. It is a transferable description of the behavior independent on a platform or a development tool (except parts generated by the tool itself, such as memories).

Table 8: A project report of the synthesis and PAR of the thesis project VHDL code is shown. Below the half of available resources is consumed by the whole design.

source Project Status			
Project File:	dongle64hdr.xise	**Parser Errors:**	No Errors
Module Name:	source	**Implementation State:**	Programming File Generated
Target Device:	xc3s50an-4tqg144	**•Errors:**	
Product Version:	ISE 14.7	**•Warnings:**	
Design Goal:	Balanced	**•Routing Results:**	All Signals Completely Routed
Design Strategy:	Xilinx Default (unlocked)	**•Timing Constraints:**	All Constraints Met
Environment:	System Settings	**•Final Timing Score:**	0 (Timing Report)

Device Utilization Summary				[-]
Logic Utilization	**Used**	**Available**	**Utilization**	**Note(s)**
Number of Slice Flip Flops	325	1,408	23%	
Number of 4 input LUTs	581	1,408	41%	
Number of occupied Slices	422	704	59%	
Number of Slices containing only related logic	422	422	100%	
Number of Slices containing unrelated logic	0	422	0%	
Total Number of 4 input LUTs	652	1,408	46%	
Number used as logic	581			
Number used as a route-thru	71			
Number of bonded IOBs	39	108	36%	
Number of BUFGMUXs	1	24	4%	
Number of RAMB16BWEs	3	3	100%	
Average Fanout of Non-Clock Nets	3.37			

Performance Summary			[-]
Final Timing Score:	0 (Setup: 0, Hold: 0, Component Switching Limit: 0)	**Pinout Data:**	Pinout Report
Routing Results:	All Signals Completely Routed	**Clock Data:**	Clock Report
Timing Constraints:	All Constraints Met		

10. Prototype of the Multi-coincidence system

The design of the Multi-coincidence system introduced in this work led to the prototype allowing the verification of the concept. The aim is not to prepare final and highly optimized device. It is expected that future generations of the system will take into account the shortcomings that will be found during measurements with the prototype.

The development of the new SiPM readout system is the significant part of this thesis. It was divided into units which were assembled on separated boards (see Figure 40). The universal Interface board (see chapter 8.1) provides power supply and control logic implemented in the FPGA. The board size is 113 mm × 52 mm. An USB communication board (see chapter 0) with FT232R of size 60 mm × 35 mm is used. The ASIC dongle board (see chapter 8.2) is attached to the Interface board. One spectroscopic chip VATA64HDR16 is mounted. Detail of the chip dongle with the Interface board in the background is shown in Figure 41.

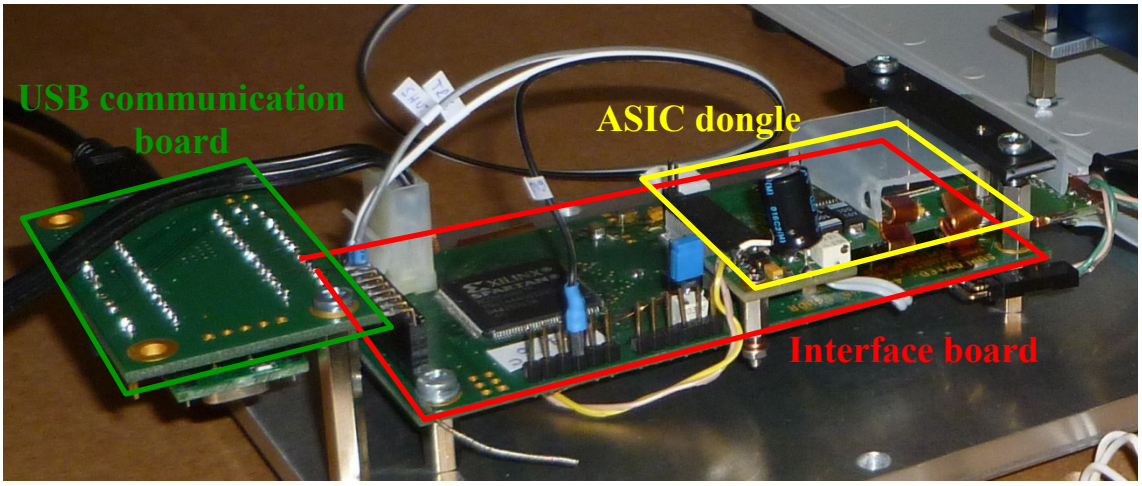

Figure 40: A prototype of the SiPM readout system is depicted. It consists of several separated boards.

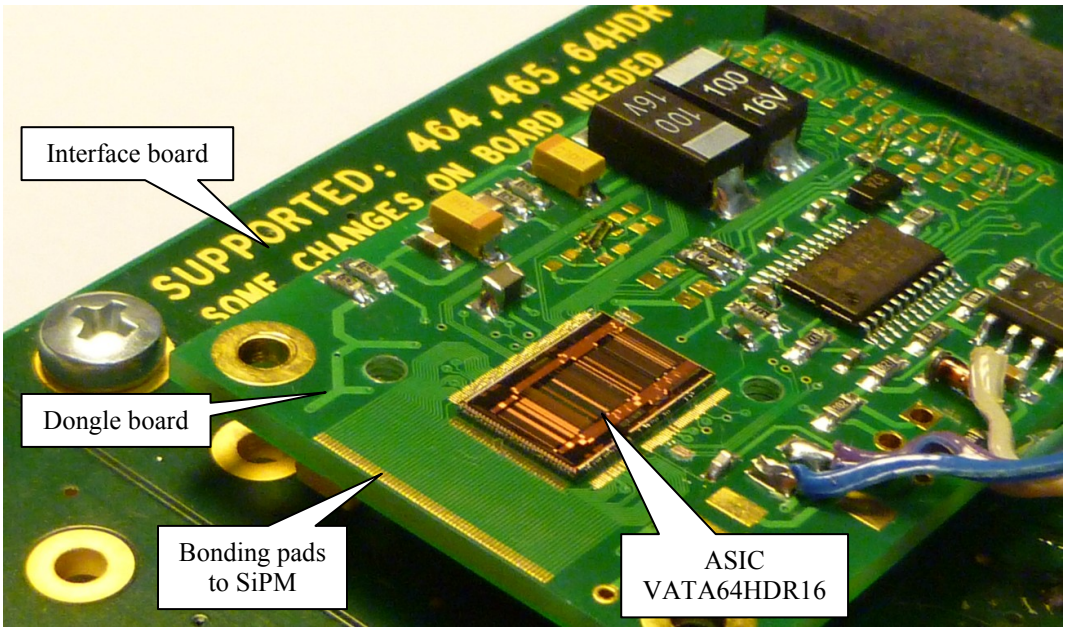

Figure 41: The picture shows the detail of the chip dongle board. ASIC pads are wire bonded to the PCB including input signal pads. The universal Interface board is in the background.

After the stand-alone tests of the SiPM readout system it has been attached to the pixel detector to create the Multi-coincidence system. Proper XY alignment of the sensitive volumes (the scintillator and the silicon pixel detector) is needed. The distance of the layers is not critical but should be in a reasonable range, i.e. in order of few millimeters, because it influences detection abilities of the system. The detail of the composition is shown in Figure 42.

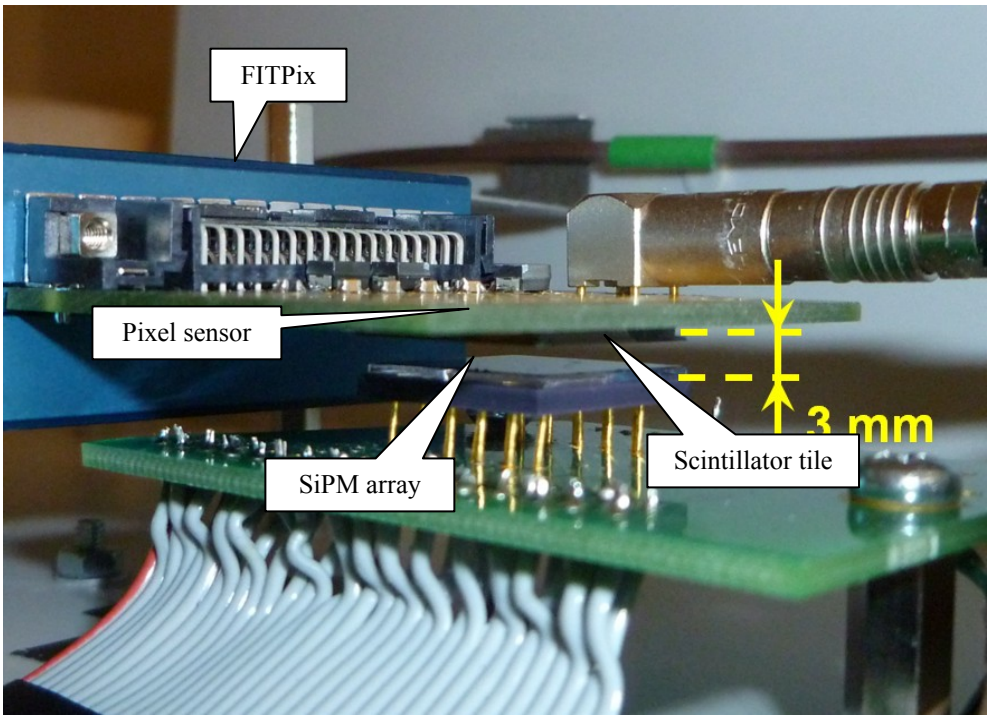

Figure 42: An alignment of the silicon pixel detector and the scintillation detector is depicted. It is desired to maximize the overlap of the sensitive volumes.

The light shielding of the scintillator is needed otherwise the sensor, i.e. the SiPM, is overwhelmed by photons of the ambient light. Although the silicon detectors are light sensitive too, Timepix is commonly covered by the aluminum layer which makes it fairly insensitive to the light of the common intensity. So the only light sensitive part is the scintillator with the attached SiPM array. It is possible to cover it by a tape or paint but it is inappropriate for testing and debugging. Furthermore, it is additional material which has to be penetrated by the recoiled proton which is very undesirable. So it was decided to cover all the detection volume including the FITPix interface.

The resulting form of the Multi-coincidence system prototype is shown in Figure 43. The sensitive volume is placed inside the plastic box which shields the ambient light. The FITPix interface is placed near the pixel detector so it has to be in the box too. The newly developed readout system for the SiPM array is mounted on mechanical support outside the box for possible debugging. Synchronization of both systems is ensured by cabling. Black bushings are used to eliminate photons entering the box. Overall dimensions of the system prototype are roughly 30 cm × 28 cm × 10 cm.

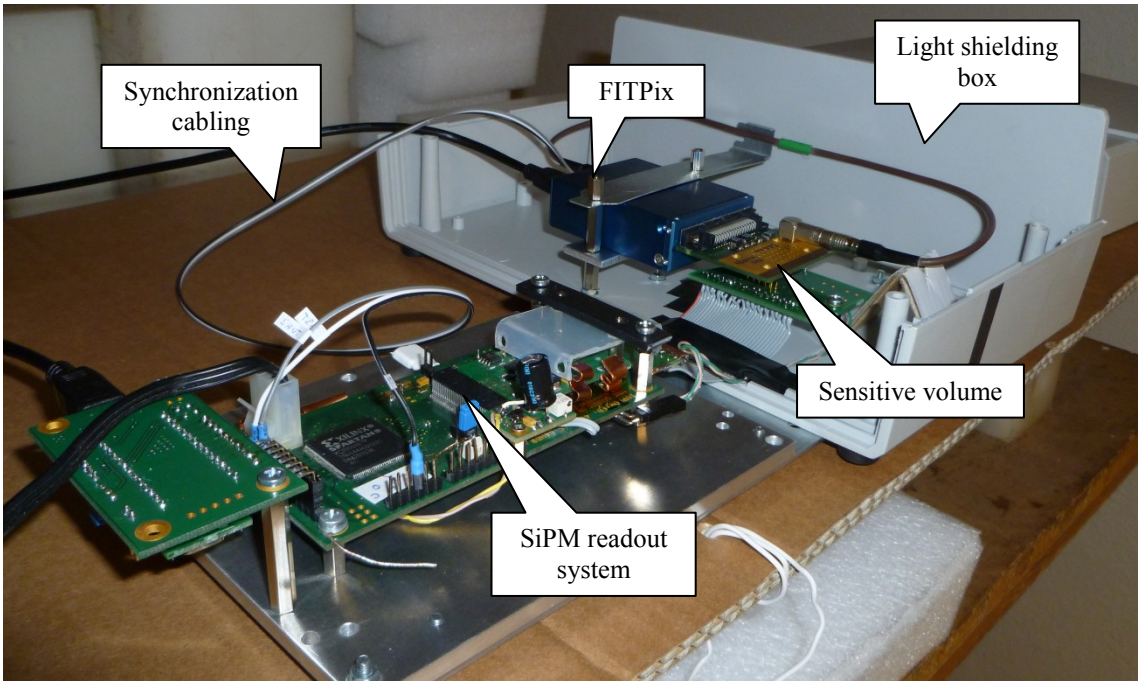

Figure 43: The prototype of the Multi-coincidence system is depicted. A light shielding covers the sensitive volume (the scintillator and the pixel detector) together with FITPix.

The prototype of the Multi-coincidence system shown in the Figure 43 was used for all measurements and verification of the final functionality. Results are described in the dedicated chapter.

11. Acquisition software & basic processing

Nowadays, the hardware design is not enough in its stand-alone form. The functionality needs to be supported by the software tool for data processing. Of course, ordinary operations like hardware setting, acquisition control, basic data visualization and storage need not to be even mentioned. The custom-made solution is necessary.

The development of the software tool is the part of the thesis project. The basic needs arise at the very beginning because of debugging and verification of the hardware. Subsequently, data visualization and graphical representation of the results are needed. The independent tool for data processing was prepared because of the two separated systems (for the pixel and the scintillation detector) which are operated with their own control applications.

11.1. Readout tool

The software for data readout communicates with the hardware, provides setting of the ASIC and FPGA registers, manages the acquisition and data handling, such as data packet recognition, visualization and storage.

The user PC is connected to the universal Interface board (see chapter 8.1) through USB. The integrated circuit FT232R is used as a bridge between USB and UART protocols. From the software point of view, data flows through D2XX driver library provided by the manufacturer as a DLL [43]. Different platforms are covered – Windows, Linux etc. The set of functions, which allows basic operations, is provided. The source code then implements complex handler of the communication.

The readout tool is prepared in C++ language as two-threaded application. The first one covers user GUI operations. The second one is responsible for processing of received packets and data evaluation. Only Windows platform is supported now.

GUI

A graphical interface allows the user to interact with the hardware device. It is based on forms which contain components for data displaying (labels, graphs) and commands entering (buttons).

The main GUI window is shown in Figure 44. At the beginning, the desired device has to be chosen from the list of devices. User is fully responsible for selection of the device with compatible firmware. Initialization procedures set the communication parameters and prepare form fields.

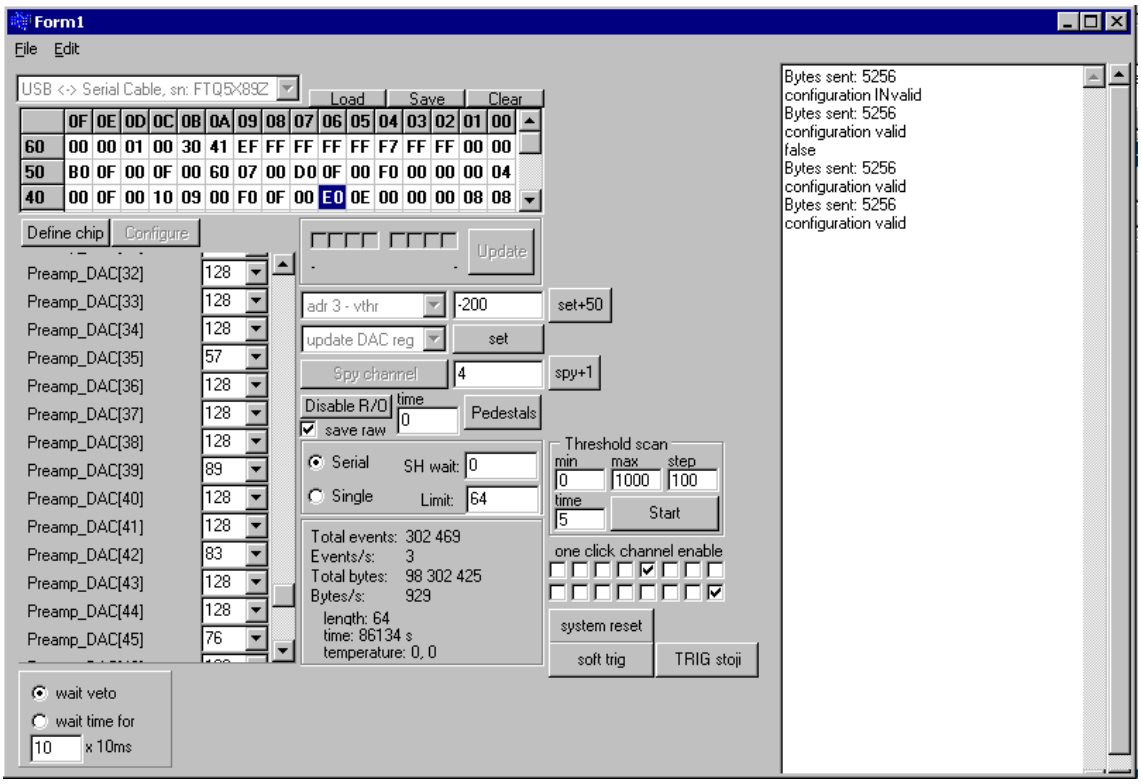

Figure 44: The main window of the acquisition software is depicted.

The main form was developed not to be dedicated for the specific ASIC. The list of configuration parameters for each chip is prepared according to its datasheet. A text file with the list is easy editable in any text editor. Format of the text file can be seen in Figure 45. The file is parsed in the software and objects are generated accordingly. Each object contains a name of the parameter, a position in the shift register (bit index), a number of bits occupied in the register (bit length), an order of bits and a text shown as a hint to help the user to understand the meaning of the parameter. For easier start, the configuration file is preselected for VATA64HDR16 directly in the code.

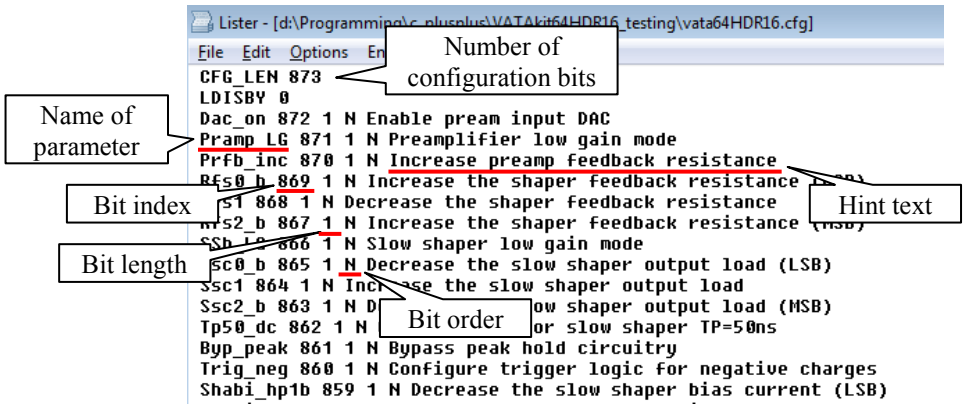

Figure 45: An example of the text file with ASIC configuration parameters is shown. A structure of the file allows to change the parameters for the particular ASIC.

The ASIC configuration values are displayed both in a spreadsheet and in interactive fields. A binary value can be changed by checkboxes. Any change in any element is mirrored to others. It is possible to load values from file, save them for future use or clear them (see Figure 46).

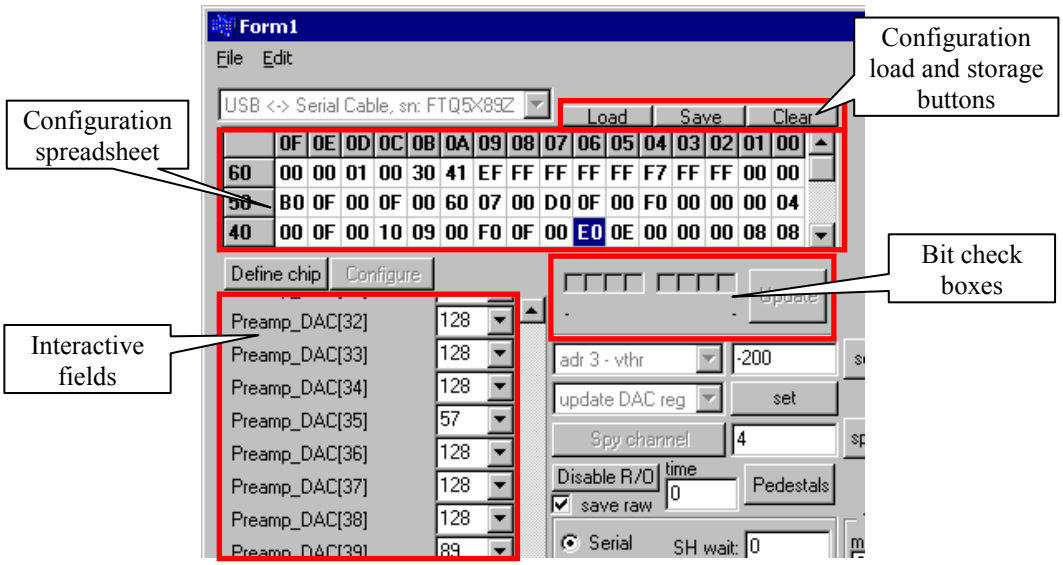

Figure 46: The ASIC configuration can be done in several ways. Any change is mirrored to all the field.

Other components influence a measurement mode and an acquisition itself (see Figure 47). DAC channels can be adjusted in all the available range. Text description is adapted according to the DAC channel function. Readout modes (serial and single) can be chosen together with a number of channels to be read. Both types of coincidence feedbacks are available and can be even switched off for the asynchronous operation. An overview of the ongoing acquisition is provided by the panel with measurement statistics. The acquisition time limit can be preset when systematic measurements are needed. The data storage requirement depends on the measurement. However, it is necessary for further processing of coincidence events.

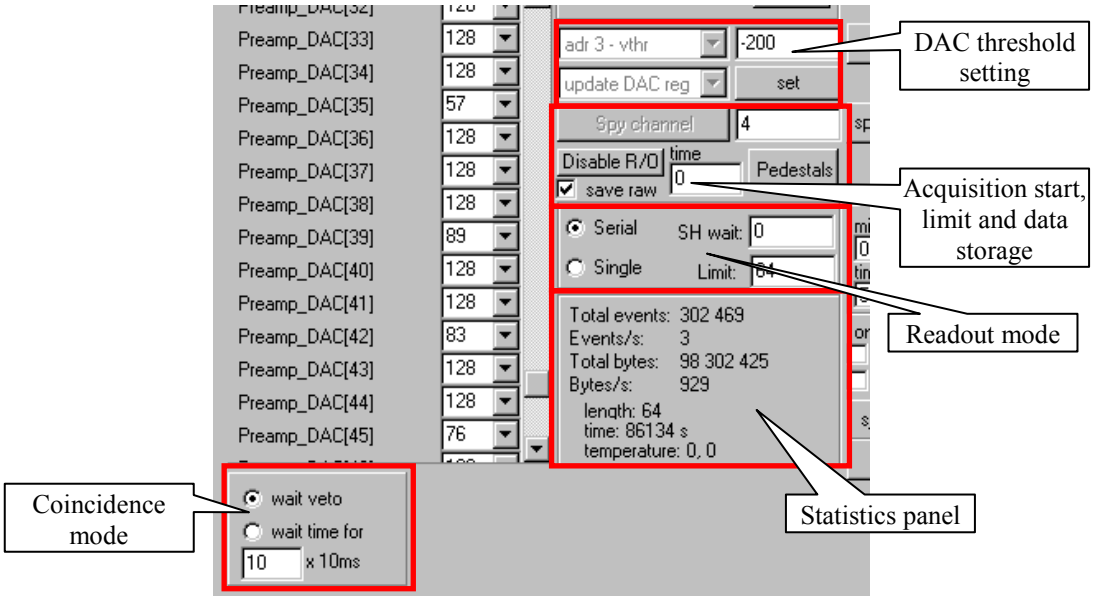

Figure 47: Components for acquisition and mode settings are highlighted. Acquisition overview shows information about the elapsed time, the events count and so on.

When further processing is needed, valid events are stored in the text file. Values of all 16 SiPM segments are stored to enable the investigation of the scintillating light distribution. Furthermore, the recorded event from the scintillator should match the

event from the pixel detector. The hardware synchronization starts both the acquisitions. A veto feedback makes the systems indifferent to new triggers until the acquisitions are finished, including the data transfer to the computer. Unfortunately, some occasional data loss was found during the first measurements. Limited possibility of the system debugging and no guarantee of the data reliability provided by the operation system Windows resulted in addition of the timestamp of the event packet reception. The timestamp was already available in Pixelman software. It is expected that the data timestamps of the two independent streams (from the scintillator and the pixel detector) are not same but very close to each other in comparison to the average time distance of the events. The example of the data recorded in the text file is shown in Figure 48.

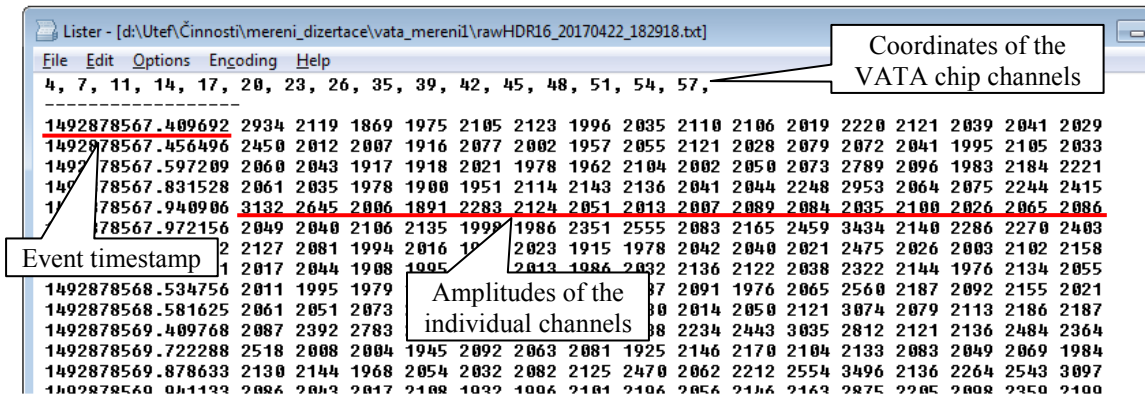

Figure 48: An example of events recorded in the file. Each line contains timestamp of the event and amplitudes of all 16 SiPM segments.

The main window is supplemented with several sub-windows displaying data during the acquisition. These windows were added as new functionalities were implemented.

The event window (see Figure 49) contains a graph of values of the last event. Different colors were used for better orientation. Blue points mark ASIC channels connected to 16 SiPM segments. Unconnected channels are red

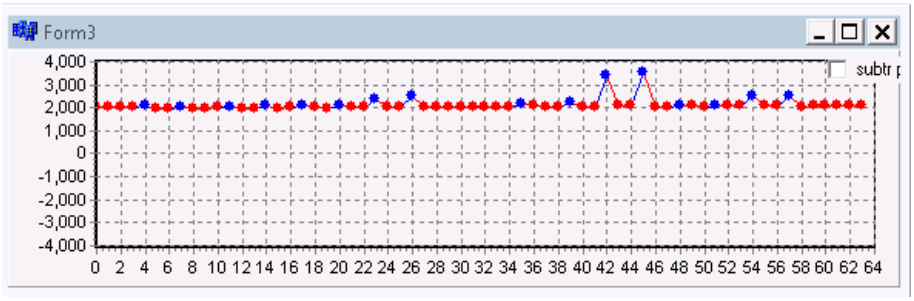

Figure 49: The event window shows two protruding channels. Red points mark connected ASIC channels while the rest is unconnected and red.

Incoming data is also used for generating spectra. Each channel has its own spectrum (see Figure 50). It is generated from values belonging to the particular channel. The integral spectrum with the adjustable range is calculated from connected channels (see Figure 51). Spectra are generated during the whole acquisition period. Restarting the acquisition causes spectra buffers to be cleared. Storage of spectra in several formats is available.

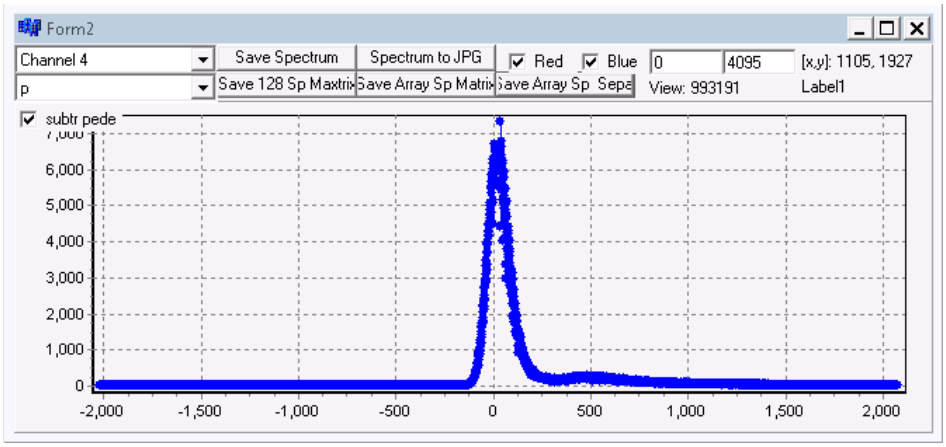

Figure 50: Window with individual spectra is depicted. Buttons allows to store spectra in several formats.

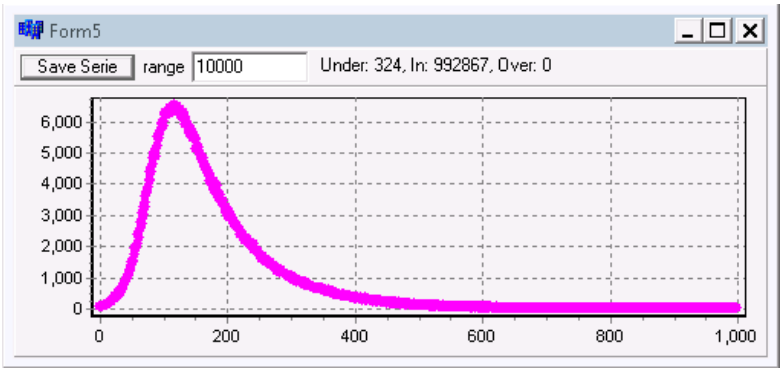

Figure 51: Window shows integral spectrum which is calculated from all connected channels. The range can be adjusted according to the signal magnitude.

The last window is prepared to display data in the matrix configuration. It is particularly appropriate for measurements in the coincidence with the pixel detector. The signal magnitude is expressed by a color. The color scale is adjustable to increase the contrast. The example (see Figure 52) shows the event where the main light is collected by the segment J. Adjacent segments sensed signal above the noise level because of the light sharing.

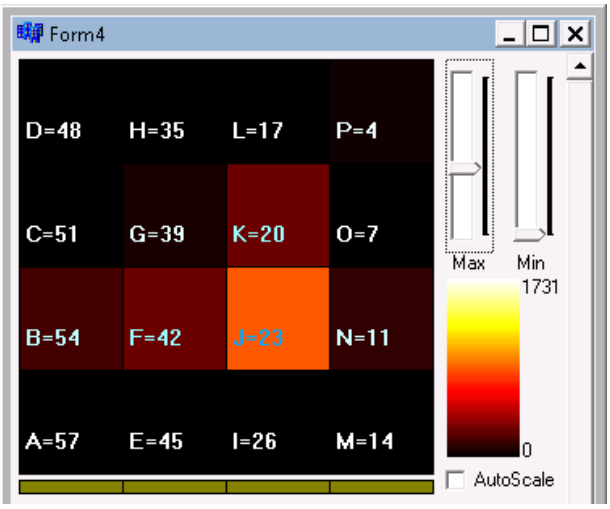

Figure 52: An example of the event visualized in a matrix configuration is depicted. Segment J measures the highest signal.

All the windows used during the measurement are shown in Figure 53. Updating of all windows is performed synchronously once per second.

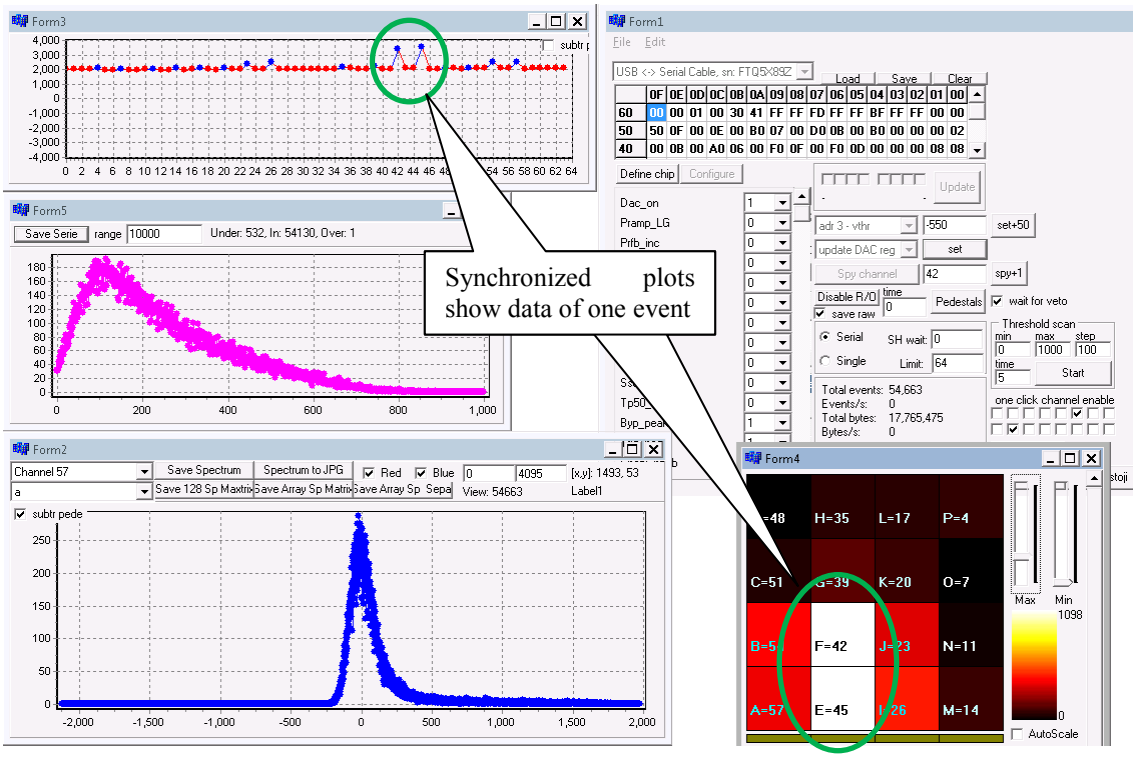

Figure 53: This picture shows a screen of the newly developed software for the SiPM readout system.

Processing thread

After the thread object initialization the endless loop is executed. Each time the loop is passed, an attempt is made to read the data from the driver buffer. When the packet is successfully read, it is parsed and checked for its reliability – header and checksum (see Table 6). Reliable data are forwarded to another procedure which is responsible for the storage to the file. Once per second the current data are visualized in GUI to prove to the user that the system is working.

11.2. Processing software

As an enhancement to the acquisition software, a data processing application was created to prove the synchronization abilities. This is the main thesis task which needs to be fulfilled to ensure the coincidence operation. The basic algorithm for coincidence data checking was verified and can be offered for further development because the processing of the data is always dependent on the experiment and many other requirements. There is no ambition to cover it by the universal and robust tool in the scope of the thesis project.

For the intended evaluation, only heavy charged particles are to be used. Pixel detector data have to be filtered. The raw data stream from pixel detector is preprocessed by the Back side pulse plug-in (possibly during acquisition). Its output file contains only clusters fulfilling the conditions. Cluster timestamps are preserved.

There are basically two inputs to the processing software – data from the SiPM array (including pedestals) and the pixel detector. Both data streams are stored in the files. The processing tool is available for offline processing, i.e. after the measurement. Of course, another measurement can be executed in the meantime. Two data streams are then opened in the processing tool. It is possible to go through the data event by event or process the batch. In both cases, only synchronous events are searched for. Permitted difference of the timestamps can be adjusted. The predefined value is 50 ms which is reasonable considering the data processing times and buffering in the computer. The coincident records can be further sorted by SiPM signal magnitude. The resulting matrixes can be stored to the files.

There are four types of frames available in the tool: current frame, integral frame and two conditional frames. For each of these frames one can choose if the raw data are used or the hit map is desired. Only the highest pixel of the cluster is used for generating the hit map. The pixel coordinates are preserved but the height is changed to one. Such an operation allows to investigate distribution of the events without any distortion caused by different energy (i.e. volume) of the clusters. The difference between integral frame and hit map can be seen in Figure 54.

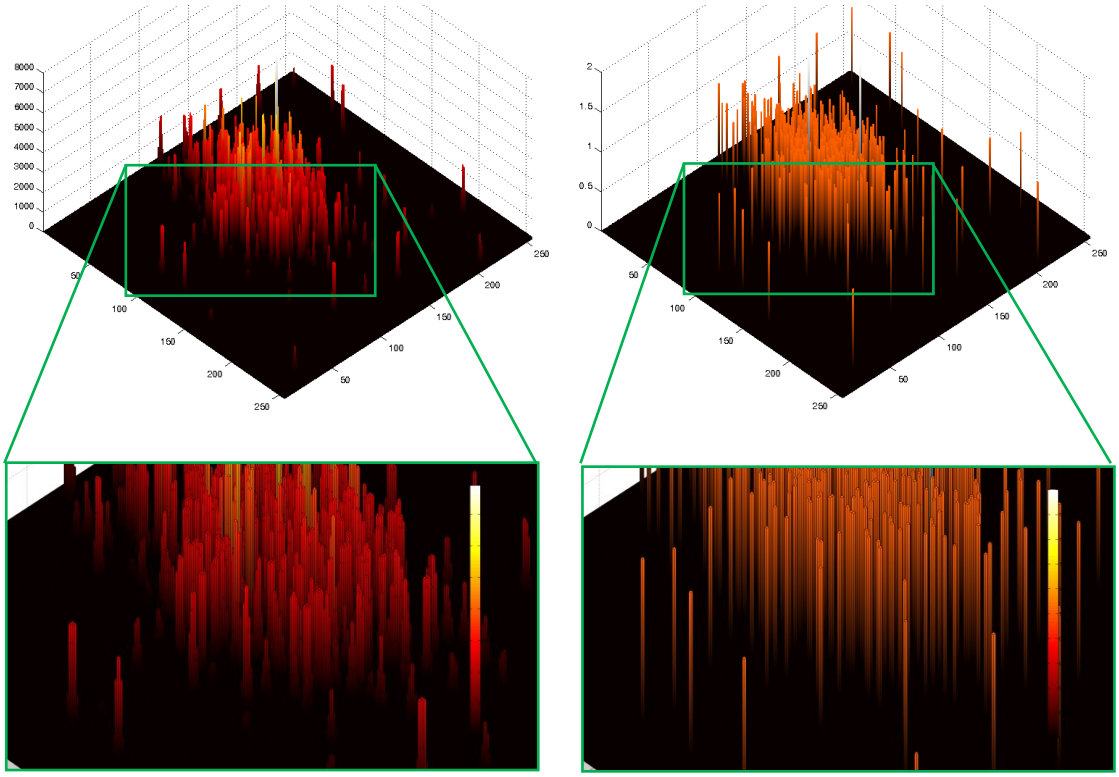

Figure 54: Difference between an integral frame and a hit map is shown in 3D plot. Integral frame (left, top) accumulates whole clusters while hit map (right, top) replaces cluster by the dot with the uniform height. Bottom pictures show the detail of the frames.

The main form of the processing software is shown in Figure 55. Data streams were properly loaded. The coincidence limit and conditions were filled in. One synchronized event which deposited energy in both detectors is displayed. Positions of the detections in both detectors are similar which means that the tool is working properly. Of course, more tests have to be made to prove the functionality with no doubts. Other demonstrations can be found in chapter 12.

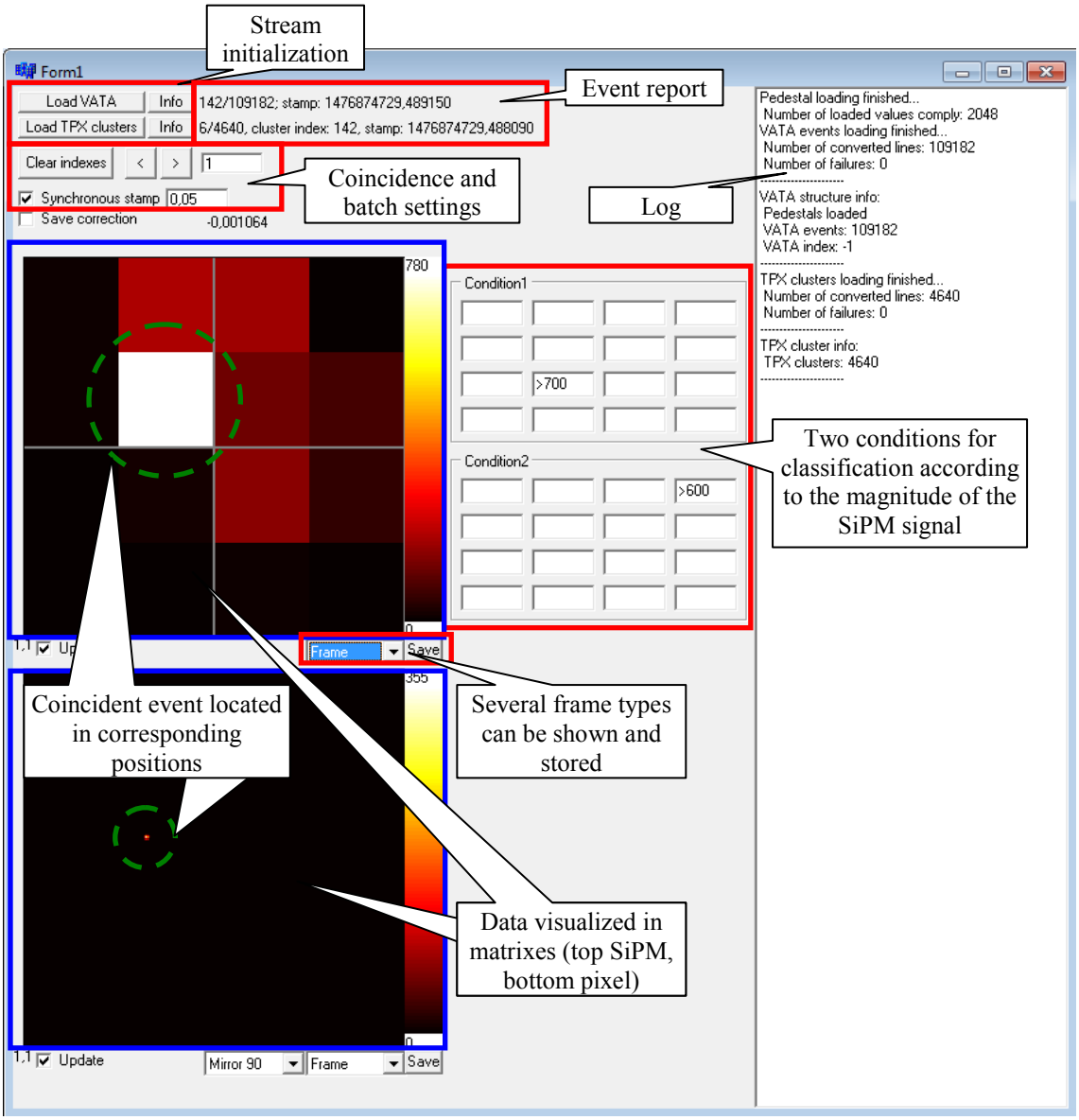

Figure 55: The main window of the processing software developed for the thesis project is shown. There are two input streams needed to be chosen. Parsing messages are written to the log. A number of events to be processed and a coincidence criterion can be adjusted. Additional filtering conditions can be assigned. The corresponding response of both detectors can be clearly seen.

12. Measurements and results

This chapter summarizes the measurements and results that have been achieved with the prototype of the newly designed device [RP1]. Measurements was performed even during the early development stages and served to verify individual parts of the design. New issues which arose during the measurements were corrected. Proper results could be obtained only with appropriate settings. Therefore, some effort had to be made to get familiar with the new system and to know the effect of the parameters on the measurement results. Although the exhaustive understanding of the behavior takes enormous amount of time, the successful operation was achieved. Significant measurement milestones are listed below.

12.1. ASIC readout system initiation

After the basic tests of the hardware-firmware-software interactions, such as a command transfer and handling, a response execution (change of a FPGA pin state, a DAC configuration etc.) and dummy data sending to computer, a cooperation of the FPGA with VATA64HDR16 was verified. The settings of the ASIC affect the operation as much as it does not work in case of the wrong configuration. A waveform generator and a 1 pF capacitor were used to simulate an input charge signal. There are two types of responses of the ASIC – a trigger signal and analog pulse available at the output. Unfortunately, there is no test circuit/chain (like JTAG or so) on the chip so the missing response, such as trigger, can be caused by the failure of the output buffer same as the preamplifier stage malfunction.

The analog pulse available at output lines looks like the one shown in Figure 56. Timescale of the plot 2 µs allows to display the signal before and after the pulse. The wavy trace around the pulse is caused by the noise picked up by the unshielded charge input. The shaping period corresponds to the expected value. The pulse rate and trigger rate was same as the frequency of the generator. No accidental events were observed.

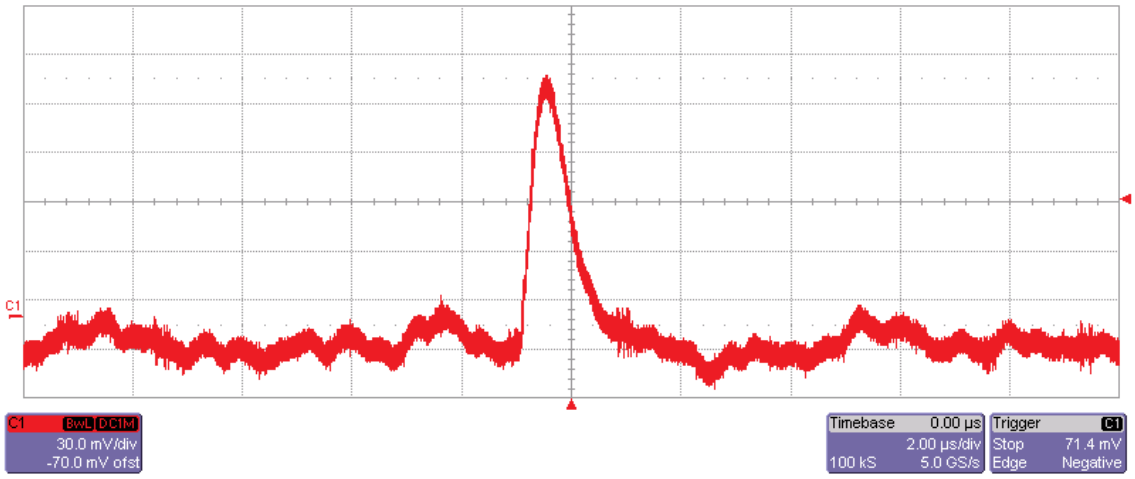

Figure 56: A response of the ASIC to the charge pulse simulated by the waveform generator and a 1 pF coupling capacitor is shown. The waveform shape before and after the pulse is caused by the noise.

This test proves that the chip is properly configured, the input signal can pass through the chip and the output multiplex and buffer work. A further step is to connect inputs of the ASIC to the SiPM array segments. There is minimal difference between the pulse simulated by a capacitor and the pulse from the SiPM. Sixteen of 64 available channels are occupied by the silicon photomultipliers. The ordinary readout routine can be tested to check the sample-hold function of the connected channels and timing of the readout procedure. Figure 57 shows the waveform recorded at the analog output as a response to the illuminating of the SiPM array by a LED. ASIC channels were switched one-by-one. Every time the sampled value is brought to the analog output. The limited strength of the output buffer causes the transition effect. Except that the output waveform is composed of the rectangular stubs.

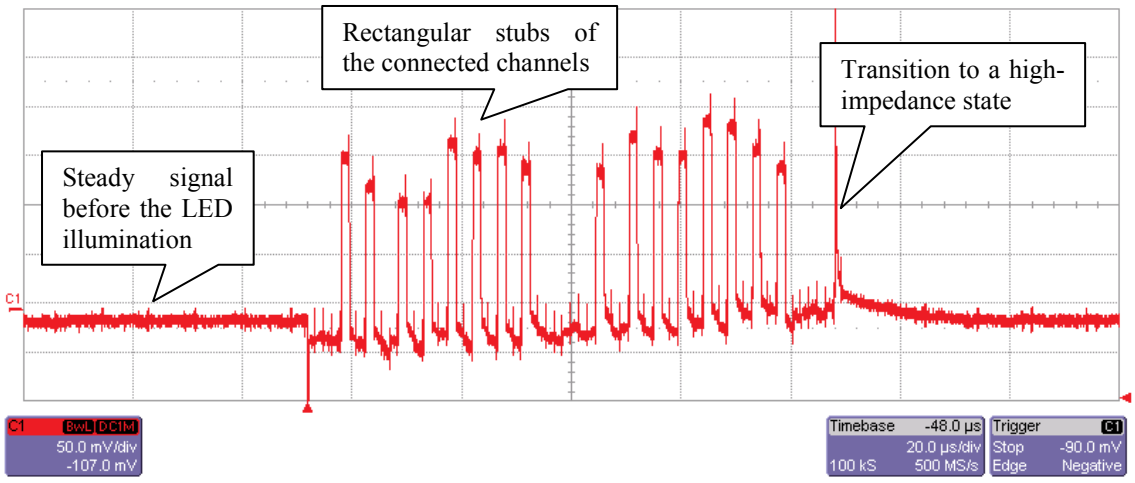

Figure 57: The output waveform of the ASIC is depicted. A LED illuminated the SiPM array connected to the 16 chip channels of the readout chip. Rectangular stubs correspond to the channel coordinates. Unconnected channels show only the noise superimposed to the pedestal value.

The readout procedure is working properly including the ADC conversion. Coordinates of the waveform stubs and decomposed data correspond to the channels to which the SiPM segments are connected. The triggering and the readout procedure can be considered reliable.

12.2. Pedestal correction

Pedestal values of the individual channels are voltage levels at the chip output when no input signal is presented. There is no way how to compensate it in the hardware. However, the software was prepared to subtract pedestal values during the measurement. A pedestal run has to be performed preferably before each measurement.

The trend of pedestal values of VATA64HDR16 is shown in Figure 58. The shape is similar for several chips, including other types from the VATA family, so it was not considered to be false. This guess was agreed by the manufacturer. The reason is the distribution of the power supply on the chip.

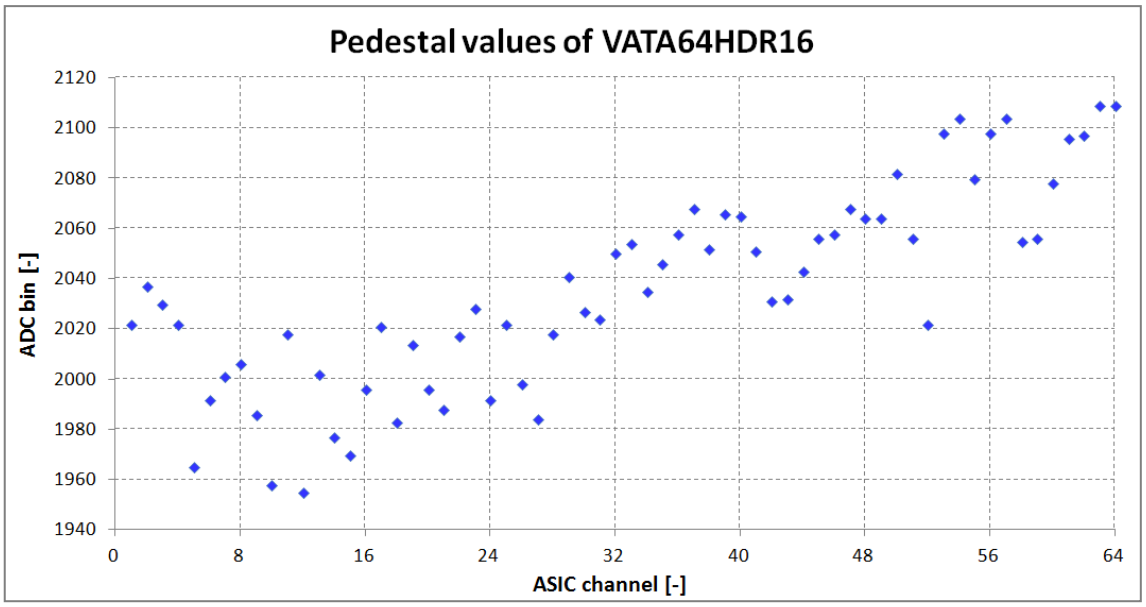

Figure 58: Pedestal values of the spectroscopic ASIC are depicted in the plot. The shape has increasing tendency. It is caused by the power supply distribution on the chip.

12.3. SiPM array equalization

The working readout allows to focus more on the tuning of the system performance. There is very limited agreement of the channels. The reason is the dispersion of the production technology of the analog parts, especially an ASIC slow shaping path, and SiPMs itself. Equalization of the channels aligns the responses so further processing, such as addition, is possible. There are two issues that should be minimized by the equalization:

- Different amplification – Level of the output signal as a response to the unified input varies channel to channel.
- Trigger rate– Despite the common threshold level, there is a different number of events generated by each channel as a reaction to the uniform stimulus.

The ASIC VATA64HDR16 can cover both issues. Input pad potentials can be adjusted that changes the bias across the SiPM segments. The operation point of the SiPM segment is $V_{sipm} = V_{bias} - V_{DAC}$. It changes amplification and ultimately the trigger rate too. The latter can be besides corrected by the dedicated register. A block diagram in Figure 59 explains the principle.

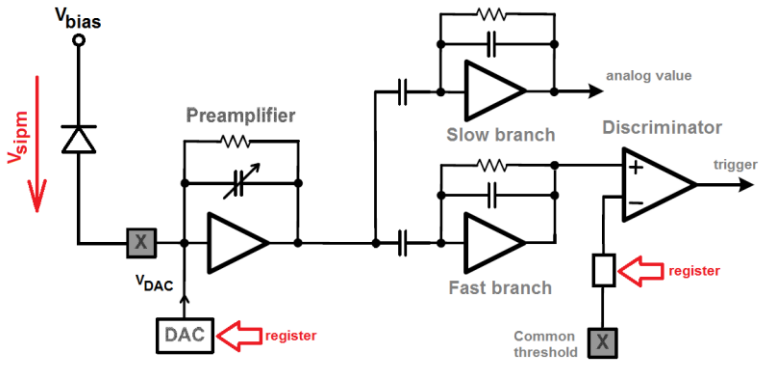

Figure 59: A block diagram of the ASIC structure shows the channel equalization possibilities. The SiPM segment is biased from a common source V_{bias}. The operation voltage V_{sipm} is derived and influenced by the input DAC settings. The amplification affects the trigger count too. The threshold level correction aligns the trigger responses of the channels.

A LED was used to generate light during the gain correction measurement. An ordinary blue 10 mm LED with an abraded lens was covered by a teflon white tape to defocus the light as much as possible. It was placed 20 cm far from the SiPM array so the impacting light was considered to be uniform. The amount of light generated by the LED was adjusted to be sufficiently above the noise level. Spectral peaks were fitted to obtain the coordinates of the mean values. These mean values before and after the gain correction are plotted in Figure 60.

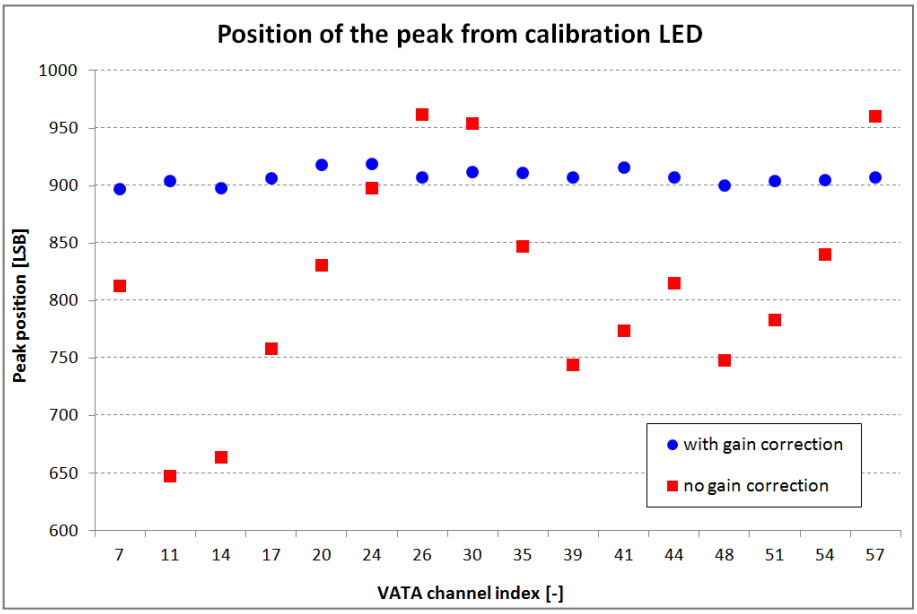

Figure 60: Mean values of the spectral peaks generated by the LED are depicted. Two measurements were performed. The gain correction of the ASIC channels was made between them.

A trigger discrimination level correction is available only in a narrow range. It was found at first tests that sometimes the available range is not wide enough. In such a case, the gain needs to be readjusted very slightly. It doesn't affect channel gain matching too much but the trigger rate is influenced a lot. The measurement of noise spectra of individual channels is the easiest way to see the correction effect. An example of the noise spectrum is shown in Figure 61. The goal is to get similar area of the small right-side peak in all spectra because it contains events triggered by the particular

channel. In case the particular channel is extremely noisy or broken, it is possible to disable it and discard its data.

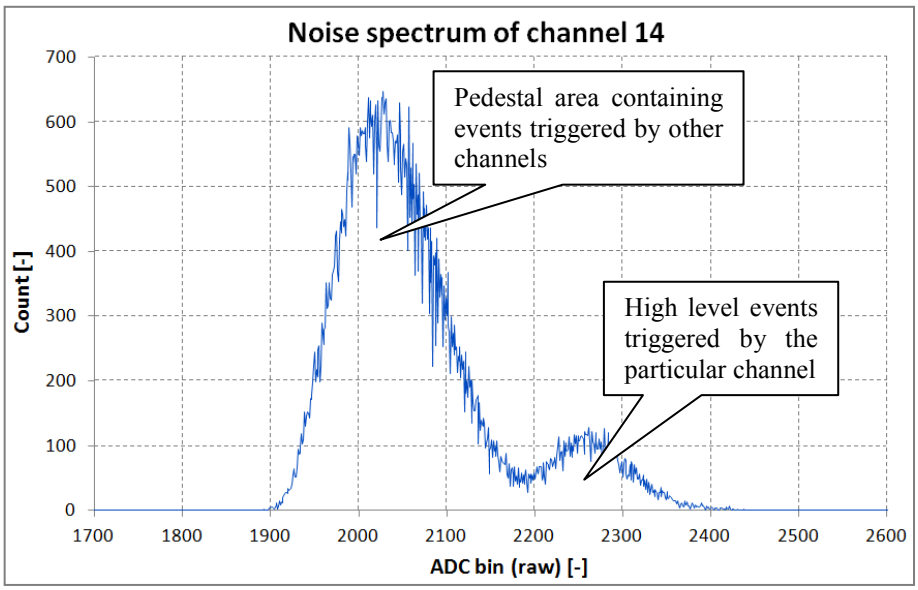

Figure 61: A noise spectrum is used for the trigger level optimization. The left side peak contains pedestal values while the right side peak accumulates high level events which were triggered by the particular channel. The goal is to balance all channels to get similar area of the right side peaks.

12.4. Summing SiPM elements

Equalization was further verified with the NaI:Tl scintillator (same piece as described in chapter 0) together with the summative effect of the signals from individual SiPM elements. The Cesium (Cs-137) source was used to irradiate the scintillator. It was already proved that the scintillator measures the expected spectrum even when sensed by the silicon photomultiplier. In this case, the difference is in the size of SiPM elements, the new readout system and data processing.

The example of four spectra of individual segments is shown in Figure 62. Other ones are very similar and their tail reaches similarly a value about 800. No noticeable peaks are in the individual spectra. It can be explained by the limited area of the SiPM segment. The amount of scintillating light is then low in comparison to the resolution. The sum spectrum generated by adding up all contributions of individual segments during the same measurement can be seen in Figure 63. The shape obviously changed and corresponds to the expected one. A photopeak and a Compton edge are clearly visible. The amount of scintillating light impacting the whole sensitive area is of course higher so the detail structure can appear. This is the proof that the summing of the digital data works. The slightly worse resolution in comparison to the bottom plot in Figure 31 is most likely caused by the older and noisier type of the SiPM technology (B-series).

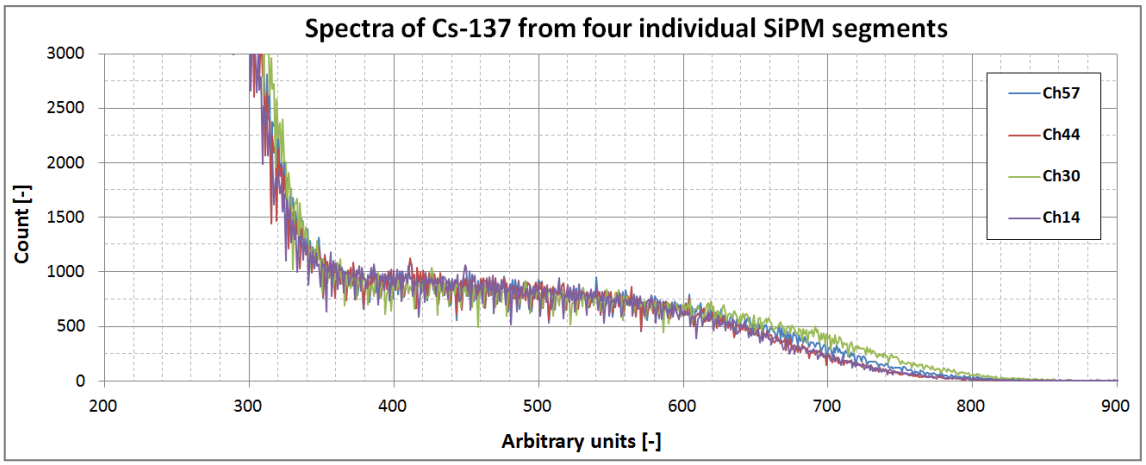

Figure 62: Spectra of four individual SiPM segments are depicted. No peaks are noticeable because of the low area of the segments.

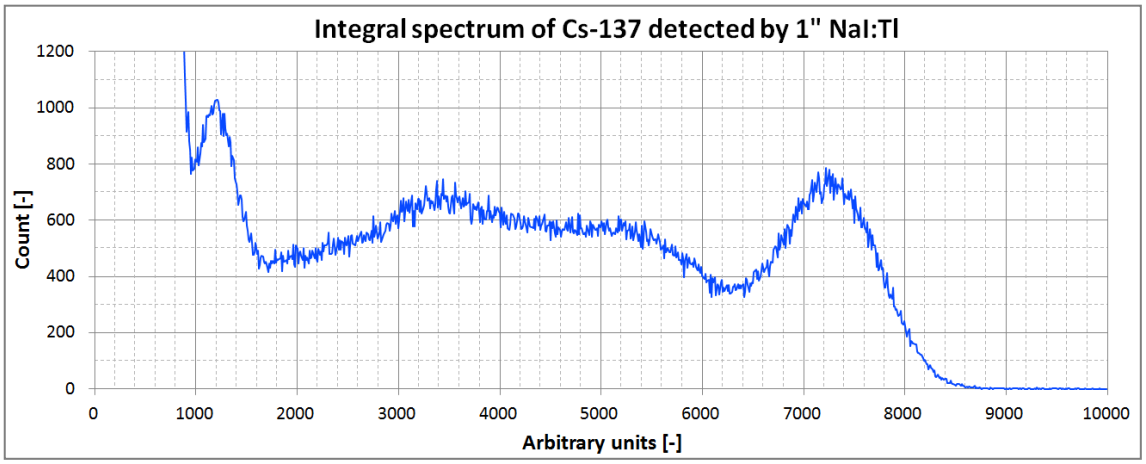

Figure 63: An integral spectrum obtained by adding up of the digital amplitudes of the individual elements.

12.5. Data synchronization check

This chapter is slightly ahead. A description of the measurement will be given in the next chapter along with other details. However, it is advisable to begin with the synchronization issue for better understanding.

The main contribution of the Multi-coincidence system is the possibility of pairing the data from different detectors. Despite the two independent parts and data streams, hardware and software synchronizations need to guarantee matching the data frames.

Unfortunately, there is only a fraction of events that makes the response in the pixel detector when triggered by the scintillator. Some reasonable yield has to be found even with low statistics. Example of two pairs of matching frames visualized in 3D plots can be seen in Figure 64. The array of silicon photomultipliers provides a coarse coordinate while more precise position is available from Timepix. The location of interactions (i.e. highest point) is very similar. The frequent detection in very different

locations means inoperative synchronization and measurement unreliability. This attitude was applied in the following measurements.

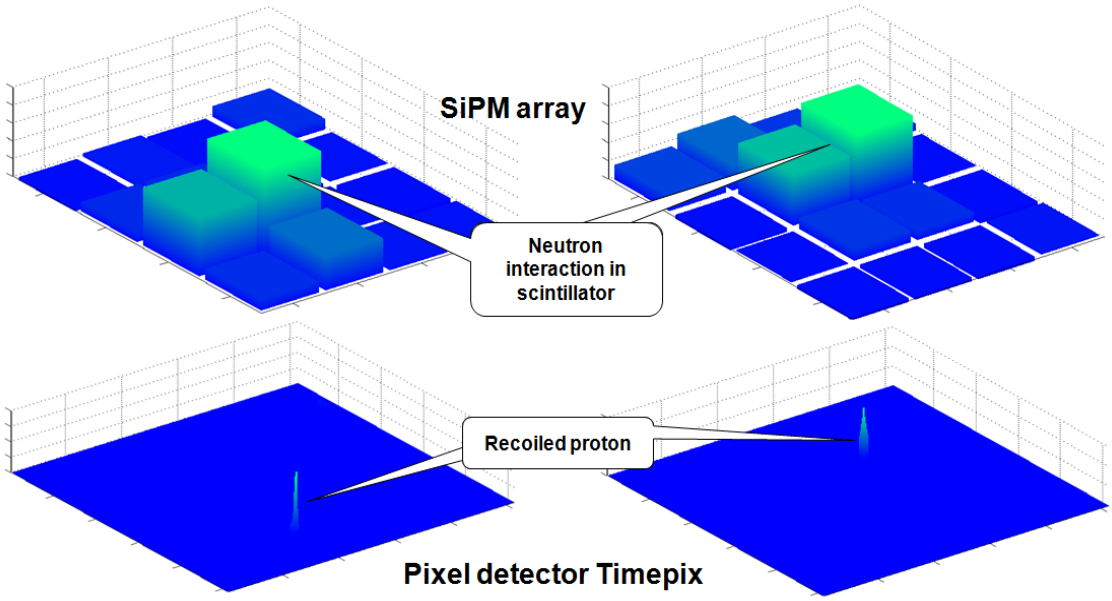

Figure 64: A 3D visualization of two pairs of matching frames is depicted. A coarse coordinate from the SiPM array roughly corresponds to the fine coordinate in Timepix.

12.6. Experiment with fast neutrons

The main experiment to verify the newly designed device was performed with fast neutrons. A laboratory radioisotope source AmBe (1 Ci, n = 2.2 MBq) available in the IEAP was used. The experiment took place in the impassable corridor at Van de Graaff facility [NP1] in satisfactory isolation from ordinary activities. The arrangement has been prepared to meet the requirements of the experiment while complying with the safety requirements for work with ionizing radiation, in particular by maximizing the distance between the apparatus and the computer and reduction of the exposure time. All activities associated with the experiment were carried out directly by the author.

A schematic cross section of the experiment is shown in Figure 65. The prototype of the Multi-coincidence system is placed on the thin board which is detached from the wooden desk. The space is used to place the radiation source because the prototype is sensitive the bottom. The guide lines were painted on the desk to help with the accurate placement.

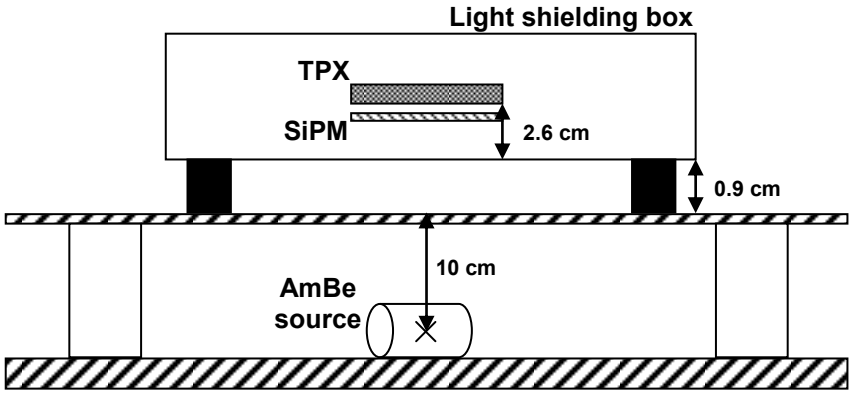

Figure 65: The cross section of the experiment with fast neutrons.

The AmBe source was placed below the sensitive volume. The distance is about 13.5 cm from the Timepix surface and about 13 cm from the scintillator. A series of measurements was performed with different settings and different positions of the radiation source.

Basic partial tasks were tested before the measurements to ensure smooth continuation, especially:

- Independent operation of Pixelman and Timepix (software trigger, fixed shutter period)
- Independent operation of the scintillator and its readout system (data accumulation should be a result)
- Response of Timepix to a trigger signal from the scintillator (HW trigger to Timepix, same count should be detected by both Timepix and the scintillator in case of rare events)
- Veto signal from Timepix blocking detection of scintillator events (same count in case of higher rates because of rejecting new events until the current one is completely processed)

The first sample measurement was made with the trigger signal restricted to only one SiPM segment (specifically O/7, see Figure 52). A Timepix acquisition window was set to 100 μs. The duration of the measurement was 52 minutes. Only data from Timepix was analyzed. The scintillator was used only for generating a trigger, relevant analog data are ignored for now. There were 7184 frames acquired carrying 6202 clusters. One tenth (619) of clusters were evaluated as correct. It means they fulfilled predefined conditions for the roundness and the size. Integral frames of the whole measurement before and after the cluster analysis are shown in Figure 66. The important outcome of this measurement is a fact that clusters, especially round blobs, are concentrated below or very near the triggering element of the SiPM array. Distant clusters, mainly long curly tracks, are generated by another process than proton recoil or are detected asynchronously to the trigger signal because of the considerable length of the acquisition window.

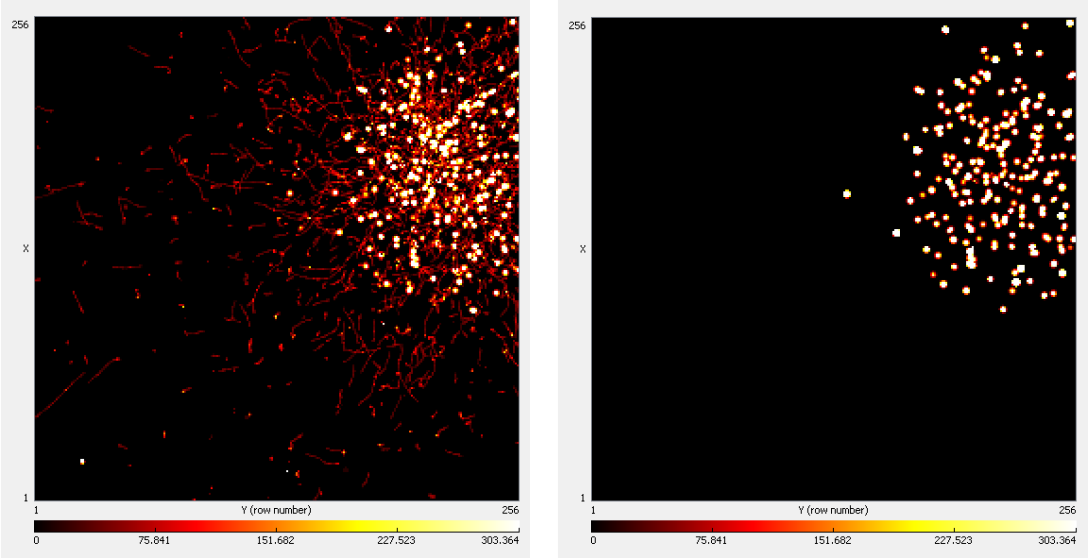

Figure 66: Integral Timepix frames of the measurement before (left) and after (right) the cluster analysis are shown. In both cases, concentration below one SiPM segment which was chosen to generate a trigger is clearly visible.

The random nature of the phenomenon was avoided by repeating the measurement with the choice of other trigger channels (F and J).

Another measurement with two different triggering channels (F and J) was performed to dispel all doubts. A comparison of this and the previous results can be seen in Figure 67. A lattice was added above the Timepix frame to show the position of the triggering SiPM segments. These results prove that the hardware synchronization of the system works reliably.

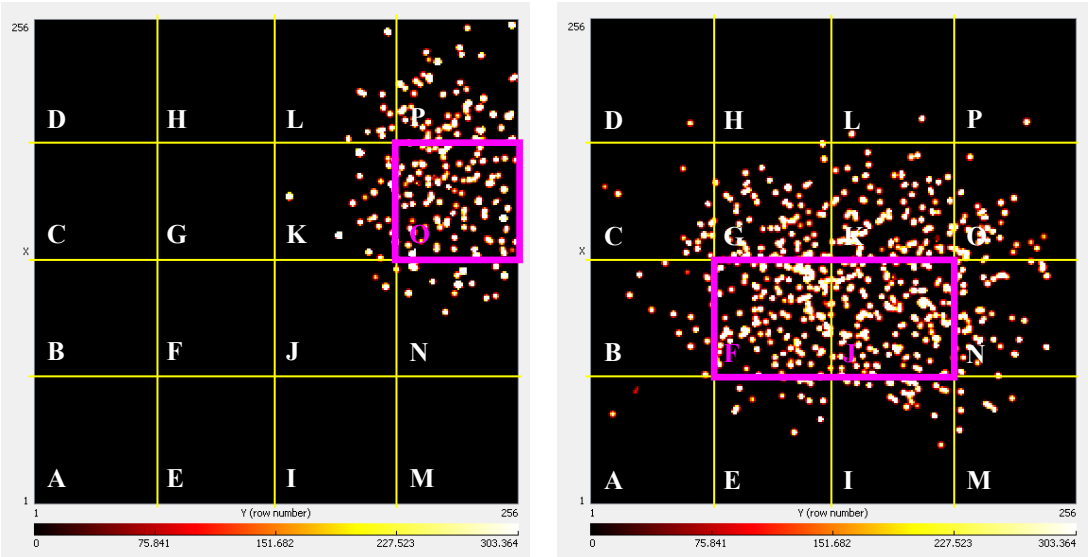

Figure 67: A comparison of the integral Timepix frames of two measurements triggered by different SiPM segments (marked by a pink rectangle) is shown.

There is a noticeable asymmetry of the cloud of events. The first explanation could be the accidental change of position of the Timepix or the scintillator. This guess was verified and appeared to be wrong. The asymmetry was caused by the improper

position of the AmBe source so the direction of the impacting neutrons was not perpendicular.

Up to now, the described measurements used low amount of active SiPM segments. It means only these segments generated trigger to start the acquisition of the system. Such an operation is not desired because it decreases the sensitive volume so the detection efficiency. The following measurement employs all SiPM segments and processes the raw data by the processing tool. Each Timepix cluster is to be located near the interaction point in the scintillator which is determined by the highest segment. Events, i.e. clusters, can be filtered according to the magnitude of the SiPM signal. Simple or more complex filtering condition can be set in the processing tool.

Figure 68 shows results of the processing of the first 100 events of the measurement. Integral frames accumulate all synchronous events. Default value of the timestamp difference (50 ms) was preserved. Condition 1 was met when the signal in one element was above 500. Condition 2 was fulfilled when another channel was over 500 and its adjacent channel is below 300 at the same time. It can be seen that Timepix clusters are filtered according to the defined condition.

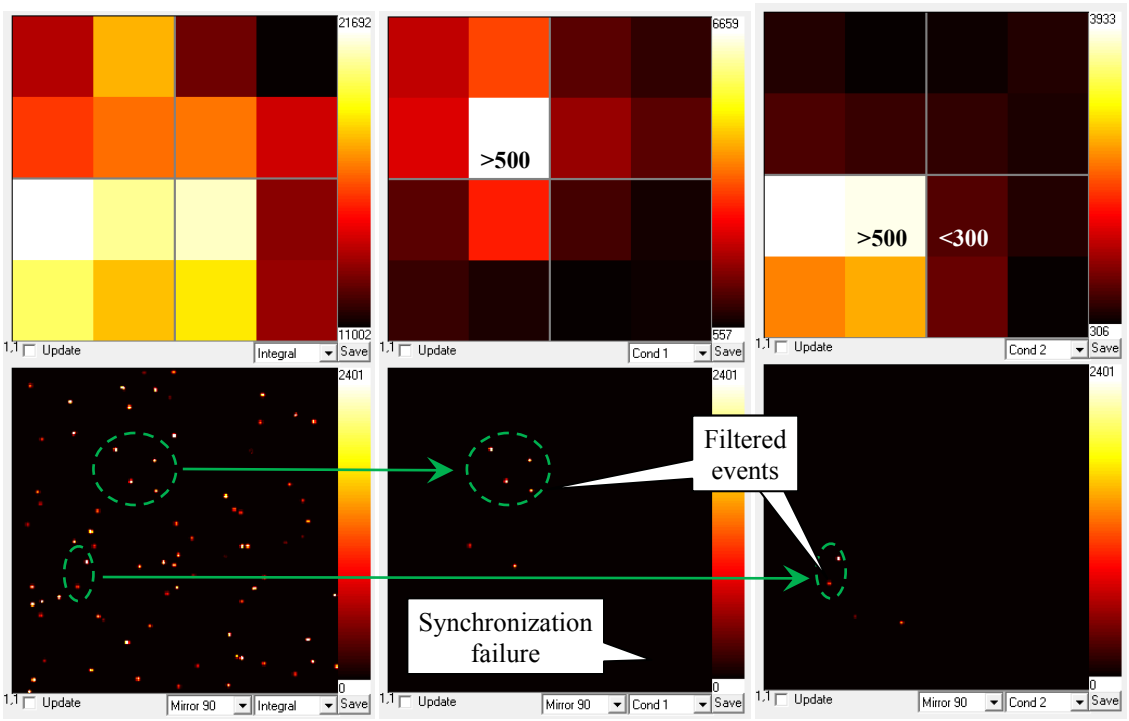

Figure 68: Three screens of the processing tool after investigation of the first 100 events of the measurement are shown – integral (left), condition 1 (middle), condition 2 (right). Setting of the conditions, i.e. magnitude of the SiPM signal, is stated in the SiPM frame (top). A missing number means that the segment is not considered. Timepix frames (bottom) show only events fulfilling the condition. Very distant Timepix clusters can be found and can be explained by too benevolent timestamp criterion.

Results of the processing of all available data are shown in Figure 69. A symmetric cloud is obtained for condition 1. Outstanding asymmetry in case of condition 2 is a consequence of the suppression from the right side. The integral frame from Timepix is uniformly covered as expected. Empty pixels (black) are caused by the limited statistics and the high granularity. On the other hand, the integral frame from the SiPM array shows the inequality among channels although they were matched. It should

be noted that the color scale highlights the difference because it doesn't start at zero. The standard deviation of the segments across the SiPM was calculated: σ = 8.3%. Compared to the resolution of the scintillator (about 20%), the channel discrepancy does not worsen the system performance.

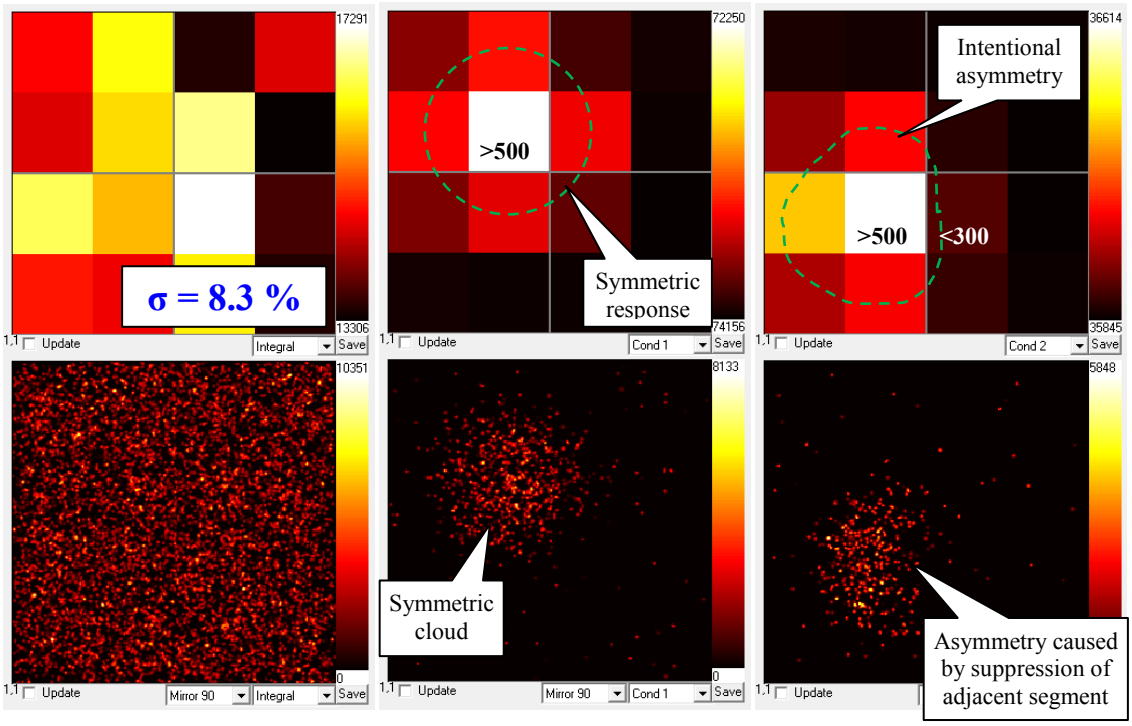

Figure 69: Processing of all the events resulted in these records. The integral Timepix frame (bottom, left) is uniformly covered. The SiPM frame (top, left) suffers from limited homogeneity. The condition 1 results (middle) shows symmetric clouds in both detectors. Compared to that, the condition 2 (right) filters events which form an asymmetric group. It is caused by the suppression of the events from the right side element.

It was observed there is a directional sensitivity of the detection. It is a very common feature of almost all detectors. But the common effect is decrease in detected events which has no sense in case the radiation field is undefined. Compared to that, the Multi-coincidence system brings the possibility to estimate the direction of the incoming neutrons based on the spread of the events.

Four measurements were performed with different positions of the AmBe source, see Figure 70. The impact angles were as follows:

- Position 1 – perpendicular in x and y direction
- Position 2 – -20 degrees in x, perpendicular in y direction
- Position 3 – -40 degrees in x, perpendicular in y direction
- Position 4 – +20 degrees in x, -20 degrees in y direction

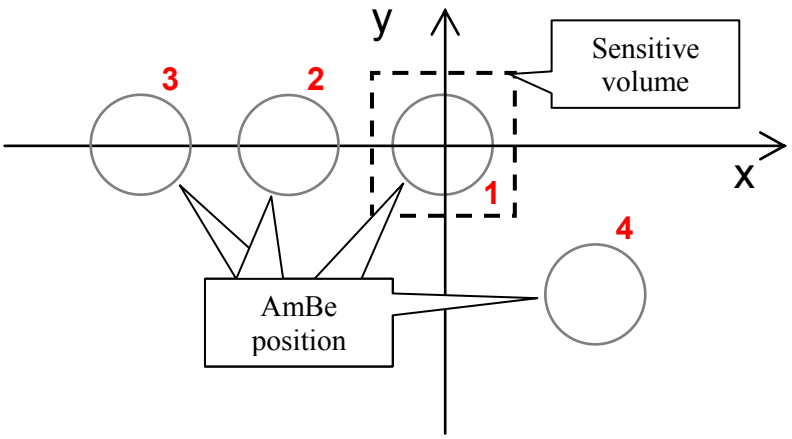

Figure 70: A sketch of the measurements arrangement (top view). The AmBe source positions are represented by circles. The sensitive volume (a dashed square) is placed to the origin of the coordinate system. Index of the measurement is assigned by the red number

Data from the Timepix detector and the scintillator was recorded. The cluster analysis of Timepix events was performed as usual. Clusters were filtered according to the magnitudes of the scintillator signal. Evaluation conditions were fixed (signal magnitude) but the coordinates, where it was applied, changed. The purpose of the operation is to select the response cloud and observe its shift when changing the position of the radiation source. Figure 71 shows the naming convention for the filtering conditions.

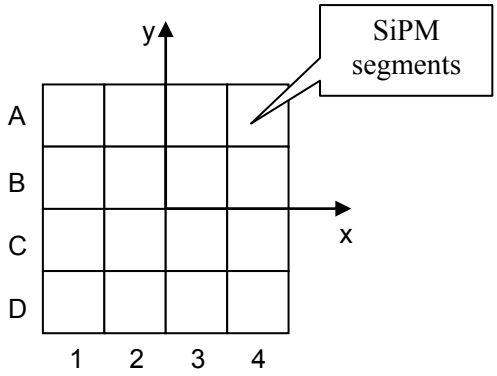

Figure 71: The image shows the naming convention established for the conditions definitions.

Filtering conditions are as follows:

1) (B1 > 500) ∧ (C1 > 500)
2) (B1 > 300) ∧ (C1 > 300) ∧ (B2 > 300) ∧ (C2 > 300)
3) (B2 > 500) ∧ (C2 > 500)
4) (B2 > 300) ∧ (C2 > 300) ∧ (B3 > 300) ∧ (C3 > 300)
5) (B3 > 500) ∧ (C3 > 500)
6) (B3 > 300) ∧ (C3 > 300) ∧ (B4 > 300) ∧ (C4 > 300)
7) (B4 > 500) ∧ (C4 > 500)

High threshold or more complex logic operation reduces the yield, i.e. number of events that can fulfill the condition. In the extreme, it can even cause that no event is able to fulfill the condition. That is the reason why the threshold was lowered for the

four-segment conditions. Same logic pattern was used for investigation the data measured with the AmBe source in four different positions. The output of the processing is the integral hit map. Horizontal and vertical projections of the hit map matrix create vectors which were further used for evaluation. The example of projections can be seen in Figure 72.

The shape of the projection changes according to the direction of the incoming neutrons. Further investigation and calibration can determine the direction. Exhaustive data analysis is not the intent of this work, so only the basic parameters demonstrating the possibility of directional detection are stated.

The center of mass of the projection is obtained by formula (10). The range is adapted to the size of one matrix which was used in the thesis project.

$$\mu = \frac{\sum_{i=1}^{256} x_i y_i}{\sum_{i=1}^{256} y_i} \tag{10}$$

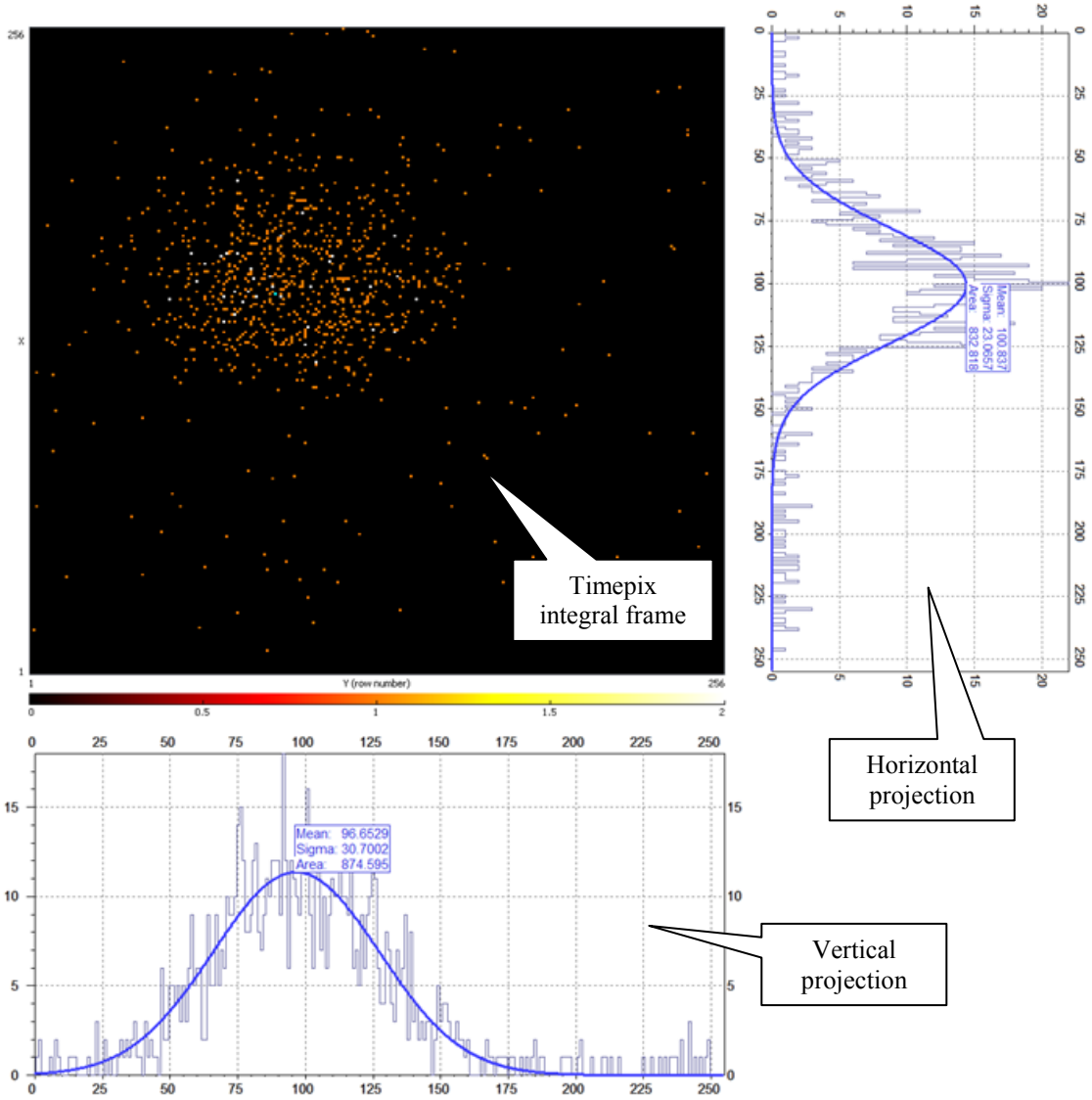

Figure 72: Horizontal and vertical projections of the Timepix integral frame are shown. The vertical projection is fairly symmetrical. This does not apply to the horizontal projection which is influenced by the direction of the incoming neutrons.

The described measurements were performed and recorded data processed according to the described procedure. Table 9 summarizes centers of mass determined for four neutron source positions and seven filtering conditions.

Table 9: Results of four measurements are summarized in the table. Centers of mass for horizontal and vertical positions were calculated. Measurement statistics can be found including duration, event rate (number of events of the scintillator) and neutron rate.

Position 1								
Condition		1	2	3	4	5	6	7
Center of mass	Vertical	33	73	102	131	163	193	225
	Horizontal	129	126	129	129	129	127	130
Filtered events		252	147	205	114	246	144	181
Start time	4.5.2017 14:28:28		Duration [s]	22949	Events	160179	Neutrons	9548
End time	4.5.2017 20:50:57				Ev./s	6,98	Neut./s	0,42

Position 2								
Condition		1	2	3	4	5	6	7
Center of mass	Vertical	31	68	102	126	159	193	225
	Horizontal	144	144	141	141	142	141	142
Filtered events		361	242	375	254	425	229	312
Start time	4.5.2017 21:00:10		Duration [s]	45831	Events	309461	Neutrons	15025
End time	5.5.2017 9:44:01				Ev./s	6,75	Neut./s	0,33

Position 3								
Condition		1	2	3	4	5	6	7
Center of mass	Vertical	37	70	96	128	160	194	226
	Horizontal	152	156	154	155	155	152	152
Filtered events		916	620	909	634	1010	563	759
Start time	5.5.2017 10:48:11		Duration [s]	186744	Events	1000881	Neutrons	32336
End time	7.5.2017 14:40:35				Ev./s	5,36	Neut./s	0,17

Position 4								
Condition		1	2	3	4	5	6	7
Center of mass	Vertical	25	56	87	113	150	179	210
	Horizontal	119	116	117	121	121	120	120
Filtered events		309	251	366	252	400	281	393
Start time	7.5.2017 15:02:09		Duration [s]	49993	Events	323252	Neutrons	13467
End time	8.5.2017 4:55:22				Ev./s	6,47	Neut./s	0,27

Centers of mass of horizontal projections presented in the graph depending on the impact angle of neutrons shows a monotone trend (see Figure 73). The filtering condition has no impact to the trend so the center of mass coordinates was averaged and trend equation calculated (see Figure 74).

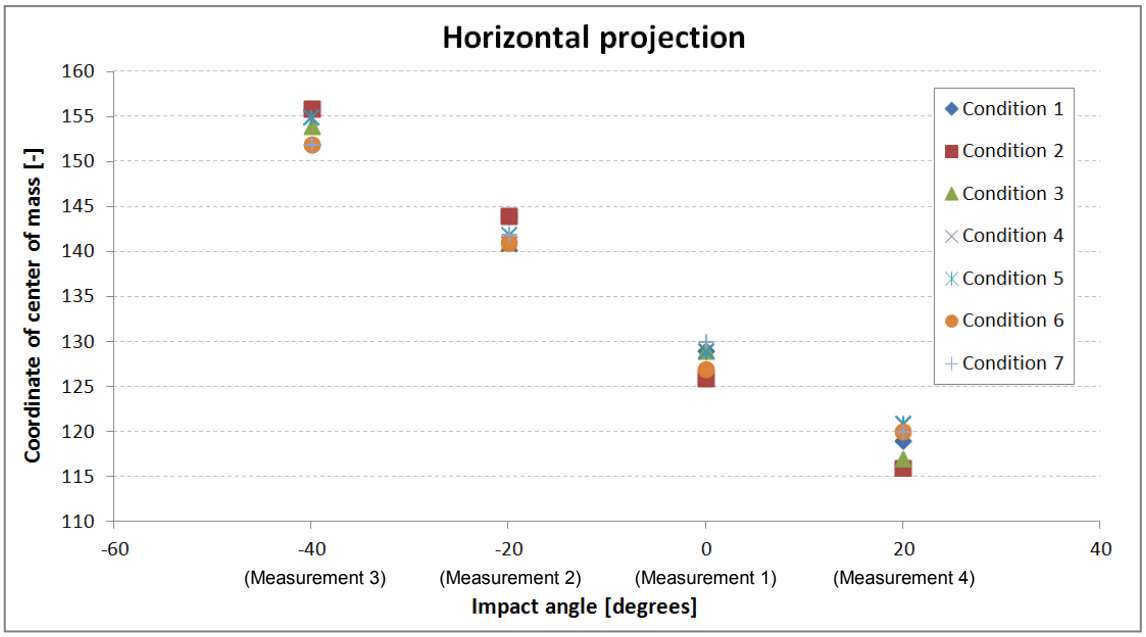

Figure 73: Coordinates of the center of mass of the horizontal projection are arranged according to the impact angle of neutrons. The monotone trend is evident.

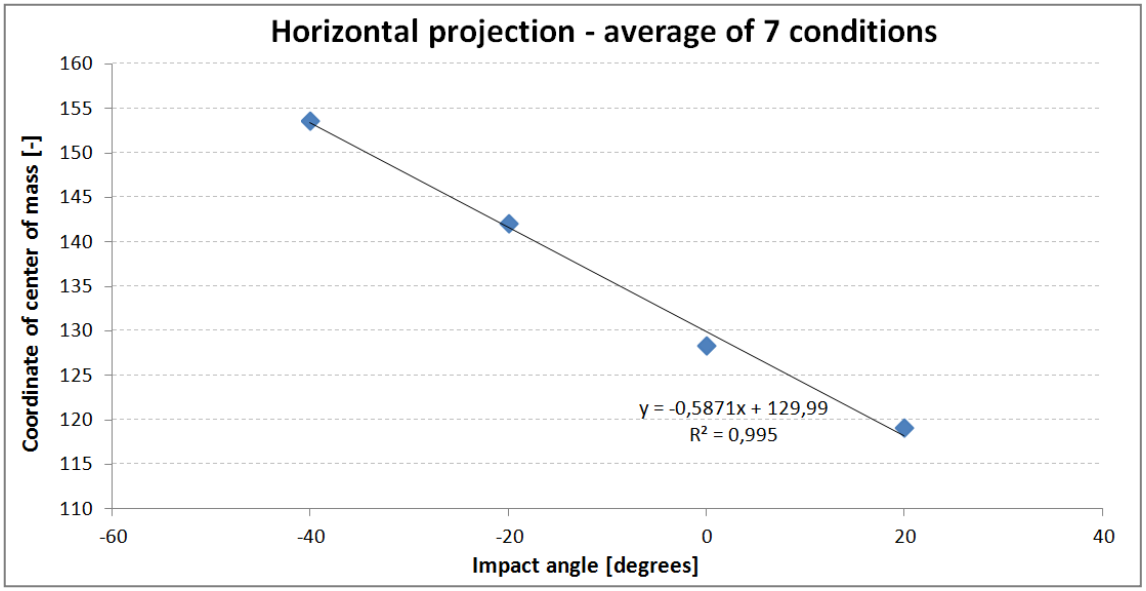

Figure 74: The trend is preserved regardless the filtering condition. The average coordinate was calculated and trend equation expressed.

The angular resolution calculated from the horizontal projections is 1.6 degrees.

Similar analysis can be made for vertical projections. In this case, the configuration of the measurements results in one angular change in measurement 4. Previous three measurements were done with same impact angle in the direction of the vertical projection. A raw data plot is shown in Figure 75.

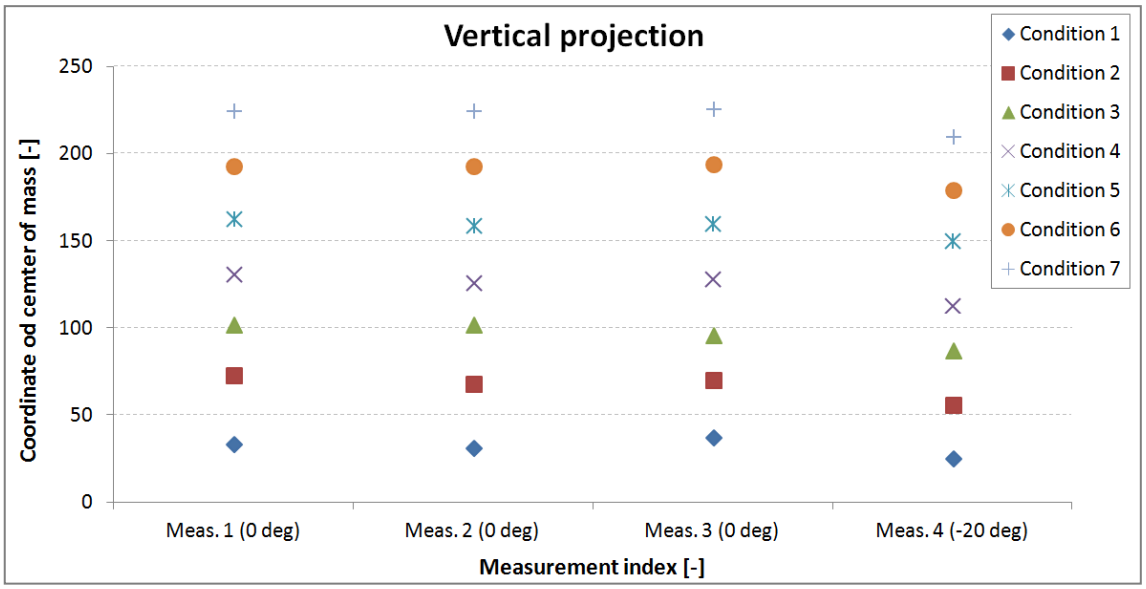

Figure 75: A plot of raw values of vertical projections is depicted. There is very broad scale because of diverse coordinates resulting from the filtering conditions.

It is apparent the coordinate of center of mass of vertical projection is very similar for the particular condition. Better evidence is reached when raw values are subtracted from the average calculated for particular filtering condition. Figure 76 shows a plot of coordinates of vertical projections after subtraction of the average.

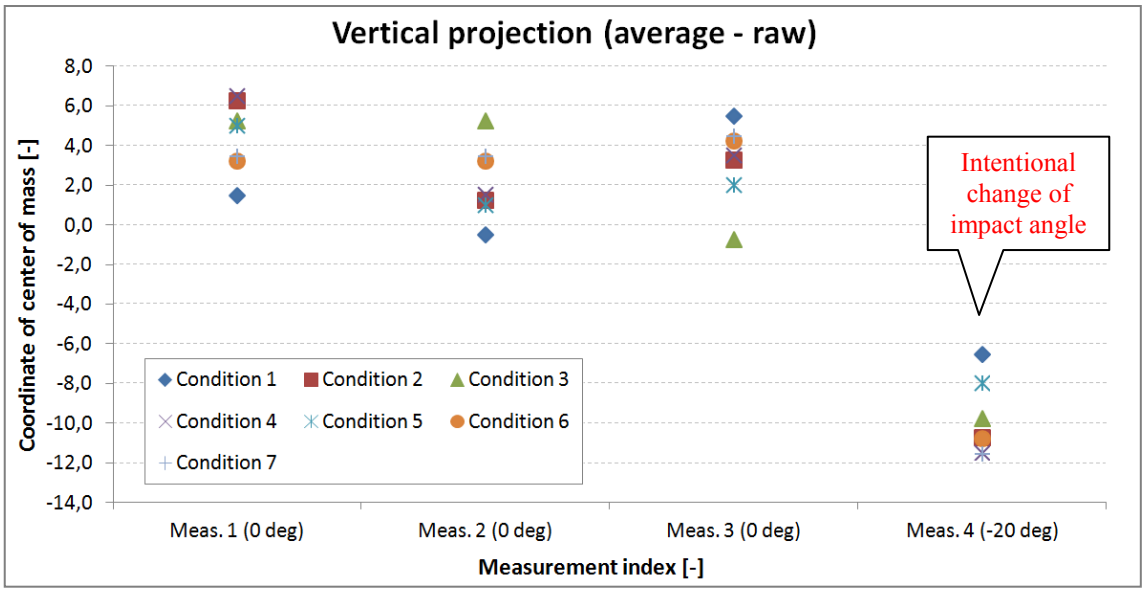

Figure 76: A plot of vertical projections of the four measurements after subtraction of the average shows a good correspondence of three measurements while the fourth one differs significantly because of the different position of the neutron source.

The difference of the measurement 4 is evident. Angular dependence suffers from lack of data because only two positions were measured. A rough estimation can be done by averaging of results of same impact angles (0 degrees and -20 degrees) as shown in Figure 77.

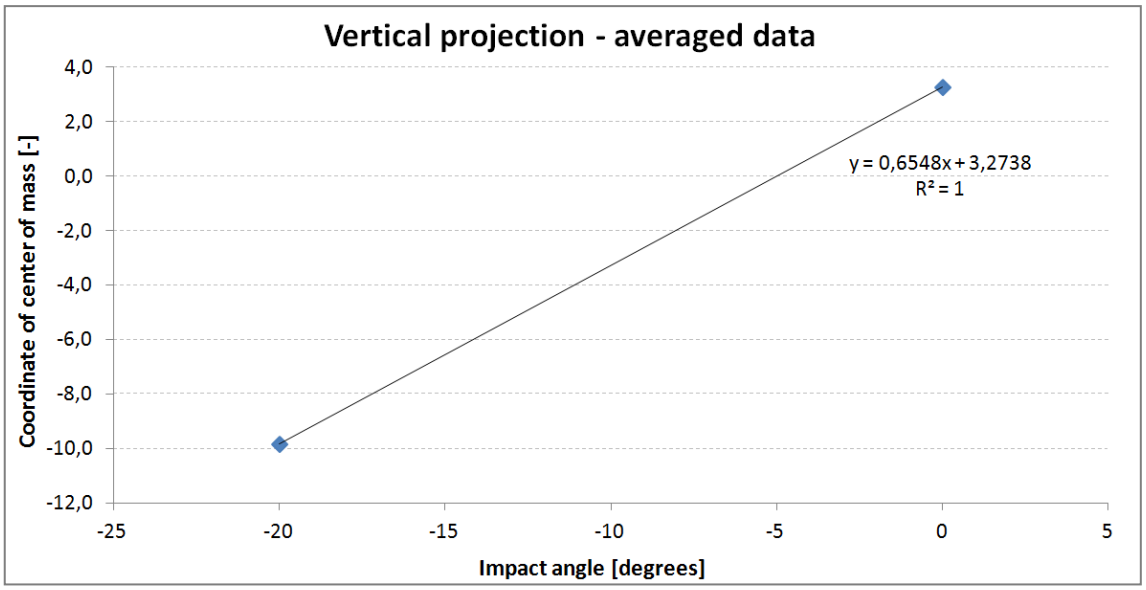

Figure 77: The trend of the angular dependence of vertical projections has very limited statistical basis. Only two angles were measured in this direction.

The angular resolution calculated from the vertical projections is 3.1 degrees.

The resolution calculated from vertical projections is worse in comparison to that from horizontal projections. It can be explained by different projection shapes (wider) which are dependent on filtering conditions. These results were achieved with one particular set of conditions and are more a consequence of processing than to be labeled as a device parameter. There are many available conditions that can be used to process the measured data. More selective conditions, such as with higher threshold or coincidence for more segments, are more advantageous but dramatically decrease the yield. The optimization is desired and can be considered as a task for future.

The contribution of the thesis project is based on merging of two different systems – the silicon detector Timepix and the scintillator covered by the array of SiPMs read by the spectroscopic chip. Both parts provide analog information about the signal deposited is the detectors. So far, analog values from SiPMs were used for filtering Timepix clusters. The resulting directional dependence was already described. Further information about the radiation field is the energy. The energy of the primary neutron can be reconstructed when the collision angle and the energy deposited by the recoiled proton is known. The collision angle can be derived from the incoming direction of the neutron and the impact angle of the recoiled proton to the silicon detector. Both values are available by the Multi-coincidence system. The energy deposited by the recoiled proton is shared by the materials which are passed through. Assuming full absorption in the silicon detector, the rest of the energy is deposited in the scintillator and a bit in the air. The scintillation light is proportional to the energy loss and the newly developed system provides the value. It can be included to the energy calculation that will increase the precision.

Figure 78 shows individual spectra from three SiPM segments. The first segment (blue) was used for triggering the system. The spectrum shows highest energies because the threshold was set as much as necessary to avoid noise. The adjacent channel (red) contains events with rather low energies but some events are comparable to that from

the triggering channel. This happens when the interaction point is just between segments and the light is significantly shared. The distant segment (green) measures only noise because no light from the triggering particle can reach it. Such a behavior is

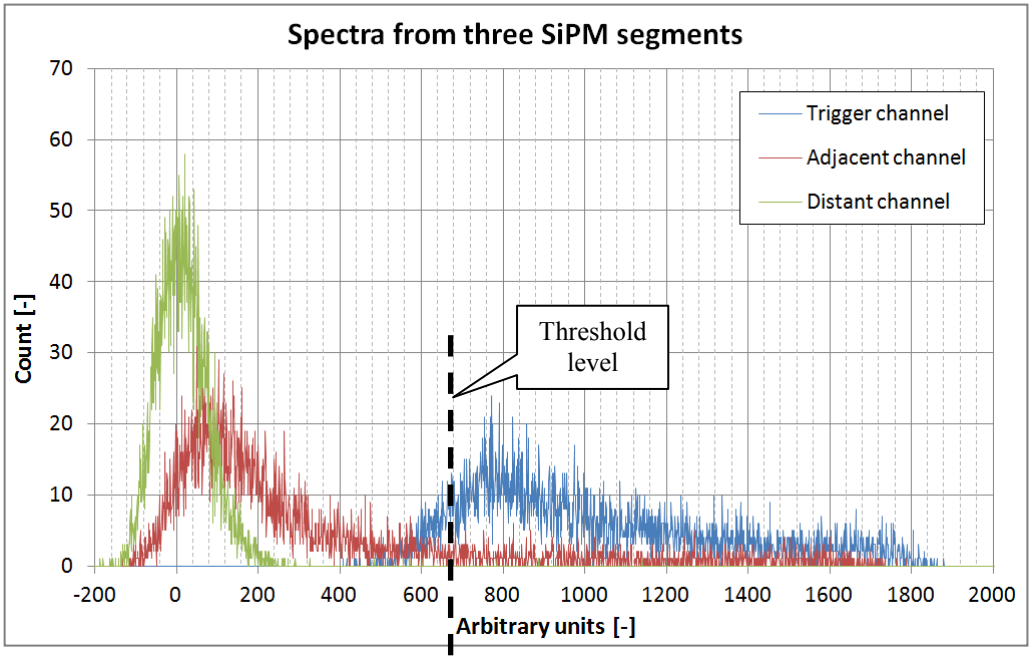

Figure 78: Spectra from three individual channels have different shapes. The trigger channel (blue) collects highest amount of light which can be slightly shared by the adjacent channel (red) while the distant channel (green) has no such a contribution.

The resolution of the plastic scintillator is expected as very poor, moreover when the light is sensed by the small area SiPM segment. The region of the triggering spectra around the threshold level was fitted by error function (see Figure 79). Its sigma is very similar to the sigma of the Gaussian fit of the pure noise from the distant channel (see Figure 80). Thus, the noise has additive character and the resolution will improve when more segments will be added.

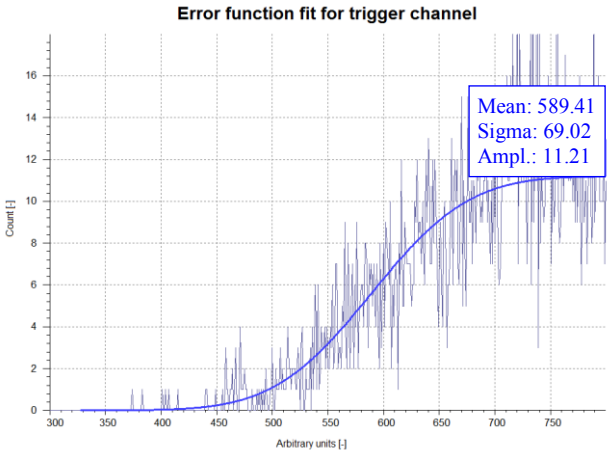

Figure 79: Error function fit of the threshold region with the fit parameters is shown.

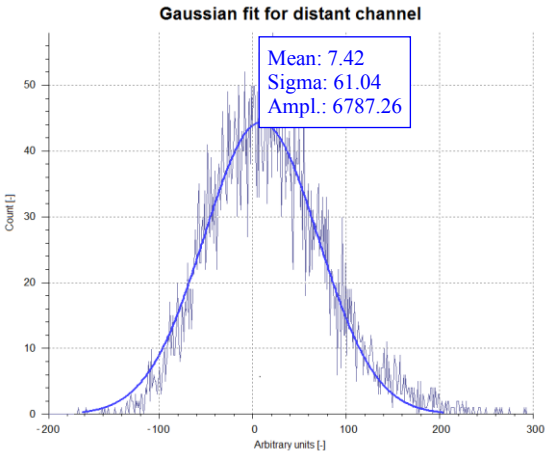

Figure 80: The adjacent channel spectrum filled mainly by the noise is fitted by the Gaussian function.

13. Results comparison

The objective of this thesis is to develop the new method and algorithm for particle detection and recognition. The effort resulted in the new instrument which was used in experimental measurements simulating the real use. The instrument itself is the original contribution of the thesis author and no competitive device can be found so far. The more important is what the device allows and what results can be achieved in comparison to other results/works.

The first comparison should be between the simulation and the measurement. The simulated detection efficiency was 4.7×10^{-4}. There is only one measurement comparable to that (perpendicular geometry). The obtained efficiency is 2×10^{-4}. It is a slightly lower value than the simulated one. There can be found two explanations: a) there are 1 MeV cuts for both detectors in the simulation which are not guaranteed in the real measurement and are probably higher, b) the simulation procedure doesn't take into account the limitation of the data transfer speed of the system. In spite of that, the real detection efficiency is appropriate when considering device optimization status.

A comparison with other system is desired despite the lack of comparable devices and information. The work is highly focused on the directional detection of neutrons. There are two approaches. The first one employs a collimator which defines the field of view of the detector. Increasing the collimation effect by narrowing the aperture makes the directional resolution better but reduces the detection efficiency [44]. The second approach, which is exploited in this work, is the coincidence of several channels. The performance of the system, particularly the detection efficiency, is influenced by system parameters, such as size of material. Detectors based on gas [45], fluid [46] or plastic [47], [48] can be found. Some parameters were found for comparison which can be seen in Table 10.

Table 10: Some parameters of directionally sensitive neutron detection systems are stated and compared to the solution achieved and presented in this thesis (highlighted as red).

Author	Ref.	Principle	Material, detector and size	Detection efficiency	Ang. resol. [deg.]
Iguchi et al.	[44]	collimator	Up to tens of centimeters	$1.1\text{x}10^{-4}$	24.5
				$1.9\text{x}10^{-5}$	3.6
Peel et al.	[47]	coincidence	Scintillating fibers, multi-anode PMT, detector size (one dimension) 10 cm, huge electronics (VME)	-	< 10
Marafini et al.	[48]	coincidence	Scintillating fibers, CMOS light sensor, $10\times10\times20$ cm^3	$8\text{x}10^{-3}$	-
Archambault et al.	[46]	coincidence	Sensitive area 4×2.5 cm^2, detector >15 cm long, acoustic sensors, oscilloscope based DAQ	-	< 8.1
Son et al.	[45]	coincidence	$30\times30\times30$ cm^3, 2-D micro-well detektor, transient digitizers	-	< 5
Mašek et al.		coincidence	Sensitive volume $2\times2\times1$ cm^3, array of SiPMs and silicon pixel detector, FPGA bases DAQ	2×10^{-4}	< 2

The comparison shows that the results achieved by the thesis project are just as good or better as competitive solutions. The significant benefit is the angular resolution

which overcomes the currently available values. The lower detection efficiency is determined by the size of the sensitive volume and the material used. However, it should be noted that the whole concept supports the stacking of sensitive layers, thereby increasing detection efficiency. The small dimensions and the own custom-made design of the electronic system are also an advantage, especially for optimization and further extension.

14.Conclusions

Simple detectors of ionizing radiation can provide only limited information about radiation field. Restrictions are mainly on the side of the physical processes in the detector material. Complex systems are valuable devices because they can provide more comprehensive characterization than available by simple detectors. It is repaid by the overall complexity of the design. Therefore, such systems are mainly a domain of large detector experiments (in CERN and others).

The new enhanced method for neutron detection which resulted in the design of the compact Multi-coincidence system presented in this thesis is based on merging of two different detection technologies in closed geometry. The activities and the content of the work were carried out in accordance with the stated goals. The author's contribution, new innovative approach and fulfillment of the goals can be summarized as follows:

- **Design the structure which is able to detect, recognize and characterize different particle types. The main focus is devoted to position and directional detection.**

The unique silicon pixel detector Timepix has excellent position and energy resolution. Unfortunately, it has demerits which decrease its qualities, such as missing self-triggering feature or fast neutron interaction indefiniteness. The new solution is to use the plastic scintillator as an efficient fast neutron converter which, furthermore, provides information about the interaction. Sensing of the light from the scintillator slab is ensured by novel type of optical photodetectors – silicon photomultipliers (SiPMs). These thin sensors tightly cover the scintillator making the structure very compact. It allows to place it near the silicon pixel detector creating a "sandwich" structure. The overall concept supports telescopic arrangement of these structures that allows to recognize neutrons and protons in the undefined radiation field. Position sensitivity of the scintillator is reached by utilization of an array of silicon photomultipliers. The interaction point in the scintillator can be localized. Projection of the events hitting both detectors based on the interaction position defines the direction of the incoming neutrons.

- **Develop the electronic architecture for particle detection with an emphasis on scalability, interoperability and portability. Activation and synchronization of detection units is to be provided.**

The development of the electronic system fully respects the needs arising from the proposed design of the detection structure. The new system was designed according to the specific needs of the thesis project. An array of silicon photomultipliers provides analog signal corresponding to the amount of scintillation light. There are 16 elements that must be processed individually to preserve the position information. The integrated solution is desired to keep the device compact and portable. The multi-channel spectroscopic chip VATA64HDR16 was utilized. It contains circuitry for processing the SiPM signals and provides analog output that allows to measure energy deposited in the scintillator. Furthermore, each event crossing the threshold generates a trigger signal which is used for starting acquisition. The control logic is implemented in the FPGA

together with the interface for data transfer and the synchronization engine. This novel architecture works as a master device that controls the operation of the Timepix detector through the FITPix interface. The Multi-coincidence system is fully synchronized so only desired neutron events can be recognized and measured.

- **Prepare the algorithms for control and processing the measurements and detection evaluation. Elaborate on the coincidence technique and easy-to-use solution.**

The control algorithm is shared between the FPGA logic and the user software. The communication protocol between hardware and software parts was prepared. The system is fully configurable by the user through the own custom-made graphical user interface. System settings, acquisition control and data visualization and processing are provided. The special tool was made for processing data from the pixel detector and the scintillator. Timepix clusters are filtered and matched with proper scintillator frames. Such coincidence data completely describe the neutron interaction. The determination of the neutron direction is based on selection of data according to the interaction point while all neutron events are still available for energy calculation.

- **Support the concept by the assembled device. Tune up the device performance and test and verify it by practical measurements with radiation sources.**

The new instrument was assembled according to the specified design. It is a fully working prototype device composed of the new readout system for the SiPM array with the attached scintillator slab and the pixel detector Timepix with the FITPix interface. The mechanical support and ambient light shielding makes the device packing. The final dimensions are $30\ \text{cm} \times 28\ \text{cm} \times 10\ \text{cm}$ that makes the device portable. The prototype device performance was optimized by equalization of the channels, this applies to both the pixel detector and the silicon photomultiplier array. The ultimate verification of the Multi-coincidence system was made with the neutron source AmBe when the response of the detectors, the overall functionality, the system synchronization and the data processing was successfully proved. The real detection efficiency almost reaches the simulated one, the difference is only by a factor of two. The achievable directional resolution below 2 degrees is better than available by another device known so far.

The thesis outcomes were presented during the work at the international conferences

- 14th International Workshop on Radiation Imaging Detectors, 2012, Portugal
- IEEE NSS/MIC Conference, France, 2016

and the topic was approved by the scientific community as the impacted article

MAŠEK, P.; JAKŮBEK, J.; UHER, J.; PRESTON, R. Directional Detection of Fast Neutrons by the Timepix Pixel Detector Coupled to Plastic Scintillator with Silicon Photomultiplier Array. Journal of Instrumentation. 2013, 8(C01021), pp. 1-6. ISSN 1748-0221

The direct contribution of this thesis is the new method for neutron detection which was developed and successfully verified. The excellent directional resolution achieved, while maintaining the detection efficiency, provides a significantly better description of the detected neutron field. The benefits of this work can be exploited in a variety of physical applications, where the key issue is the neutron detection and the separation from other types of radiation, such as study of fission reactions, neutron measurements in a hadron therapy, searching of radiation threats or a space weather monitoring.

References

[1] Knoll, G. F. *Radiation Detection and Measurement, 3rd ed.* New York : Wiley, 2000. ISBN: 0-471-07338-5.

[2] Spieler, H. *Semiconductor Detector Systems.* Oxford : Oxford University Press, 2005. ISBN: 978-0-19-852784-8.

[3] Da Via, C. et al. 3D silicon sensors: Design, large area production and quality assurance for the ATLAS IBL pixel detector upgrade. *Nucl. Instr. and Meth. A 694.* p. 321–330, 2012.

[4] Llopart, X., Ballabriga, R., Campbell, M., Tlustos, L., Wong, W. Timepix, a 65k Programmable Pixel Readout Chip for Arrival Time, Energy and/or Photon Counting Measurements. *Nucl. Instr. and Meth. A 581.* p. 485–494, 2007, Issues 1–2.

[5] Medipix Collaboration homepage. [Online] [cit. 2017-03-15]. Available at: http://www.cern.ch/medipix.

[6] Kraus, V., Holik, M., Jakubek, J., Kroupa, M., Soukup, P., Vykydal, Z. FITPix - Fast Interface for Timepix Pixel Detectors. *Journal of Instrumentation 6 C01079.* 2011.

[7] Turecek, D., Holy, T., Jakubek, J., Pospisil, S., Vykydal, Z. Pixelman: a Multi-platform Data Acquisition and Processing Software Package for Medipix2, Timepix and Medipix3 Detectors. *Journal of Instrumentation 6 C01046.* 2011.

[8] Uher, J., Jakubek, J. Equalization of Medipix2 imaging detector energy thresholds using measurement of polychromatic X-ray beam attenuation. *Journal of Instrumentation 6 C11012.* 2011.

[9] Jakubek, J. Precise Energy Calibration of Pixel Detector Working in Time-Over-Threshold Mode. *Nucl. Instr. and Meth. A 633.* p. S262–S266, 2011, Supplement 1.

[10] Kreisler, B., Anton, G., Durst, J., Michel, T. Induced Signals in X-ray Detectors. *IEEE Nuclear Science Symposium Conference Record.* 2009.

[11] Amorini, F. et al. Digital Signal Processing for Monolithic Silicon Detector Telescopes. *IEEE Nuclear Science Symposium Conference Record.* 2008.

[12] Bouchami, J. et al. Study of the Charge Sharing in Silicon Pixel Detector by Means of Heavy Ionizing Particles Interacting with a Medipix2 Device. *Nucl. Instr. and Meth. A 633.* p. S117–S120, 2011, Supplement 1.

[13] Llopart, X. TimePix Users's Manual. *CERN, distributed only between members.* 2006.

[14] Jakubek, J. Semiconductor Pixel Detectors and Their Applications in Life Sciences. *Journal of Instrumentation 4 P03013.* 2009.

[15] Soukup, P., Jakubek, J., Vykydal, Z. 3D Sensitive Voxel Detector of Ionizing Radiation Based on Timepix Device. *Journal of Instrumentation 6 C01060.* 2011.

[16] Keppler, E., Glasmachers, A., Winkelnkemper, W. New Design Aspects for an Energetic Particle Telescope for Space Missions. *IEEE Transactions on Instrumentation and Measurement.* 1981, Volume: IM-30, Issue: 3.

[17] Marco-Hernández, R. A Beam Test Telescope Based on the Alibava Readout System. *IEEE Nuclear Science Symposium Conference Record.* 2010.

[18] Johnson, R. P. et al. Results from a Pre-Clinical Head Scanner for Proton CT. *IEEE Nuclear Science Symposium and Medical Imaging Conference.* 2014.

[19] Jakubek, J., Uher, J. Fast Neutron Detector Based on TimePix Pixel Device with Micrometer Spatial Resolution. *IEEE Nuclear Science Symposium Conference Record.* 2009.

[20] Jakubek, J., Uher, J., Soukup, P. Fast Neutron Tracker Based on 3D Position Sensitive Semiconductor Voxel Detector. *IEEE Nuclear Science Symposium Conference Record.* 2010.

[21] Sadygov, Z. Y. *Patent of Russia No. 2102821.* 1998.

[22] Philips Digital Photon Counting. [Online] [cit. 2017-04-22]. Available at: http://www.digitalphotoncounting.com/tech-details/.

[23] An Introduction to the Silicon Photomultiplier. *SensL - Technical note.* Rev. 6.0, February 2017. Available online: https://www.google.cz/url?sa=t&rct=j&q=&esrc=s&source=web&cd=1&ved=0ahUKEwjvn8TWlZrUAhVJuhoKHZGDAzIQFggtMAA&url=http%3A%2F%2Fwww.sensl.com%2Fdownloads%2Fds%2FTN%2520-%2520Intro%2520to%2520SPM%2520Tech.pdf&usg=AFQjCNH9dTkAVqFiinL0donLu1Px.

[24] Fabris, L. et al. Understanding SiPM Instrumentation and Why SiPMs May Not Replace PMTs. *IEEE Nuclear Science Symposium Conference Record.* 2016.

[25] An Introduction to the Silicon Photomultiplier. *SensL - Technical note.* Rev. 3.1, October 2011.

[26] How to Evaluate and Compare Silicon Photomultiplier Sensors. *SensL - White paper.* Rev. 1.1, October 2015.

[27] SensL eStore. [Online] Available at: http://sensl.com/estore/.

[28] UV-Sensitive, 4-Side Scalable Silicon Photomultiplier Array. *SensL - Datasheet.* Rev. 1.1, September 2013.

[29] Bower, K. E., Barbanel, Y. A., Shreter, Y. G., Bohnert, G. W. *Polymers, Phosphors, and Voltaics for Radioisotope Microbatteries.* Florida : CRC Press, 2002. ISBN: 978-0-8493-0915-1.

[30] Smolek, K. et al. Measurement of High Energy Cosmic Rays in the Experiment CZELTA. *IEEE Nuclear Science Symposium Conference Record.* 2008.

[31] Hodak, R. et al. Improvement of the Energy Resolution of the Scintillating Detectors for the Low Background Measurement. *AIP Conference Proceedings 1672.* 2015.

[32] Štekl, I., Hodák, R., Přidal, P., Smolek, K., Burešová, H. Plastový scintilátor na bázi polystyrenu pro detektory. *Patent.* 2016. Available online: https://isdv.upv.cz/webapp/pts.det?xprim=10088809&lan=cs&s_majs=&s_puvo=&s_naze=&s_anot=.

[33] Interactions of Ions with Matter. [Online] [cit. 2017-04-27]. Available at: http://www.srim.org/.

[34] C-Series Family. [Online] [cit. 2017-04-12]. Available at: http://sensl.com/products/c-series/.

[35] Low Noise, Fast, Blue-Sensitive Silicon Photomultipliers. *SensL - Datasheet.* Rev. 2.0, November 2015.

[36] Polak, I. Gain stabilization of SiPMs. *IEEE Nuclear Science Symposium Conference Record.* 2016.

[37] Licciulli, F., Indiveri, I., Marzocca, C. A Novel Technique for the Stabilization of SiPM Gain Against Temperature Variations. *IEEE Transactions on Nuclear Science.* 2013, Volume: 60, Issue: 2.

[38] Gil, A., Rodriguez, J., Alvarez, V., Diaz, J., Gomez-Cadenas, JJ., Lorca, D. Programmable power supply system for SiPM bias. *IEEE Nuclear Science Symposium Conference Record.* 2011.

[39] Preston, R., Jakubek, J., Prokopovich, D., Uher, J. Proton beam characterisation of a prototype thin-tile plastic scintillator detector with SiPM readout for use in fast-neutron tracker. *Journal of Instrumentation 7 P02007.* 2012.

[40] de La Taille, Ch. Overview of SiPM readout electronics. *International Workshop on New Photon-detectors.* 2012. Available at: https://indico.cern.ch/event/164917/contributions/1417117/.

[41] VATA64HDR16, specification V2R2. *IDEAS - Datasheet.* 2010.

[42] DS557 - Spartan-3AN FPGA Family Data Sheet, v4.2. *Xilinx - Datasheet.* June 2014. Available online: https://www.xilinx.com/support/documentation/data_sheets/ds557.pdf.

[43] D2XX Direct Drivers. [Online] [cit. 2017-07-03]. Available online: http://www.ftdichip.com/Drivers/D2XX.htm.

[44] Iguchi, T., Iizuka, S., Uritani, A., Kawarabayashi, J. Development of directional neutron detector for compact fast neutron camera. *IEEE Nuclear Science Symposium Conference Record.* 2000.

[45] Son, S. et al. Neutron Imaging Camera. *IEEE International Conference on Technologies for Homeland Security (HST).* 2010.

[46] Archambault, B. C. et al. Development of a novel direction-position sensing fast neutron detector using tensioned metastable fluids. *Nucl. Instr. and Meth. A 673.* p. 89-97, 2012.

[47] Peel, J., Mascarenhasa, N., Mengeshaa, W., Sunnarborga, D. Development of a directional scintillating fiber detector for 14MeV neutrons. *Nucl. Instr. anf Meth. A 556.* p. 287-290, 2006.

[48] Marafini, M. et al. MONDO: a neutron tracker for particle therapy secondary emission characterisation. *Physics in Medicine & Biology, Volume 62, Number 8.* 2017.

[49] Ziegler, J. F., Ziegler, M. D., Biersack, J.P. SRIM – The stopping and range of ions in matter. *Nucl. Instr. and Meth. B 286.* p. 1818–1823, 2010.

[50] Kreisler, B., Anton, G. Durst, J., Michel, T. Induced Signals in X-ray Detectors. *IEEE Nuclear Science Symposium Conference Record.* 2009.

List of candidate's publications

Publications related to the thesis topic - Impacted articles

[RI1] **MAŠEK, P.**; JAKŮBEK, J.; UHER, J.; PRESTON, R. Directional Detection of Fast Neutrons by the Timepix Pixel Detector Coupled to Plastic Scintillator with Silicon Photomultiplier Array. *Journal of Instrumentation.* 2013, 8(C01021), pp. 1-6. ISSN 1748-0221. (Impact Factor 2013 = 1.526, Citations = 1, authors participation = 60/20/10/10)

Publications related to the thesis topic - Conference proceedings

[RP1] **MAŠEK, P.**; JAKŮBEK, J. Improved Fast Neutron Detector Based on Timepix and Plastic Scintillating Converter. In: *IEEE Nuclear Science Symposium 2016 Conference Record.* 2016 IEEE Nuclear Science Symposium and Medical Imaging Conference. Strasbourg, 29.10.2016 - 05.11.2016. (accepted, not yet published)

[RP2] GRANJA, C.; KRAUS, V.; JAKŮBEK, J.; POSPÍŠIL, S.; **MAŠEK, P.**; VYKYDAL, Z.; PLATKEVIČ, M.; KOHOUT, Z. et al. Spatially Correlated and Coincidence Detection of Fission Fragments with the Pixel Detector Timepix. In: *IEEE Nuclear Science Symposium 2010 Conference Record.* 2010 IEEE Nuclear Science Symposium and Medical Imaging Conference. Knoxville, 30.10.2010 - 06.11.2010. Piscataway: IEEE. 2011, pp. 131-137. ISSN 1082-3654. ISBN 978-1-4244-3962-1. (Citations = 5)

Publications related to the thesis topic - Functional samples

[RF1] **MAŠEK, P.** Multichannel SiPM readout system. [Functional Sample]. 2015, Available from: http://old.utef.cvut.cz/en/index.php?Ns=103&id=1000101

[RF2] **MAŠEK, P.** and PŘIDAL, P. Switching current regulator for SiPM biasing. [Functional Sample]. 2015, Available from: http://old.utef.cvut.cz/en/index.php?Ns=103&id=1000098

[RF3] **MAŠEK, P.** and PŘIDAL, P. Testing kit for array of silicon photomultipliers. [Functional Sample]. 2013, Available from: http://www.utef.cvut.cz/en/index.php?Ns=103&id=1000069

[RF4] **MAŠEK, P.**, SOUKUP, P., and JAKŮBEK, J. Directional Fast Neutron Detector based on Timepix Coupled to Plastic Scintillator SiPM Array. [Functional Sample]. 2012, Available from: http://www.utef.cvut.cz/en/index.php?Ns=103&id=1000066

Publications not related to the thesis topic - Impacted articles

[NI1] AFFOLDER, A., et al. Silicon detectors for the sLHC. *Nuclear Instruments and Methods in Physics Research, Section A, Accelerators, Spectrometers,*

Detectors and Associated Equipment. 2011, **658**(1), pp. 11-16. ISSN 0168-9002. Available from: http://dx.doi.org/10.1016/j.nima.2011.04.045 (Impact Factor 2011 = 1.207, Citations = 17)

[NI2] **MAŠEK, P.**; LINHART, V.; GRANJA, C.; POSPÍŠIL, S.; HUSÁK, M. Integrated USB based readout interface for silicon strip detectors of the ATLAS SCT module. *Journal of Instrumentation.* 2011, **6**(C12016), pp. 1-5. ISSN 1748-0221. (Impact Factor 2013 = 1.869, Citations = 1)

Publications not related to the thesis topic - Conference proceedings

[NP1] GRANJA, C.; KRALIK, M.; KOHOUT, Z.; **MAŠEK, P.**; POSPÍŠIL, S.; VYKYDAL, Z.; ŠOLC, J.; SOLAR, M. et al. Neutron Sources for Test and Calibration of Neutron Detectors for Space Research. In: AYALA, E., et al., eds. *IX Latin American Symposium on Nuclear Physics and Applications.* IX Latin American Symposium on Nuclear Physics and Applications. Quito, 18.07.2011 - 22.07.2011. Melville, New York: American Institute of Physics. 2012, pp. 446-452. ISSN 0094-243X. ISBN 978-0-7354-1003-9. Available from: http://proceedings.aip.org/resource/2/apcpcs/1423/1/446_1 (Citations = 1)

[NP2] **MAŠEK, P.** Portable Tracker Based on the ATLAS SCT Module Controlled by USB-Based Readout Interface. In: *IEEE Nuclear Science Symposium and Medical Imaging Conference 2011.* IEEE Nuclear Science Symposium and Medical Imaging Conference. Valencia, 23.10.2011 - 29.10.2011. Piscataway, New Jersey: Omnipress. 2011, pp. 482-484. ISSN 1082-3654. ISBN 978-1-4673-0118-3.

Publications not related to the thesis topic - Patents and industrial designs

[NT1] POSPÍŠIL, S.; **MAŠEK, P.**; SVOBODA, Z.; TOUŠ, J.; SMEJKAL, J.; HRADECKÝ, P. *Detektor pro detekci více složek pole záření.* CRYTUR, spol. s r.o.; Ústav technické a experimentální fyziky ČVUT v Praze. 36858. 26.10.2016.

Publications not related to the thesis topic - Functional samples

[NF1] **MAŠEK, P.**, SLAVÍČEK, T., and KOHOUT, Z. Polohově citlivý neutronový detektor s VATA GP8. [Functional Sample]. 2017

[NF2] KOUBA, P.; ŠTEKL, I.; **MAŠEK, P.**; HŮLKA, J.; ČEŠPÍROVÁ, I.; BELAS, E. Terénní identifikátor radionuklidů na bázi CdTe. [Functional Sample]. 2015

[NF3] SLAVÍČEK, T. and **MAŠEK, P.** Evaluation board VATA GP7 with PAD diodes. [Functional Sample]. 2015, Available from: http://ad-bang.utef.cvut.cz/

[NF4] SLAVÍČEK, T. and **MAŠEK, P.** Evaluation board VATA GP7 with Strip detector with deposited neutron convertor. [Functional Sample]. 2015, Available from: http://ad-bang.utef.cvut.cz/

[NF5] **MAŠEK, P.** and SLAVÍČEK, T. Evaluation board VATA GP7. [Functional Sample]. 2014, Available from: http://www.utef.cvut.cz/en/index.php?Ns=103&id=1000094

[NF6] PŘIDAL, P. and **MAŠEK, P.** Amplifier for from SiPM for S3 detector purpose. [Functional Sample]. 2014, Available from: http://www.utef.cvut.cz/en/index.php?Ns=103&id=1000093

[NF7] **MAŠEK, P.** and KOHOUT, Z. Simple spectrometer with Si detector. [Functional Sample]. 2014, Available from: http://www.utef.cvut.cz/en/index.php?Ns=103&id=1000092

[NF8] **MAŠEK, P.** Digitizer module multi-channel agregator. [Functional Sample]. 2014, Available from: http://www.utef.cvut.cz/en/index.php?Ns=103&id=1000091

[NF9] **MAŠEK, P.** Fast ADC module. [Functional Sample]. 2013, Available from: https://www.rvvi.cz/riv?ss=detail&h=RIV%2F68407700%3A21670%2F13%3A00215784%21RIV14-TA0-21670___

[NF10] KOHOUT, Z.; **MAŠEK, P.**; SOLAR, M.; GRANJA, C. Neutron monitor 3He Bonner sphere for VdG neutron sources. [Functional Sample]. 2013, Available from: http://www.utef.cvut.cz/en/index.php?Ns=103&id=1000083

[NF11] KOHOUT, Z.; **MAŠEK, P.**; GRANJA, C.; SOLAR, M. Fast neutron on-line monitor for the VdG accelerator neutron sources. [Functional Sample]. 2013, Available from: http://www.utef.cvut.cz/en/index.php?&Ns=103&id=1000082

[NF12] **MAŠEK, P.**; SOLAR, M.; GRANJA, C.; LINHART, V. Gamma-gamma coincidence unit. [Functional Sample]. 2013, Available from: http://www.utef.cvut.cz/cz/index.php?Ns=103&id=1000077

[NF13] **MAŠEK, P.** Readout interface for silicon strip radiation detectors of SCT type. [Functional Sample]. 2010, Available from: http://www.utef.cvut.cz

Publications not related to the thesis topic - Others

[NO1] SLAVÍČEK, T.; POSPÍŠIL, S.; **MAŠEK, P.**; URBAN, T.; TROJEK, T.; KOHOUT, Z. Development of Neutron Image Sensor Technology for AD-BANG project. In: *2016 IEEE NSS/MIC*. 2016 IEEE NSS/MIC. Štrasburg, 29.10.2016 - 05.11.2016. IEEE Xplore. 2016, Available from: http://ad-bang.utef.cvut.cz/cs/o-projektu/

[NO2] URBAN, T.; SLAVÍČEK, T.; HŮLKA, J.; KOK, A.; MEIER, D.; **MAŠEK, P.**; POSPÍŠIL, S.; KOYBASI, O. et al. Stripové křemíkové senzory pro měření ve směsných neutron-gama radiačních polích. In: *XXXVIII. Dny radiační ochrany*. XXXVIII. Dny radiační ochrany. Mikulov, 07.11.2016 - 11.11.2016. Praha: České vysoké učení technické v Praze. 2016, pp. 119. ISBN 978-80-01-06028-5. Available from: http://reg.fjfi.cvut.cz/dro2016/proofs/dro2016-el.pdf

Appendix A

Values of projected range of the protons (recoiled hydrogen) in polystyrene and silicon for different energies were obtained by SRIM calculator [49].

```
==================================================================
          SRIM version ---> SRIM-2013.00
          Calc. date   ---> Oct 27, 2016
==================================================================

Ion = Hydrogen [1] , Mass = 1.008 amu

 Target Density =  1.0600E+00 g/cm3 = 9.8062E+22 atoms/cm3
 ======== Target  Composition ========
   Atom   Atom   Atomic    Mass
   Name   Numb   Percent   Percent
   ----   ----   -------   -------
    H      1    050.00    007.74
    C      6    050.00    092.26
 ======================================
 Bragg Correction = 0.35%
 Stopping Units =  MeV / (mg/cm2)
 See bottom of Table for other Stopping units

      Ion       dE/dx      dE/dx     Projected  Longitudinal   Lateral
     Energy     Elec.     Nuclear     Range     Straggling   Straggling
 --------------  ----------  ----------  ----------  ----------  ----------
 10.00 keV   5.460E-01  8.191E-03   2105 A      481 A       515 A
 11.00 keV   5.694E-01  7.655E-03   2260 A      493 A       534 A
 12.00 keV   5.913E-01  7.192E-03   2410 A      504 A       552 A
 13.00 keV   6.118E-01  6.788E-03   2555 A      514 A       569 A
 14.00 keV   6.311E-01  6.431E-03   2697 A      523 A       584 A
 15.00 keV   6.492E-01  6.114E-03   2835 A      531 A       599 A
 16.00 keV   6.663E-01  5.831E-03   2970 A      539 A       612 A
 17.00 keV   6.825E-01  5.574E-03   3102 A      546 A       625 A
 18.00 keV   6.977E-01  5.342E-03   3232 A      553 A       637 A
 20.00 keV   7.258E-01  4.937E-03   3485 A      565 A       660 A
 22.50 keV   7.569E-01  4.517E-03   3789 A      580 A       685 A
 25.00 keV   7.841E-01  4.168E-03   4084 A      592 A       708 A
 27.50 keV   8.079E-01  3.874E-03   4370 A      603 A       729 A
 30.00 keV   8.290E-01  3.623E-03   4649 A      613 A       749 A
 32.50 keV   8.475E-01  3.405E-03   4923 A      623 A       767 A
 35.00 keV   8.639E-01  3.214E-03   5191 A      631 A       784 A
 37.50 keV   8.784E-01  3.045E-03   5455 A      639 A       800 A
 40.00 keV   8.912E-01  2.894E-03   5716 A      647 A       815 A
 45.00 keV   9.122E-01  2.637E-03   6228 A      662 A       843 A
 50.00 keV   9.281E-01  2.425E-03   6731 A      677 A       869 A
 55.00 keV   9.396E-01  2.248E-03   7228 A      690 A       894 A
 60.00 keV   9.473E-01  2.096E-03   7720 A      702 A       916 A
 65.00 keV   9.518E-01  1.965E-03   8210 A      714 A       938 A
 70.00 keV   9.535E-01  1.851E-03   8699 A      725 A       959 A
 80.00 keV   9.497E-01  1.661E-03   9679 A      752 A       999 A
 90.00 keV   9.388E-01  1.509E-03   1.07 um     778 A      1037 A
100.00 keV   9.228E-01  1.384E-03   1.17 um     804 A      1073 A
110.00 keV   9.035E-01  1.279E-03   1.27 um     829 A      1109 A
120.00 keV   8.821E-01  1.191E-03   1.37 um     854 A      1145 A
130.00 keV   8.598E-01  1.114E-03   1.48 um     879 A      1180 A
140.00 keV   8.371E-01  1.048E-03   1.59 um     904 A      1216 A
```

150.00 keV	8.145E-01	9.892E-04	1.71 um	930 A	1252 A
160.00 keV	7.924E-01	9.374E-04	1.82 um	956 A	1288 A
170.00 keV	7.710E-01	8.910E-04	1.94 um	982 A	1325 A
180.00 keV	7.503E-01	8.493E-04	2.07 um	1009 A	1363 A
200.00 keV	7.117E-01	7.774E-04	2.32 um	1096 A	1440 A
225.00 keV	6.682E-01	7.039E-04	2.66 um	1225 A	1541 A
250.00 keV	6.299E-01	6.439E-04	3.03 um	1356 A	1648 A
275.00 keV	5.961E-01	5.939E-04	3.41 um	1489 A	1761 A
300.00 keV	5.661E-01	5.515E-04	3.81 um	1624 A	1879 A
325.00 keV	5.394E-01	5.152E-04	4.24 um	1762 A	2004 A
350.00 keV	5.154E-01	4.836E-04	4.68 um	1902 A	2135 A
375.00 keV	4.939E-01	4.559E-04	5.15 um	2045 A	2271 A
400.00 keV	4.744E-01	4.313E-04	5.64 um	2190 A	2414 A
450.00 keV	4.405E-01	3.899E-04	6.66 um	2689 A	2716 A
500.00 keV	4.119E-01	3.560E-04	7.77 um	3171 A	3040 A
550.00 keV	3.875E-01	3.279E-04	8.95 um	3644 A	3385 A
600.00 keV	3.663E-01	3.042E-04	10.19 um	4113 A	3750 A
650.00 keV	3.478E-01	2.838E-04	11.51 um	4582 A	4135 A
700.00 keV	3.314E-01	2.661E-04	12.90 um	5053 A	4538 A
800.00 keV	3.038E-01	2.369E-04	15.86 um	6691 A	5397 A
900.00 keV	2.812E-01	2.138E-04	19.08 um	8220 A	6323 A
1.00 MeV	2.624E-01	1.950E-04	22.55 um	9700 A	7312 A
1.10 MeV	2.489E-01	1.794E-04	26.23 um	1.11 um	8356 A
1.20 MeV	2.358E-01	1.662E-04	30.12 um	1.26 um	9448 A
1.30 MeV	2.227E-01	1.550E-04	34.22 um	1.40 um	1.06 um
1.40 MeV	2.111E-01	1.452E-04	38.57 um	1.54 um	1.18 um
1.50 MeV	2.008E-01	1.366E-04	43.14 um	1.69 um	1.31 um
1.60 MeV	1.915E-01	1.291E-04	47.94 um	1.84 um	1.44 um
1.70 MeV	1.832E-01	1.224E-04	52.97 um	1.99 um	1.57 um
1.80 MeV	1.756E-01	1.163E-04	58.21 um	2.14 um	1.71 um
2.00 MeV	1.623E-01	1.060E-04	69.37 um	2.70 um	2.02 um
2.25 MeV	1.485E-01	9.550E-05	84.54 um	3.49 um	2.42 um
2.50 MeV	1.370E-01	8.698E-05	101.04 um	4.25 um	2.86 um
2.75 MeV	1.274E-01	7.992E-05	118.86 um	4.99 um	3.33 um
3.00 MeV	1.191E-01	7.397E-05	137.97 um	5.72 um	3.83 um
3.25 MeV	1.120E-01	6.888E-05	158.35 um	6.46 um	4.36 um
3.50 MeV	1.057E-01	6.448E-05	179.99 um	7.21 um	4.92 um
3.75 MeV	1.002E-01	6.063E-05	202.86 um	7.97 um	5.51 um
4.00 MeV	9.526E-02	5.723E-05	226.96 um	8.73 um	6.13 um
4.50 MeV	8.683E-02	5.151E-05	278.75 um	11.52 um	7.46 um
5.00 MeV	7.990E-02	4.687E-05	335.29 um	14.16 um	8.90 um
5.50 MeV	7.408E-02	4.304E-05	396.52 um	16.73 um	10.45 um
6.00 MeV	6.911E-02	3.980E-05	462.34 um	19.30 um	12.11 um
6.50 MeV	6.483E-02	3.704E-05	532.70 um	21.87 um	13.88 um
7.00 MeV	6.109E-02	3.465E-05	607.54 um	24.47 um	15.75 um
8.00 MeV	5.486E-02	3.073E-05	770.27 um	33.91 um	19.80 um
9.00 MeV	4.988E-02	2.763E-05	950.36 um	42.75 um	24.26 um
10.00 MeV	4.580E-02	2.513E-05	1.15 mm	51.40 um	29.12 um
11.00 MeV	4.239E-02	2.305E-05	1.36 mm	60.03 um	34.36 um
12.00 MeV	3.949E-02	2.131E-05	1.59 mm	68.73 um	39.98 um
13.00 MeV	3.699E-02	1.982E-05	1.84 mm	77.54 um	45.98 um
14.00 MeV	3.482E-02	1.853E-05	2.10 mm	86.48 um	52.34 um
15.00 MeV	3.291E-02	1.741E-05	2.38 mm	95.56 um	59.07 um

==========

==========

SRIM version ---> SRIM-2013.00
Calc. date ---> duben 24, 2017

==========

Ion = Hydrogen [1] , Mass = 1.008 amu

Target Density = 2.3212E+00 g/cm3 = 4.9770E+22 atoms/cm3

======== Target Composition ========

Atom Name	Atom Numb	Atomic Percent	Mass Percent
Si	14	100.00	100.00

==========

Bragg Correction = 0.00%
Stopping Units = MeV / (mg/cm2)
See bottom of Table for other Stopping units

Ion Energy	dE/dx Elec.	dE/dx Nuclear	Projected Range	Longitudinal Straggling	Lateral Straggling
10.00 keV	3.131E-01	4.222E-03	1342 A	519 A	488 A
11.00 keV	3.277E-01	3.995E-03	1452 A	538 A	511 A
12.00 keV	3.419E-01	3.794E-03	1558 A	554 A	532 A
13.00 keV	3.556E-01	3.615E-03	1662 A	569 A	552 A
14.00 keV	3.688E-01	3.455E-03	1762 A	583 A	571 A
15.00 keV	3.813E-01	3.310E-03	1861 A	596 A	589 A
16.00 keV	3.933E-01	3.179E-03	1957 A	608 A	605 A
17.00 keV	4.046E-01	3.059E-03	2051 A	619 A	621 A
18.00 keV	4.152E-01	2.949E-03	2143 A	629 A	636 A
20.00 keV	4.346E-01	2.755E-03	2323 A	648 A	664 A
22.50 keV	4.556E-01	2.549E-03	2540 A	669 A	696 A
25.00 keV	4.732E-01	2.375E-03	2751 A	688 A	726 A
27.50 keV	4.878E-01	2.226E-03	2956 A	704 A	752 A
30.00 keV	4.999E-01	2.097E-03	3157 A	720 A	778 A
32.50 keV	5.097E-01	1.984E-03	3355 A	734 A	801 A
35.00 keV	5.177E-01	1.883E-03	3550 A	747 A	824 A
37.50 keV	5.240E-01	1.794E-03	3744 A	759 A	845 A
40.00 keV	5.289E-01	1.713E-03	3937 A	771 A	866 A
45.00 keV	5.352E-01	1.575E-03	4320 A	793 A	905 A
50.00 keV	5.380E-01	1.459E-03	4701 A	814 A	942 A
55.00 keV	5.382E-01	1.360E-03	5084 A	833 A	977 A
60.00 keV	5.365E-01	1.276E-03	5468 A	852 A	1011 A
65.00 keV	5.334E-01	1.202E-03	5855 A	869 A	1044 A
70.00 keV	5.293E-01	1.137E-03	6246 A	886 A	1077 A
80.00 keV	5.192E-01	1.028E-03	7041 A	922 A	1140 A
90.00 keV	5.077E-01	9.403E-04	7856 A	957 A	1203 A
100.00 keV	4.957E-01	8.673E-04	8692 A	991 A	1265 A
110.00 keV	4.836E-01	8.057E-04	9550 A	1024 A	1326 A
120.00 keV	4.717E-01	7.531E-04	1.04 um	1058 A	1388 A
130.00 keV	4.603E-01	7.075E-04	1.13 um	1091 A	1451 A
140.00 keV	4.492E-01	6.675E-04	1.23 um	1124 A	1513 A
150.00 keV	4.387E-01	6.322E-04	1.32 um	1158 A	1577 A
160.00 keV	4.286E-01	6.008E-04	1.42 um	1192 A	1641 A
170.00 keV	4.190E-01	5.726E-04	1.52 um	1226 A	1706 A
180.00 keV	4.099E-01	5.471E-04	1.62 um	1261 A	1772 A
200.00 keV	3.930E-01	5.030E-04	1.83 um	1347 A	1907 A
225.00 keV	3.741E-01	4.576E-04	2.11 um	1466 A	2081 A
250.00 keV	3.573E-01	4.203E-04	2.40 um	1587 A	2261 A
275.00 keV	3.423E-01	3.890E-04	2.70 um	1710 A	2447 A
300.00 keV	3.288E-01	3.624E-04	3.02 um	1835 A	2638 A
325.00 keV	3.166E-01	3.395E-04	3.35 um	1961 A	2836 A
350.00 keV	3.055E-01	3.194E-04	3.69 um	2089 A	3039 A

375.00 keV	2.954E-01	3.018E-04	4.05 um	2219 A	3248 A
400.00 keV	2.861E-01	2.862E-04	4.41 um	2351 A	3463 A
450.00 keV	2.696E-01	2.596E-04	5.18 um	2727 A	3908 A
500.00 keV	2.554E-01	2.379E-04	5.99 um	3098 A	4373 A
550.00 keV	2.430E-01	2.197E-04	6.85 um	3468 A	4857 A
600.00 keV	2.321E-01	2.043E-04	7.75 um	3838 A	5360 A
650.00 keV	2.224E-01	1.911E-04	8.69 um	4209 A	5881 A
700.00 keV	2.137E-01	1.795E-04	9.67 um	4582 A	6418 A
800.00 keV	1.986E-01	1.604E-04	11.74 um	5719 A	7542 A
900.00 keV	1.861E-01	1.452E-04	13.97 um	6806 A	8728 A
1.00 MeV	1.755E-01	1.328E-04	16.33 um	7871 A	9972 A
1.10 MeV	1.663E-01	1.225E-04	18.84 um	8926 A	1.13 um
1.20 MeV	1.571E-01	1.137E-04	21.48 um	9986 A	1.26 um
1.30 MeV	1.492E-01	1.062E-04	24.28 um	1.11 um	1.40 um
1.40 MeV	1.423E-01	9.965E-05	27.22 um	1.21 um	1.55 um
1.50 MeV	1.361E-01	9.392E-05	30.29 um	1.32 um	1.71 um
1.60 MeV	1.305E-01	8.886E-05	33.50 um	1.44 um	1.87 um
1.70 MeV	1.253E-01	8.434E-05	36.85 um	1.55 um	2.03 um
1.80 MeV	1.207E-01	8.029E-05	40.33 um	1.66 um	2.20 um
2.00 MeV	1.124E-01	7.331E-05	47.69 um	2.04 um	2.56 um
2.25 MeV	1.037E-01	6.620E-05	57.61 um	2.56 um	3.03 um
2.50 MeV	9.644E-02	6.042E-05	68.32 um	3.07 um	3.54 um
2.75 MeV	9.023E-02	5.562E-05	79.80 um	3.56 um	4.08 um
3.00 MeV	8.486E-02	5.156E-05	92.05 um	4.06 um	4.66 um
3.25 MeV	8.018E-02	4.808E-05	105.03 um	4.56 um	5.26 um
3.50 MeV	7.604E-02	4.507E-05	118.76 um	5.07 um	5.89 um
3.75 MeV	7.236E-02	4.243E-05	133.20 um	5.59 um	6.55 um
4.00 MeV	6.906E-02	4.010E-05	148.36 um	6.11 um	7.24 um
4.50 MeV	6.338E-02	3.616E-05	180.77 um	7.86 um	8.71 um
5.00 MeV	5.866E-02	3.297E-05	215.93 um	9.54 um	10.29 um
5.50 MeV	5.466E-02	3.031E-05	253.80 um	11.19 um	11.97 um
6.00 MeV	5.124E-02	2.807E-05	294.32 um	12.84 um	13.76 um
6.50 MeV	4.826E-02	2.616E-05	337.45 um	14.50 um	15.66 um
7.00 MeV	4.564E-02	2.450E-05	383.14 um	16.17 um	17.66 um
8.00 MeV	4.125E-02	2.177E-05	482.01 um	21.92 um	21.95 um
9.00 MeV	3.771E-02	1.961E-05	590.78 um	27.36 um	26.64 um
10.00 MeV	3.479E-02	1.786E-05	709.23 um	32.70 um	31.70 um

==========

Appendix B

The wiring diagram of the Interface board for spectroscopic ASICs.

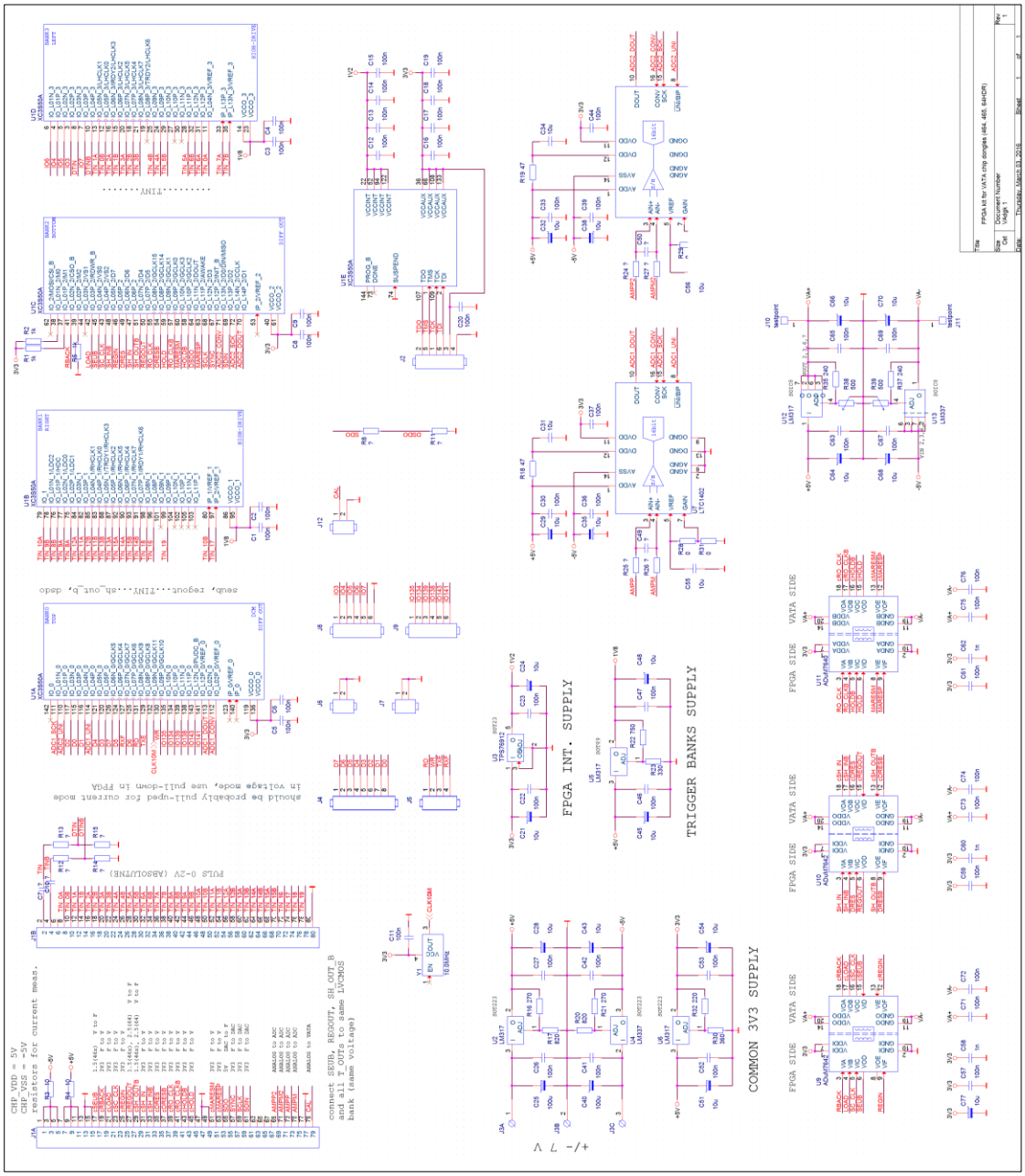

Appendix C

The wiring diagram of the Chip dongle for VATA64HDR16.